Probe Reactions of Alcohols and Alkanes for Understanding Catalytic Properties of Microporous Materials and Alumina Oxide Solid Acid Catalysts

A Dissertation
SUBMITTED TO THE FACULTY OF
UNIVERSITY OF MINNESOTA
BY

Hsu Chiang

IN PARTIAL FULFILLMENT OF THE REQUIREMENTS
FOR THE DEGREE OF
DOCTOR OF PHILOSOPHY

Adviser: Aditya Bhan

August, 2012

Acknowledgements

There are a number of people whom I would like to thank for their help in the past five years. Besides my family, the person I would like to thank the most is my adviser, professor Aditya Bhan, for his guidance, encouragement and teaching. He always gave me support and patience whenever I needed help in my graduate school career. I have learned many invaluable things from his advice, and these things will always be important in my life. I am grateful to be one of his first students so I can work closely with him and other group members in the Bhan research group. I will keep the good memories of the Bhan group in my mind forever. I also would like to thank all the Bhan group members for being helpful whenever I needed them. Thanks to Ian Hill for his support and company. I will always remember his help for finding my wedding ring. I appreciate Samia Ilias and Elizabeth Mallon for giving me good advice for my presentations. It is good to have Samia, Jeremy and Joseph to organize group lunch. Liz always keeps a positive attitude in times of frustration, which cheers me up. I also appreciate Dr. Dongxia Liu for teaching me zeolite synthesis and for giving me good advice when I was confused. Thanks to Dr. Do-Young Hong for his kindness and for teaching me infrared spectroscopy. I would like to visit him in Korea one day. Thanks to Srinivas Rangarajan for his help in my job searching. His questions about my research gave me experimental inspiration. Thanks to Jeremy Bedard, Mark Mazar and Sam Blass for adding fun to my life in the CEMS department. I still owe Jeremy a little bit of money for using his research unit for a while. I will return the money whenever my good friend Jeremy moves to Midland, MI. I deeply appreciate my good experimental partner Joseph DeWilde for helping me so much. Without his help, I could not have finished this thesis in time. Thanks to Cha-Jung Chen, who brought food from Taiwan to ease my homesickness. Thanks to the smart undergraduate students Chris Ho, Mingwei Tian, and Wenhao Liu, Derek Jones, and Ed Michor for experimental assistance. Mingwei Tian's smart program saved me a lot of time. One page is not enough for all the things and people I want to appreciate. Finally, I would like to thank my family for their endless love and strong support. They are always the strength and courage in my heart.

Abstract

Steady-state chemical reactions of alkanol dehydration and alkane hydroisomerization were employed as probe reactions to evaluate the effects of structure and composition of zeolites and gamma alumina (γ-Al_2O_3) on measured catalytic rates and selectivity to establish the mechanistic cycles and catalytic site requirements for the corresponding reactions.

The measured kinetic effects of ethanol and ethylene pressure on diethyl ether (DEE) formation over three zeolite materials (H-MFI, H-FER and H-MOR) show that ethanol dimers are formed during reaction and that these dimeric species are subsequently dehydrated to form DEE. In zeolites, ethylene formation was only observed on zeolites possessing 8-MR channels (H-MOR). The 8-MR channels protect ethanol monomeric species and prevent the formation of ethanol dimeric species due to size restrictions. The results of ethanol dehydration reactions studied in this research imply that the design and selection of microporous catalysts for performing shape-selective reactions of oxygenates requires us to consider the size and stability of the corresponding surface intermediates as well as the location of Brønsted acid sites.

Hydroisomerization reactions on bifunctional metal-acid catalysts (Pt/Al_2O_3 and acid zeolites) can convert n-hexane into 2-methylpentane (2MP) and 3-methylpentane (3MP). The measured rate of n-hexane isomerization was linearly proportional to the molar ratio of H_2 to n-C_6H_{14} over three zeolites (FER, MOR, BEA), consistent with a bifunctional mechanism involving the facile dehydrogenation of n-hexane into n-hexene on the metal catalyst and a kinetically-relevant step involving isomerization of n-hexene to 2MP and 3MP on zeolitic acidic sites. Sodium-exchanged MOR was used to study the rate of n-hexane isomerization in 12MR channel (MOR(12MR)) and 8MR pockets (MOR(8MR)) in MOR. The measured rate of isomerization over zeolites increase in the order of FER < MOR(12MR) < MOR(8MR) < BEA, showing that pore size cannot be used to accurately predict the occurrence or exclusion of a particular reaction within zeolitic solids.

The mechanisms and site requirements for unimolecular and bimolecular dehydration reactions of ethanol on γ-Al_2O_3 were investigated using steady state and isotopic kinetic

studies and in situ titration. The rates of ethylene and DEE formation from ethanol dehydration on γ-Al_2O_3 at 488K were not inhibited by exposure to CO_2 (0-47kPa) while pyridine exposure (3kPa) nearly shut down the rates of formation, showing that acid sites rather than basic sites are required for ethylene and DEE formation. The proposed mechanisms for ethylene and DEE formation proceed through desorption of surface-bound ethoxide species and the activation of surface ethanol dimeric species, respectively. The proposed mechanisms are consistent with the measured pressure dependence in ethanol and water, and the measured kinetic isotope effects using isotopic labeling reactants. The rate and equilibrium constants in the kinetic models derived from these mechanisms were estimated using Athena Visual Studio software to assess the stability of surface species formed during ethanol dehydration reactions.

Table of Contents

List of Tables

List of Figures

Chapter 1:
Introduction

1.1 Motivation

Zeolites and gamma-alumina (γ-Al_2O_3) are inorganic materials used as acid catalysts and catalyst supports for reforming, hydrotreating, alkylation, alcohol dehydration, and hydrocracking in the petrochemical industry [1-4]. In this study, alkane and alkanol conversion, including skeletal isomerization and dehydration reactions, were used as probe reactions to evaluate the effects of structure and composition on measured catalytic rates and selectivity to establish catalytic site requirements for the corresponding reactions. Kinetic analysis of the reactions of ethanol and n-hexane under study was carried out in conventional micro-reactor studies with concurrent chromatographic and mass spectrometric analysis of the effluent composition. The reactor effluents were measured as a function of temperature, reactor residence time, and varying concentrations of products and reactants. The identity of intermediate species and the reversibility of the relevant elementary steps were characterized by in-situ infrared spectroscopy and isotopic transient techniques. These techniques allowed for rigorous analysis of the elementary steps for the reactions and enabled us to determine the rate and equilibrium constants for elementary steps associated with these reactions. Transition state theory and thermodynamics allowed for quantitative elucidation of the effects of environment of the active sites on the reaction; specifically by determining the enthalpy and entropy of transition states, reflected in the values of the intrinsic rate constants, or the enthalpy and entropy of adsorption, reflected in the values of the equilibrium constants.

1.2 Shape selective catalysis on zeolites

Zeolites are crystalline aluminosilicates with micropores consisting of channels and cages of size typically smaller than 1 nm. These micropores can control adsorption and reactions within zeolites by their shape and size. Therefore, zeolites are widely used in industrial applications for catalysis, ion exchange, and separation [5-7]. One can also

consider zeolites as crystalline silicates which are constituted by a basic building block SiO_4 tetrahedron in which a fraction of the Si^{4+} are replaced by Al^{3+}, generating a negative charge which is typically balanced by cations, M^{n+}, inside the zeolite pores. In the special case that these cations are protons, zeolites become heterogeneous solid acids and are used industrially as catalysts for petroleum refining [5, 8].

The control of reaction selectivity by zeolite framework topology is referred to by the term shape selectivity. There are three classical concepts used to describe shape selectivity in zeolites: reactant selectivity, restricted transition state selectivity, and product selectivity [9-12]. Reactant selectivity refers to the scenario wherein molecules larger than the pore diameter of the zeolite cannot diffuse into the microporous environment and therefore, the size of the reactant precludes reactivity. Product selectivity refers to the scenario wherein bulky products formed inside zeolite pores diffuse slowly because of their size, with the result bulky products have more opportunities to be isomerized or cracked to other products which can diffuse through the pores faster. If the selectivity to reactants or products are induced by limited mass transfer, the value of selectivity will depend on the size of the crystal [13]. In restricted transition state selectivity, reactions with bulky transition state configurations are constrained by steric hindrance imposed by pore size and geometry restrictions around active sites [12, 13].

An alcohol can be dehydrated on an acidic catalyst via a unimolecular route to produce an olefin or through a bimolecular pathway to generate an ether. Using solid-state ^{13}C magic-angle spinning (MAS) NMR, Wang et al. [14] showed that adsorbed ethanol can be dehydrated into a surface-bound ethoxide species on a zeolite and Kondo et al. [15] observed that this surface-bound ethoxide species can desorb to form ethylene. Zecchina et al. [16] observed that two alcohol molecules can be adsorbed on one Brønsted acid site using infrared spectroscopy. The lack of change in the differential heat of adsorption of methanol and ethanol (90 and 130 kJ mol^{-1}, respectively) at coverages higher than one ethanol molecule per aluminum led Lee et al. [17] to also conclude that dimeric ethanol species are adsorbed on H-ZSM-5. The stability and identity of adsorption and reaction intermediates for alcohol dehydration on zeolites, such as alcohol dimeric species and

surface-bound alkoxide species, have been established on the basis of solid-state NMR and infrared spectroscopic studies [14-16] as well as calorimetric measurements [17] . However, the effects of zeolite topology on the rate and selectivity to olefin and ether synthesis have not been interpreted in terms of a mechanistic cycle and kinetics for unimolecular and bimolecular alcohol dehydration.

In our work, three zeolite framework materials (H-MFI, H-FER, and H-MOR) were chosen to study the effects of zeolite pore connectivity and channel size on the rate and selectivity of ethanol conversion. Steady-state kinetic measurements and isotopically-labeled ethanol were employed to explore the mechanism of ethanol dehydration on these materials. The results and detailed discussion will be presented in chapter 2 to demonstrate that the 8-membered ring (8-MR) pockets of H-MOR protect ethanol monomers from forming bulky ethanol dimers as shown in Figure 1.1, and thereby, propagate the selective unimolecular dehydration of ethanol to generate ethylene.

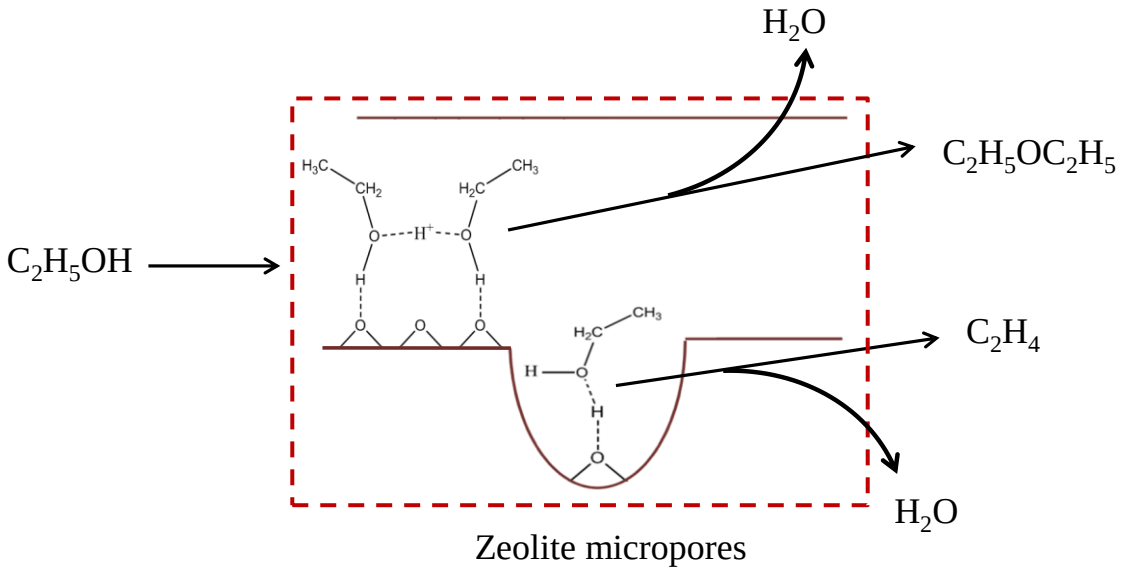

Figure 1.1. *Monomolecular and bimolecular ethanol dehydration in zeolite micropores.*

Alkane hydroisomerization catalyzed by bifunctional metal-acid formulations is an important reaction in petrochemical refining for transforming linear saturated hydrocarbons to branched hydrocarbons with higher octane rating. The mechanism and kinetics of bifunctional hydroisomerization have been extensively studied on solid acid

catalysts [18-20]. The generally accepted pathway of hydroisomerization based on the study by Weisz and Swegler [21] includes dehydrogenation of the linear alkane to form a linear alkene on the metal surface. This linear alkene is isomerized into a branched alkene on the acidic site in the zeolite micropore environment; subsequently, this branched alkene is hydrogenated over the metal catalyst to generate a branched alkane. Alkane isomerization can be catalyzed by only the acidic zeolite but high temperatures are required (573 K on zeolite BEA) [22] for initial dehydrogenation of the alkane, and, in absence of H_2 and metal catalysts, high concentrations of alkenes result in excessive oligomerization, cyclization, and aromatization reactions that form unreactive carbon deposits [22-25]. In bifunctional catalyst formulations, however, because the equilibrium of alkane, alkene, and hydrogen is established by platinum at lower temperatures (~473 K), low concentrations of olefins are maintained by adjusting the alkane to H_2 ratio in the feed [25].

The detailed mechanism for how linear alkenes are transformed into branched alkenes over acidic zeolites has also been extensively studied by computational chemistry methods. Hybrid quantum mechanical–molecular mechanical (QM/MM) calculations show that surface-bound, linear alkoxide intermediates formed upon chemisorption are more stable than physisorbed linear alkenes [26, 27] and that stability of the linear alkoxide increases with increasing carbon number in FER (C_3-C_5) [26] and FAU (C_2-C_8) [27]. Linear alkoxide species have been observed as stable intermediates in ^{13}C-NMR and infrared spectra during alcohol dehydration and protonation of alkenes on zeolite surfaces [14, 28, 29]. The isomerization of a linear alkoxide into a branch alkoxide occurs via an edge-protonated cyclo-propane species as a transition state which is energetically favored compared to directly shifting the alkyl group as shown by Demuth et al. [30] and Boronat et al. [31] using density functional theory (DFT).

In this work, three zeolite framework materials (H-BEA, H-FER, and H-MOR) were chosen to study the effects of zeolite pore connectivity, channel size, and location of OH groups on the rate and selectivity of n-hexane hydroisomerization over bifunctional catalysts consisting of physical mixtures of zeolites and Pt/Al_2O_3 (0.9-1.0 Pt/H^+ in molar ratio). The results and detailed discussion will be presented in chapter 3 to demonstrate

that the n-hexene is partially confined in the small 8-MR pockets of MOR as shown in Figure 1.2. This partial confinement of n-hexene in the small 8-MR pockets results in the selectivity of n-hexane isomatization selectivity and the activation entropy in small 8-MR side pockets of MOR being similar to that observed in the larger 12-MR channels of MOR.

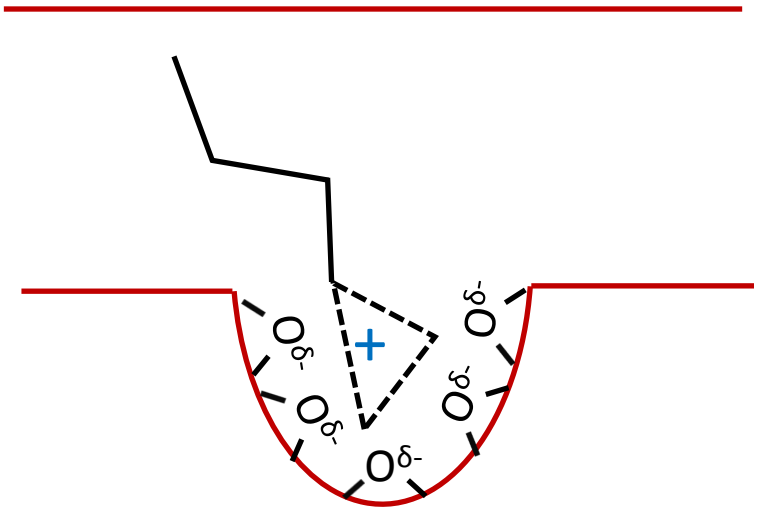

Figure 1.2. *The n-hexene molecule is partially confined in the 8-MR side pockets of MOR.*

1.3 Acid catalyzed reaction on γ-Al_2O_3

Gamma alumina (γ-Al_2O_3) is widely used in the chemical industry as an acid catalyst and a catalyst support for alcohol dehydration, hydrodesulfurization, and isomerization of olefins [1-4, 32] due to its high surface area (50-300 m^2/g) and its high thermal stability (stable at temperatures as high as 873 K [1, 4, 33]). The precursors of γ-Al_2O_3 are boehmite (γ-AlO(OH)), bayerite (α-$Al(OH)_3$), or gibbsite (γ-$Al(OH)_3$), which can be transformed into different transition aluminas such as gamma (γ), eta (η), theta (θ), etc. depending on the synthesis temperature [1, 33]. Thermal treatment of all these precursors and transition aluminas above 1473 K will transform all these materials into the most stable phase of alumina, a low surface area (3-5 m^2/g) material referred to as alpha (α) alumina [33]. The crystallographic structure of γ-Al_2O_3, a high surface area transitional

alumina commonly used as an industrial support and acid catalyst, is difficult to characterize due to its low crystallinity.

The surface of γ-Al_2O_3 possesses surface hydroxyl groups, Lewis acid sites, and basic sites [1, 34-38]. Lewis acid sites on γ-Al_2O_3 surface, which are three (Al_{III}), four (Al_{IV}), and five coordinated Al (Al_V), are generated by removal of surface hydroxyl groups as water from the γ-Al_2O_3 [39-41].

Both an E2-type mechanism and an E1-type mechanism have been proposed for ethylene formation for ethanol dehydration on γ-Al_2O_3 [42-47]. The E2-type mechanism includes (1) the adsorption of an alcohol on a Lewis acid site, (2) the adsorbed alcohol dehydrates through a transition state which breaks C_β-H and C_α-O bonds simultaneously, to form an olefin [43, 44, 47]. In an E1-type mechanism, the adsorbed alcohol is dissociated to form a surface-bound alkoxide species and a surface hydroxyl group, and subsequent desorption of this alkoxide species results in the formation of olefin [42, 46]. Whether olefin formation occurs via an E2- or an E1-type mechanism has not been determined because both of the two mechanisms are consistent with the observed primary isotope effects (KIE) for C_β-H bond cleavage and the zero order dependence in alcohol pressure [43, 44, 46]. For ether formation on γ-Al_2O_3, Knözinger [43] proposed a mechanism that comprises of the following sequence of steps (1) adsorption of an alcohol on a Lewis acid site; (2) the adsorbed alcohol is dissociated to form a surface-bound alkoxide species and a surface hydroxyl group; (3) the surface-bound alkoxide species reacts with a alcohol, which is physisorbed on neighboring a surface hydroxyl group, to form an ether. However, DeCanio et al. [45] concluded that ether formation is not due to the reaction between a surface-bound alkoxide and a physisorbed alcohol based on their observation that no desorption of alcohol was observed above 373 K in the temperature programmed desorption (TPD) of methanol, ethanol, 1-propanol and other alcohols. Due to the diversity and complexity of surface sites and the undetermined crystallographic structure, the mechanism and site requirements for alcohol dehydration on γ-Al_2O_3 have still not been determined.

In this work, the steady-state kinetic measurements and isotopic labeling were employed to explore the mechanism and site requirements of unimolecular and

bimolecular ethanol dehydration on γ-Al_2O_3. Pyridine, lutidine, and CO_2 were used as titrants to probe the involvement of acidic and basic centers in ethanol dehydration on γ-Al_2O_3. The results and detailed discussion will be presented in chapter 4 to demonstrate that ethylene formation occurs via an E1-type mechanism and diethyl ether formation involves the activation of a surface dimer species Figure 1.3.

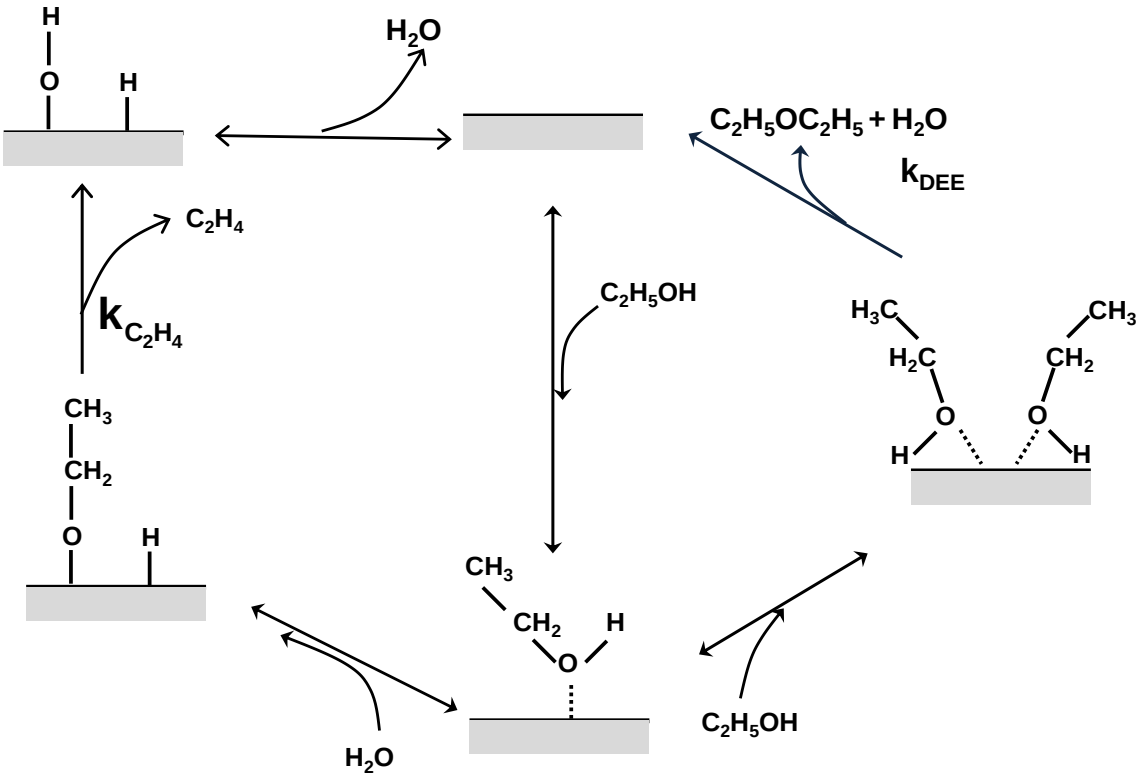

Figure 1.3. *Proposed elementary steps for DEE and ethylene formation for ethanol dehydration on γ-Al_2O_3.*

Chapter 2:

Catalytic consequences of hydroxyl group location on the rate and mechanism of parallel dehydration reactions of ethanol over acidic zeolites*

2.1. Introduction

Environmental issues drive the search for alternative sources of fuels and chemicals that are currently derived from petroleum. Plant biomass represents an abundant, carbon-neutral source that can be used to supply energy carriers and chemicals currently produced from crude oil [48]. Since most of plant biomass is comprised of carbohydrates, the intermediates derived from plant biomass typically contain OH groups. The selective removal of these OH groups via dehydration is one of the challenges for production of fuels and chemicals from biomass [49-53].

Proton-form zeolites are solid acid catalysts with channel and pocket dimensions typically less than 1nm. Zeolite topology can promote reaction rates and selectivity based on spatial constraints [10], attractive or repulsive interactions between adsorbed molecules and pore walls [11, 54], and by altering the relative stability of surface-bound intermediates inside mircopores [55]. The microporous host environment in zeolites enables them to be shape-selective catalysts and thus good candidates for selective dehydration of biomass-derived intermediates.

Ethanol dehydration was chosen as a probe reaction to develop a basic understanding of the effects of the size and connectivity of zeolite channels as well as OH group location within zeolite host environments on oxygen removal via dehydration reactions. Ethanol can be dehydrated through a unimolecular route to produce ethylene, or through a bimolecular pathway to generate diethyl ether (DEE) [56]. Wang et al. [14] showed that absorbed ethanol can be dehydrated into a surface-bound ethoxide species on zeolite H-Y using solid-state ^{13}C magic-angle spinning (MAS) NMR. In situ infrared

*Reported from H. Chiang, and A. Bhan, Journal of Catalysis 271 (2010) 251-261 © 2010 Elsevier Inc.

spectroscopic studies done by Kondo et al. [15] demonstrated that the desorption of surface-bound ethoxide species on zeolite H-MOR generates ethylene. Kondo et al. [15] introduced ethanol over H-MOR materials at 453 K to decompose ethanol to the surface-bound ethoxide species and water which was desorbed at 453 K. These authors heated the surface-bound ethoxide species on H-MOR and trapped all the desorbed gas phase species, and subsequently cooled down the temperature to 213 K to re-adsorb the trapped species again. The measured infrared spectrum of the re-adsorbed species at 213 K was nearly identical to the spectrum measured upon exposure to ethylene at 213 K. Zecchina et al. [16] used infrared spectroscopy to study the adsorption of ethanol on H-MOR and H-MFI. Based on the increase in intensity of the background and the Evans window in the infrared spectra, they concluded that two ethanol molecules co-adsorb on the same zeolitic OH group to form an ethanol dimeric species when the ratio of adducts/OH groups was higher than 1:1. The lack of change in the differential heat of adsorption of ethanol (~130 kJ mol^{-1}) at coverages higher than one ethanol molecule per aluminum led Lee and Gorte [17] to also conclude that dimeric ethanol species are absorbed on H-ZSM-5. De las Pozas et al. [57] studied ethanol conversion over zeolites H-HEU, H-MFI, H-MOR, H-LTL and H-FAU at 383 K and their results showed that only H-HEU and H-MOR materials, possessing 8-MR channels, convert ethanol to ethylene. Ethanol dehydration over zeolites and the effects of zeolite pore topology on ethanol dehydration reactions have already been studied [56-63], and the stability and identity of adsorption and reaction intermediates, such as ethanol dimeric species and surface-bound ethoxide species, have been established on the basis of solid state NMR and infrared spectroscopic studies [14-16] as well as calorimetric measurements [17]. The effects of zeolite topology on the rate and selectivity to ethylene and diethyl ether have not been interpreted in terms of a mechanistic cycle and kinetics for unimolecular and bimolecular ethanol dehydration.

In this work, three zeolite framework materials (H-MFI, H-FER and H-MOR) were chosen to study the effects of zeolite pore connectivity and channel size on the rate and selectivity of ethanol conversion. The measured kinetic effects of ethanol and ethylene pressure on DEE formation over these three zeolite materials show that ethanol dimers

are formed and that these dimeric species are subsequently dehydrated to form DEE. Ethylene formation was only observed on zeolites possessing 8-MR channels because 8-MR channels protect ethanol monomeric species and prevent the formation of ethanol dimeric species due to size restrictions.

2.2 Materials and methods

2.2.1 Catalyst preparation

MFI (Si/Al = 42.6, CBV 8014), FER (Si/Al = 11.5, CP 914c), and MOR (Si/Al = 11.1, CBV 21A) zeolite samples from Zeolyst, where the silicon to aluminum ratio was determined by elemental analysis (Galbraith Laboratories), in their NH_4^+ form were sieved to maintain particle sizes between 180 and 425μm (40-80 mesh) and subsequently treated in dry air (1.67 cm^3 s^{-1} at NTP conditions, ultrapure, Minneapolis Oxygen) by increasing the temperature from ambient to 773 K at 0.0167 K s^{-1} and holding for 4h to thermally decompose NH_4^+ to H^+ and $NH_{3(g)}$. The protonated MFI, FER, and MOR zeolite samples are abbreviated as H-MFI, H-FER and H-MOR, respectively.

2.2.2 Steady-state catalytic reactions of ethanol and ethanol-ethylene mixtures

Steady-state ethanol dehydration reactions were carried out in a tubular packed-bed quartz reactor (10 mm inner diameter) under atmospheric pressure and differential conditions (<1.5% conversion). Catalyst samples (0.05 g - 0.2 g) were supported on a coarse quartz frit inside the reactor, and the temperature was controlled using a furnace (National Electric Furnace FA120 type) connected to a Watlow Temperature Controller (96 series). Catalyst samples weighing less than 0.12 g were diluted with acid-washed quartz particles (0.5 g - 0.8 g, 160-630 μm, European Commission). Catalyst temperatures were measured using a K-type thermocouple touching the bottom of a well on the external surface of the quartz reactor. Catalyst samples were treated in He (1.67 cm^3 s^{-1}, ultrapure, Minneapolis oxygen) at 773 K (0.0167 K s^{-1}) for 3 h prior to cooling in He flow (~1.67 cm^3 s^{-1}) to reaction temperatures (358 K - 409 K). C_2H_5OH (≥99.5%, Sigma-Aldrich), C_2H_5OD (99.5 atom % D, Sigma-Aldrich) and C_2D_5OD (99.5 atom %

D, Sigma-Aldrich) reactants were introduced into flowing gas streams as a liquid using a syringe pump (Cole Parmer 74900 series). Liquid ethanol ($2.85x10^{-7}$ - $2.4x10^{-6}$ mol s^{-1}) was vaporized at 383 K into a gas flow which contained He (0.55-9.4 cm^3 s^{-1} at NTP condition) and a mixture of Ar/CH_4 (0.0137-0.0297 cm^3 s^{-1} at NTP conditions; 75% Ar and 25% CH_4, Minneapolis oxygen) as internal standards; transfer lines were maintained at temperatures greater than 343 K by resistive heating to prevent any condensation. The partial pressure of ethanol was changed by dilution with He (0.55-9.4 cm^3 s^{-1} at NTP condition, Ultrapure, Minneapolis oxygen). The partial pressures of ethanol and diethyl ether were always kept below their respective vapor pressures at ambient temperature to prevent condensation. Ethylene (0.0053-0.0883 cm^3 s^{-1} at NTP condition, chemically pure, MATHESON TRI-GAS) was introduced into the reactant stream after ethanol dehydration reactions achieved steady-state. The partial pressure of ethylene (0-1.6 kPa for H-MFI, 0-0.6 kPa for H-MOR and 0-4.5 kPa for H-FER) was changed by adjusting the flow rate of ethylene at a fixed ethanol pressure (1.4 kPa for H-MFI and H-FER; 1.0 kPa for H-MOR). The reactor effluent was sent via heated transfer lines to a mass spectrometer (MKS Cirrus 200 Quadrupole mass spectrometer system) or to a gas chromatograph (Agilent 6890N GC) equipped with a methyl-siloxane capillary column (HP-1, 50.0m x 320 μm x 0.52 μm) connected to a flame ionization detector and a packed column (SUPELCO HAYESEP R 80/100 mesh packed column, 12ft) connected to a thermal conductivity detector. Activation energies and pre-exponential factors were calculated from Arrhenius plots where the reaction rate constants were measured as a function of temperature (358-409 K).

2.3. Results and discussion

Ethylene and diethyl ether (DEE), products of unimolecular and bimolecular ethanol dehydration reactions, respectively, were observed on H-MOR (Si/Al = 11.1; temperature = 368 K; ethanol pressure = 0.3-6.0 kPa); however, ethanol conversion into ethylene was not observed over H-MFI (Si/Al = 42.6) and H-FER (Si/Al = 11.5) under these reaction conditions as shown in Figure 2.3.1. In the following paragraphs, we present mechanistic cycles for ethanol dehydration over different zeolite materials and interpret these marked

effects of zeolite structure on the selectivity of parallel ethanol dehydration reactions in terms of experimentally determined kinetic and thermodynamic parameters.

2.3.1 Kinetics and mechanism for ethanol dimerization into diethyl ether

The measured rates of DEE synthesis over H-FER, H-MFI and H-MOR as a function of ethanol pressure are shown in Figures 2.3.2-2.3.4. The rate of ethanol dimerization over the three zeolite materials increases with increasing ethanol pressure and then gradually approaches an upper limit. Two plausible mechanisms that would account for this observed pressure dependence were proposed for bimolecular ethanol dehydration. The first sequence of elementary steps for ethanol dimerization proposed by Phillips and Datta [56] is dimer-mediated (Figure 2.3.5) and includes ethanol adsorption on a Brønsted acid site to form an ethanol monomer (Step 1, Figure 2.3.5) and then co-adsorption of a second ethanol molecule on the same Brønsted acid site to form an ethanol dimer (Step 2, Figure 2.3.5). Subsequent dehydration of the two co-adsorbed molecules forms DEE and water and re-generates the acid site (rate-limiting step, Step 3, Figure 2.3.5). The second sequence of elementary steps for DEE synthesis referred to here as an ethoxide-mediated mechanism includes the adsorption of an ethanol molecule to form an ethanol monomer (Step 1, Figure 2.3.6), and the subsequent decomposition of this ethanol monomer into a surface-bound ethoxide species and water (Step 2, Figure 2.3.6). This ethoxide intermediate subsequently reacts with an ethanol molecule to form DEE (rate-limiting step, Step 3, Figure 2.3.6) and re-generates the Brønsted acid site. The ethanol dimer, which is formed by the co-adsorption of two ethanol monomers (Step 4, Figure 2.3.6), is considered to be an inactive species for the ethoxide-mediated mechanism.

The evidence for the existence of an ethanol dimer and for the surface-bound ethoxide species has already been reported in the literature. Zecchina et al. [16] studied the adsorption of methanol and ethanol over H-ZSM-5 and H-MOR zeolites using infrared spectroscopy. Based on observations in the infrared spectra, when the ratio of adducts/OH groups was higher than 1:1, (i) the intensity of the background and the Evans window increased; (ii) the band centered at 1650-1600 cm^{-1} broadened below 1300 cm^{-1},

and (iii) the intensity of the band at ~2980 cm^{-1} (A component) decreased and the band centered at ~2450 cm^{-1} (B component) broadened, the authors concluded that methanol and ethanol dimers are formed. Furthermore, the lack of change in the differential heat of adsorption of ethanol (~130 kJ mol^{-1}) at coverages higher than one ethanol molecule per aluminum led Lee and Gorte [17] to conclude that dimeric ethanol species are absorbed on H-ZSM-5. Absorbed ethanol can also be decomposed into a surface-bound ethoxide species and water on zeolite H-Y. Wang et al. [14] studied the adsorption and activation of ethanol over zeolite H-Y using in situ ^{13}C cross-polarization (CP) MAS NMR. Absorbed ethanol was heated from 295 K to 453 K. After using dry nitrogen to remove water and physisorbed ethanol at 453 K, a signal was observed at 72.6 ppm due to the formation of a new species. Since this new species could react with water, Wang et al. [14] concluded that this new species is a surface-bound ethoxide species.

Equations 2.3.1 and 2.3.2 are rate laws derived for the dimer-mediated mechanism (Figure 2.3.5) and the ethoxide-mediated mechanism (Figure 2.3.6), respectively, considering dimer activation to form DEE (Step 3, Figure 2.3.5) and the reaction of surface-bound ethoxide species with ethanol to form DEE (Step 3, Figure 2.3.6) to be kinetically-relevant (derivations included in the Supplementary Information). Both rate expressions are consistent with the observed zero-order ethanol pressure dependence for ethanol dimerization over the three zeolite materials (shown in Figures 2.3.2-2.3.4).

$$\frac{r_{C_2H_5OC_2H_5}}{[H^+]_0} = \frac{k_5 K_4 [C_2H_5OH]}{1 + K_4 [C_2H_5OH]} \tag{2.3.1}$$

$$\frac{r_{C_2H_5OC_2H_5}}{[H^+]_0} = \frac{k_3 K_2 [C_2H_5OH]}{[H_2O] + K_4 [H_2O][C_2H_5OH]} \tag{2.3.2}$$

The rate parameter k_5 is the intrinsic rate constant for dimer activation (Step 3, Figure 2.3.5); K_4 is the adsorption equilibrium constant for ethanol dimer formation (Step 2, Figure 2.3.5 and Step 4, Figure 2.3.6); k_3 is the rate constant for the reaction of surface-bound ethoxide species with ethanol (Step 3, Figure 2.3.6) and K_2 is the equilibrium constant for dehydration of the ethanol monomer (Step 2, Figure 2.3.6); $[H^+]_0$ is the number of initially accessible Brønsted acid sites and $[C_2H_5OH]$ is the partial pressure of ethanol.

The requirement of ethoxide species for DEE synthesis was probed in ethylene co-feed experiments. If the formation of DEE involves ethoxide species as intermediates (Figure 2.3.6), the rate of DEE synthesis should increase with increasing ethylene pressure because the coverage of ethoxide species increases with increasing pressure of ethylene. The measured rate of DEE synthesis as a function of ethylene pressure over H-MFI (ethanol pressure = 1.4 kPa, ethylene pressure = 0-1.5 kPa, T = 388 K) and H-MOR (ethanol pressure = 1.0 kPa, ethylene pressure = 0-0.57 kPa, T = 409 K) showed that ethylene has no kinetic effect on DEE synthesis rates (Figure 2.3.7 (a) and 2.3.7 (b)) implying that the dimer-mediated mechanism (Figure 2.3.5), which does not involve ethoxide intermediates, is prevalent on H-MFI and H-MOR.

In contrast, the rate of DEE synthesis over H-FER (ethanol pressure = 1.4kPa, ethylene pressure = 0-4.5 kPa, T = 368 K) increased linearly with increasing ethylene pressure (Figure 2.3.7 (c)). Using the quasi-equilibrium assumption for ethanol monomer and dimer formation and for the formation of ethoxide species formed upon dehydration of the ethanol monomer and upon ethylene adsorption, and the pseudo-steady-state approximation for all reactive intermediates for the ethoxide-mediated mechanism shown in Figure 2.3.6 gave a rate expression for DEE synthesis of the form shown in Equation 2.3.3. The derivation of Equation 2.3.3 is included in the Supplementary Information section.

$$\frac{r_{C_2H_5OC_2H_5}}{[H^+]_0} = \frac{k_3 K_e [C_2H_4]}{K_1 + K_1 K_4 [C_2H_5OH]} \qquad (2.3.3)$$

Where K_e is the equilibrium constant for ethanol adsorption to form the surface-bound ethoxide species; K_1 and K_4 are the equilibrium constants for ethanol monomer and dimer formation, respectively. This equation is inconsistent with the measured effects of ethylene pressure since the regression line has a non-zero intercept (7.5×10^{-6} mol DEE (mol H^+)$^{-1}$ s^{-1}) which is nearly identical to the rate of DEE synthesis (7.0×10^{-6} mol DEE (mol H^+)$^{-1}$ s^{-1}) measured using only ethanol under these reaction conditions (ethanol pressure = 1.4 kPa, T = 368 K) as reported in Figure 2.3.7 (c). Therefore, the rate equation for ethanol dimerization over H-FER should be comprised of two terms as shown in Equation 2.3.4.

$$\frac{r_{C_2H_5OC_2H_5}}{[H^+]_0} = \frac{k_5 K_4 [C_2H_5OH]}{1 + K_4 [C_2H_5OH]} + \frac{k_{ee} K_{co} [C_2H_4]}{1 + K_4 [C_2H_5OH]} \quad (2.3.4)$$

Where K_{co} is the equilibrium constant for the formation of co-adsorbed ethylene and ethanol complexes, and k_{ee} is the intrinsic rate constant for activation of the co-adsorbed ethylene and ethanol complex to form diethyl ether. The first term in Equation 2.3.4 represents the contribution from the dimer-mediated mechanism (Figure 2.3.5) and the second term represents the contribution from the activation of a co-adsorbed ethylene and ethanol complex to produce DEE. The co-adsorption of ethanol and ethylene is consistent with the observation that an alkene molecule interacts with an absorbed methanol molecule to form a co-absorbed methanol and alkene complex on a zeolitic OH group reported by Svelle et al. [64, 65]. These authors used density functional theory (DFT) with an added damped dispersion term to systematically investigate the adsorption of ethylene and methanol over zeolite clusters of varying sizes (3T to 38T) and found that the calculated energy for ethylene co-adsorption (-37 kJ mol^{-1}) on H-ZSM-5 is lower than the heat adsorption of ethylene (-24 kJ mol^{-1} to -31 kJ mol^{-1}).

The activation of co-absorbed ethylene and ethanol to form DEE may go through two pathways. One is the direct activation of the co-adsorbed ethylene and ethanol complex to form DEE. The second pathway involves the formation of an ethoxide intermediate upon ethylene adsorption and the subsequent reaction of this surface-bound ethoxide with a co-adsorbed ethanol to form DEE (Figure 2.3.8). These two pathways however, cannot be distinguished kinetically because their corresponding rate expressions have the same form as the second term of Equation 2.3.4.

The kinetic effects of ethylene on the rate of DEE synthesis over MFI, MOR and FER materials leads us to conclude that when only using ethanol as feed, the dimer-mediated mechanism is dominant. This is consistent with the observations made by Blaszkowski and van Santen [66] for conversion of methanol into dimethyl ether on the basis of DFT calculations done on a 3T cluster, which showed that the dimer-mediated mechanism had a lower energy barrier (145 kJ mol^{-1}) compared to the methoxide-mediated mechanism (215 kJ mol^{-1}). In presence of ethylene, the mechanism for DEE formation on FER

materials is different than that on MOR and MFI materials, implying that the rate and mechanism for DEE synthesis changes depending on zeolite structure.

Equation 2.3.1 can be written in a linear form as Equation 2.3.5, which accurately describes the kinetic effects of ethanol pressure on DEE formation over the three zeolite materials as shown by the linear dependence of inverse DEE synthesis rates on ethanol pressure (Figures 2.3.9-2.3.11). The values of the intrinsic rate constant for dimer activation (k_5, Step 3, Figures 2.3.5) and the equilibrium constant for dimer formation (K_4, Step 2, Figures 2.3.5) can be obtained from the values of the slope and the intercept and are listed in Table 2.3.1.

$$\frac{[C_2H_5OH][H^+]_0}{r_{C_2H_5OC_2H_5}} = \frac{1}{k_5K_4} + \frac{[C_2H_5OH]}{k_5} \qquad (2.3.5)$$

The regressed rate constant for activation of the ethanol dimer (k_5) increases with increasing pore size (H-MOR > H-MFI > H-FER [67]) and the order of regressed equilibrium constants (K_4) is H-MFI > H-MOR > H-FER. The much weaker adsorption of the ethanol dimer in H-FER (K_4 = 107) compared to H-MFI (K_4 = 1859) and H-MOR (K_4 = 313) suggests ethylene can co-adsorb on FER materials and thereby initiate another reaction cycle for DEE synthesis involving the reaction of co-adsorbed ethanol and ethylene in ethylene co-feed experiments described above.

2.3.2 Reactions of ethanol dehydration over H-MOR

In this work, ethanol conversion was carried out over H-FER, H-MFI and H-MOR, however, ethylene production was only observed over H-MOR materials as shown in Figure 2.3.1. The kinetic effects of ethanol pressure on the rate of ethylene synthesis were measured to understand the corresponding mechanism. The data reported in Figure 2.3.12 show that the rate of unimolecular dehydration of ethanol to ethylene decreases with increasing ethanol pressure and that the rate is nearly constant at higher ethanol pressures. This decrease in the rate of unimolecular dehydration of ethanol with increasing ethanol pressure (Figure 2.3.12) is consistent with the observations reported by Macht et al. [68, 69] for unimolecular dehydration of 2-butanol over heteropolyacid catalysts (HPA, $H_3PW_{12}O_{40}$). Macht et al. [68, 69] attributed the decrease in butanol

dehydration rates with increasing 2-butanol pressure to the formation of a 2-butanol dimeric species as inferred from their DFT calculations [70] that showed that the 2-butanol dimer is 84 kJ mol^{-1} more stable than the 2-butanol monomer. Similarly, Lee et al. [71] observed that the rate of unimolecular dehydration of ethanol to ethylene over HPA catalysts ($H_3PW_{12}O_{40}$) also decreased when ethanol pressure increased implying that ethanol dimers formed at high pressures inhibit the rate of ethylene synthesis. The negative kinetic effects of alcohol pressure on unimolecular dehydration rates over HPA catalysts are in agreement with our postulation that the ethanol dimer inhibits unimolecular dehydration reactions of ethanol over H-MOR.

The rate of ethylene synthesis over H-MOR does not decrease at higher pressures, suggesting that the location of some Brønsted acid sites protects ethanol monomers from forming ethanol dimers. We hypothesize that Brønsted acid sites located in small 8-MR side pockets in H-MOR protect ethanol monomers against the formation of ethanol dimers because of size exclusion; hence, the hydroxyl groups encapsulated in 8-MR pockets can selectively catalyze the unimolecular dehydration of ethanol to ethylene. Indirect evidence that 8-MR channels can prevent the inhibitory effects of ethanol dimeric species on ethylene production can be found in the report by de las Pozas et al. [57]. These authors carried out ethanol conversion over various zeolites (H-HEU, H-FAU, H-LTL, H-MOR and H-MFI**)** at the vapor pressure of ethanol at 273 K (1.6 kPa) and 383 K**,** and we note on the basis of selectivity and conversions reported by these authors that only H-HEU and H-MOR, materials that possess 8-MR channels, converted ethanol into ethylene.

Based on the hypothesis that the ethanol dimer is not formed in 8-MR channels, we propose that the mechanism for ethanol dehydration within 8-MR pockets in H-MOR is the same as the mechanism proposed by Kondo et al. [15]. This mechanism includes the adsorption of ethanol on a Brønsted acid site to form an ethanol monomer (Step 1, Figure 2.3.13) and subsequent decomposition of the ethanol monomer to form a surface-bound ethoxide intermediate and water (Step 2, Figure 2.3.13). Desorption of the surface-bound ethoxide intermediate generates ethylene and re-generates the surface Brønsted acid site (Step 3, Figure 2.3.13). The complete catalytic cycle for the conversion of ethanol into

ethylene and diethyl ether within 12-MR channels in MOR-type materials is shown in Figure 2.3.14. The mechanism includes the adsorption of ethanol to form an ethanol monomer (Step 1, Figure 2.3.14) and the subsequent decomposition of this ethanol monomer into a surface-bound ethoxide species and water (Step 2, Figure 2.3.14) or the subsequent co-adsorption of another ethanol molecule to form an ethanol dimer (Step 4, Figure 2.3.14). Desorption of the surface-bound ethoxide species generates ethylene (Step 3, Figure 2.3.14) and dimerization of the co-adsorbed ethanol monomers generates diethyl ether and water (Step 5, Figure 2.3.14).

The rate-limiting step for ethanol dehydration mechanisms in 8-MR pockets (Figure 2.3.13) and 12-MR channels (Figure 2.3.14) was probed using isotopic ethanol reactants (C_2H_5OD and C_2D_5OD) at 388 K as shown in Table 2.3.2. The rate of ethylene synthesis using C_2H_5OH is nearly identical to that measured using C_2H_5OD reactants (Table 2.3.2; $r_{C2H4,H}/r_{C2H4,D}$ = 1.1; ethanol pressure = 0.46-5.6 kPa; temperature = 388 K); however, the rate of ethylene synthesis decreased when using C_2D_5OD reactants (Table 2.3.2, $r_{C2H4,H}/r_{C2H4,D}$ = 1.5) under these reaction conditions. The estimated kinetic isotopic effect (KIE) value at 388 K is ~4.2 for C-H cleavage and ~5.7 for O_{zeo}-H bond cleavage, where O_{zeo} is the oxygen atom in the zeolite lattice; the estimated value of the KIE is ~1.3 for the re-hybridization of the α-carbon from sp^3 to sp^2 hybridization in the transition state for dehydration (Step 2 in Figure 2.3.13 and Figure 2.3.14; the estimation of the KIE is discussed in the Supplementary Information). Therefore, the small values of $r_{C2H4,H}/r_{C2H4,D}$ for both C_2H_5OD and C_2D_5OD reactants show that the rate-limiting step for ethylene production is not the desorption of the ethoxide (Step 3 in Figure 2.3.13 and Figure 2.3.14) which involves C-H bond cleavage. The decomposition of adsorbed ethanol into surface-bound ethoxide species and water (Step 2, Figure 2.3.13 and Figure 2.3.14) involves O_{zeo}-H bond and C-O bond cleavage. The small values of $r_{C2H4,H}/r_{C2H4,D}$ for both C_2H_5OD and C_2D_5OD noted above show that O_{zeo}-H bond cleavage is not involved in the kinetically relevant step. The $r_{C2H4,H}/r_{C2H4,D}$ = 1.5 for C_2D_5OD reactants is similar to the estimated value for α-carbon re-hybridization (sp^3 to sp^2), indicating that the transition state of the rate-limiting step for ethylene formation involves α-carbon re-hybridization. These observations are consistent with the KIE observed for 2-propanol

dehydration over HPA catalysts ($H_3PW_{12}O_{40}$) [69]. Macht et al. [69] used CD_3-CHOH-CD_3 and CD_3-CDOD-CD_3 as reactants at 343 K and the measured KIE values reported are 1.6 and 1.4 for CD_3-CHOH-CD_3 and CD_3-CDOD-CD_3, respectively. The secondary KIE values suggest that the transition state for 2-propanol dehydration over HPA catalysts involves the re-hybridization (sp^3 to sp^2) of the α-carbon in 2-propanol. These authors also observed that the order of measured rate constants for the dehydration of butanol isomers is 1-butanol (0.09×10^{-3} $(H^+ s)^{-1}$) << 2-butanol (60×10^{-3} $(H^+ s)^{-1}$) << tert-butanol (3300×10^{-3} $(H^+ s)^{-1}$). This order is the same as the order of carbenium-ion stability for the corresponding butanol isomers. In addition, the much larger rate constant of 1-butene isomerization (1.2 $(HPA\ s)^{-1}$) compared to that of 2-butanol dehydration (0.175 $(HPA\ s)^{-1}$) in their work suggests that the rate-limiting step is not the desorption of surface-bound butoxide intermediates [68]. Based on the secondary KIE measured for ethanol dehydration over H-MOR as well as the results reported for alkanol dehydration over HPA catalysts in the literature, we conclude that the rate-limiting step for unimolecular dehydration of ethanol in 8-MR pockets and in 12-MR channels in H-MOR is the decomposition of adsorbed ethanol into surface-bound ethoxide species and water (Step 2 in Figure 2.3.13 and Figure 2.3.14) via a carbenium-ion transition state.

The rate equation (Equation 2.3.6) for ethylene synthesis based on the proposed mechanism in 8-MR pockets (Figure 2.3.13) and 12-MR channels (Figure 2.3.14) is consistent with the measured ethanol pressure dependence of ethylene synthesis rates (Figure 2.3.12).

$$\frac{r_{C_2H_4}}{[H^+]_0} = \frac{x_{12MR} k_{2,12MR}}{1 + K_{4,12MR}[C_2H_5OH]} + x_{8MR} k_{2,8MR} \qquad (2.3.6)$$

where $k_{2,12MR}$ and $k_{2,8MR}$ are the intrinsic rate constants for dehydration of adsorbed ethanol to form surface-bound ethoxide species in 12-MR channels and in 8-MR pockets, respectively; x_{12MR} and x_{8MR} are the fraction of Brønsted acid sites in 12-MR channels and 8-MR pockets, and $K_{4,12MR}$ is the equilibrium constant for ethanol dimer formation inside 12-MR channels.

The values of $K_{4,12MR}$ evaluated from the ethanol pressure dependence of ethylene synthesis rates (Figure 2.3.12) from Equation 2.3.6 are comparable to the values of K_4

evaluated from the ethanol pressure dependence of diethyl ether synthesis rates over H-MOR (Equation 2.3.5; Figure 2.3.11) and a tabulated compilation of $K_{4,12MR}$ evaluated from these two independent data sets at different temperatures is reported in Table 2.3.3. This consistency in the value of the equilibrium constant for formation of ethanol dimeric species, $K_{4,12MR}$, supports the mechanism proposed in Figure 2.3.14.

No ethylene production is observed on H-MFI because ethanol monomeric species are further converted to energetically favorable ethanol dimers; hence the dehydration of ethanol results in the formation of diethyl ether instead of ethylene. Ethylene production is only observed on H-MOR among the three zeolites (H-MOR, H-FER and H-MFI) and the rate of ethylene synthesis does not decrease with increasing ethanol pressure on H-MOR (Figure 2.3.12), suggesting that the 8-MR side pockets are too small to form ethanol dimers. The undetectable ethylene production on H-FER materials are consistent with the observation that most of the Brønsted acid sites are located in the 10-MR channels of H-FER as reported by Eder and Lercher [72] based on the observation that the differential heat of adsorption of n-hexane is constant until the coverage achieved is ~0.9 molecules per acid site.

Zeolites without 8-MR (H-MFI, H-LTL and H-FAU) channels have also been shown to catalyze the dehydration of ethanol into ethylene at high temperatures (453 K) [57], suggesting that the adsorption of a second ethanol molecule becomes weaker (K_4 becomes small) and the rate constant for ethanol decomposition into surface-bound ethoxide species increases (k_2) at high temperatures. Bun et al. [60] showed that the rate of ethylene synthesis was inversely proportional to ethanol pressure over H-ZSM-5 at high temperatures (543 K) consistent with the rate equation derived from the mechanism shown in Figure 2.3.14 (the first term in Equation 2.3.6). On the basis of these observations, we suggest that the mechanism for ethanol dehydration within the 12-MR channels of H-MOR (Figure 2.3.14) is also the mechanism for ethanol dehydration over H-MFI. This mechanism is consistent with the zero-order dependence of DEE synthesis rates on ethanol pressure shown in Figure 2.3.3.

The intrinsic rate constant for ethylene synthesis over H-MOR at different temperatures was evaluated by nonlinear regression of Equation 2.3.6 (Figure 2.3.12). The activation

energy and pre-exponential for ethylene formation over H-MOR obtained by plotting the natural logarithm of regressed rate constants (k_2) versus the inverse temperature (368-409 K; Figure 2.3.15) are reported in Table 2.3.4. The intrinsic activation energy for ethylene synthesis in 8-MR channels is higher than that in 12-MR channels; however, the pre-exponential factor in 8-MR channels is higher than the pre-exponential factor in 12-MR channels. A plausible explanation for this observation is the partial adsorption of the reactant within 8-MR pockets as proposed by Gounder and Iglesia [23] to explain the larger activation energy and entropy of activation for propane dehydrogenation in 8-MR pockets compared to 12-MR channels of H-MOR.

Our results clearly show that bimolecular dehydration of ethanol preferentially occurs in large and medium-pore zeolites; in contrast, spatial constraints imposed by small pores only allow unimolecular dehydration of ethanol. The effects of pore size on unimolecular and bimolecular ethanol dehydration noted in this research resemble the effects of pore size on unimolecular and bimolecular m-xylene disproportionation reported by Clark et al. [12]. These authors used a hybrid quantum mechanical-molecular mechanical (QM/MM) method to determine that over large pore zeolites (H-FAU), the disproportionation reaction of m-xylene can go through either a methoxide-mediated unimolecular pathway or via a diphenylmethane-mediated bimolecular pathway. The formation of diphenylmethane however, is inhibited in medium pore zeolites (H-MFI and H-MOR) due to steric constraints; hence the methoxide-mediate pathway is preferred in these materials. These theoretical results reported by Clark et al. [12] are consistent with the intermediates of ethylbenzene disproportionation identified using ^{13}C magic angle spinning (MAS) NMR by Huang et al. [73]. In large pore H-FAU, the MAS NMR signal of bulky diphenylethane was detected (46 ppm) at 443 K. In medium-pore zeolite materials (H-MOR and H-MFI), surface-bound ethoxide was detected at 483 K (73 ppm), however, no NMR signal corresponding to diphenylethane intermediates was observed.

The effects of the location of zeolitic OH groups on the selectivity of parallel ethanol dehydration reactions, as seen with the 8-MR pockets of H-MOR selectively promoting ethylene synthesis, are in line with recent observations reported by Cheung et al. [74] and Bhan et al. [5, 75] for dimethyl ether carbonylation, and by Gounder and Iglesia [23] for

parallel reactions of unimolecular alkane activation. Cheung et al. [74, 76] noted that the zeolites (H-MOR and H-FER) with eight-membered-ring (8-MR) channels had a higher rate of dimethyl ether (DME) carbonylation than zeolites without 8-MR channels (H-BEA, H-FAU and H-MFI). Bhan et al. [5, 75] selectively replaced the zeolitic protons in 8-MR side pockets in H-MOR materials with Na^+ cations and noted that the rate of DME carbonylation scaled with the number of Brønsted acid sites within the 8-MR side pockets. Gounder and Iglesia [23] studied the unimolecular cracking and dehydrogenation of propane over H-MOR and Na-MOR at 748 K, and showed that rates for both cracking and dehydrogenation of propane within 8-MR pockets are higher than those in 12-MR channels.

The results of ethanol dehydration reactions studied in this research imply that the design and selection of microporous catalysts for performing shape-selective reactions of oxygenates requires us to consider the size and stability of the corresponding surface intermediates as well as the location of Brønsted acid sites.

2.4 Conclusions

Steady-state ethanol dehydration reactions over H-FER, H-MFI and H-MOR showed that H-MOR can catalyze ethanol conversion into both ethylene and diethyl ether, while H-FER and H-MFI can only catalyze bimolecular ethanol dehydration reactions. Ethanol-ethylene co-feed experiments showed that the rate of DEE synthesis over H-MFI and H-MOR is independent of ethylene pressure, suggesting that the mechanism for DEE synthesis involves the dimerization of co-adsorbed ethanol monomers instead of reactions of surface-bound ethoxide species intermediates with ethanol. The measured rates of DEE synthesis over H-FER as a function of ethylene pressure had a regression line where the value of the intercept was nearly identical to the rate of DEE synthesis measured using only ethanol as feed, suggesting that DEE formation on H-FER materials involves both dimerization of co-adsorbed ethanol monomers and the activation of co-absorbed ethylene and ethanol complexes. No ethylene production is observed on H-MFI and H-FER because ethanol monomeric species are further converted to energetically favorable ethanol dimers.

Ethylene production is only observed on H-MOR among the three zeolites studied (H-MOR, H-FER and H-MFI) and the rate of ethylene synthesis does not decrease with increasing ethanol pressure on H-MOR, suggesting that 8-MR side pockets protect ethanol monomers from forming ethanol dimers. Kinetic isotopic effects measured using deuterated ethanol reactants show that the rate-limiting step for ethylene formation is the decomposition of ethanol to form a surface-bound ethoxide species and water via a carbenium-ion transition state. The selectivity to ethylene and diethyl ether in parallel ethanol dehydration reactions is determined by the stability of intermediates, the size of zeolite channels and the location of Brønsted acid sites. In zeolite pores large enough to accommodate ethanol dimers, ethanol preferentially dehydrates via a bimolecular pathway to generate diethyl ether since the formation of ethanol dimeric species is energetically more favorable than the formation of ethanol monomers. In zeolite channels too small to accommodate the ethanol dimer, ethanol is dehydrated via a unimolecular reaction pathway to generate ethylene.

Acknowledgments: The authors acknowledge the financial support from a Discovery Grant from the Institute on the Environment. We also thank Mingwei Tian for assistance with the reaction studies.

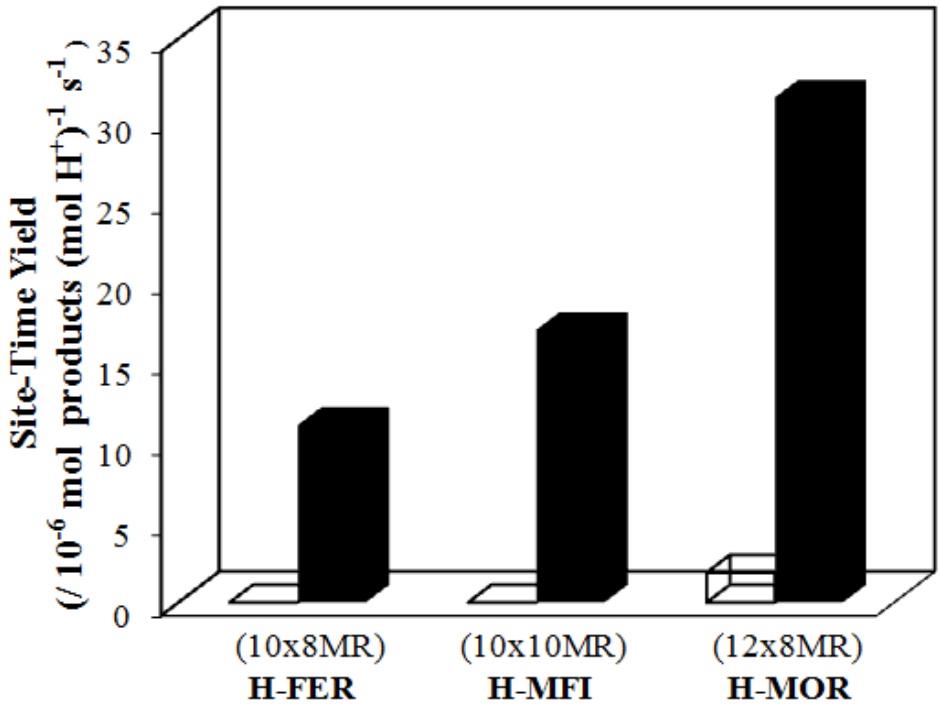

Figure 2.3.1. The rate of DEE (black bars) and ethylene synthesis (white bars) at 368 K and 5 kPa ethanol pressure.

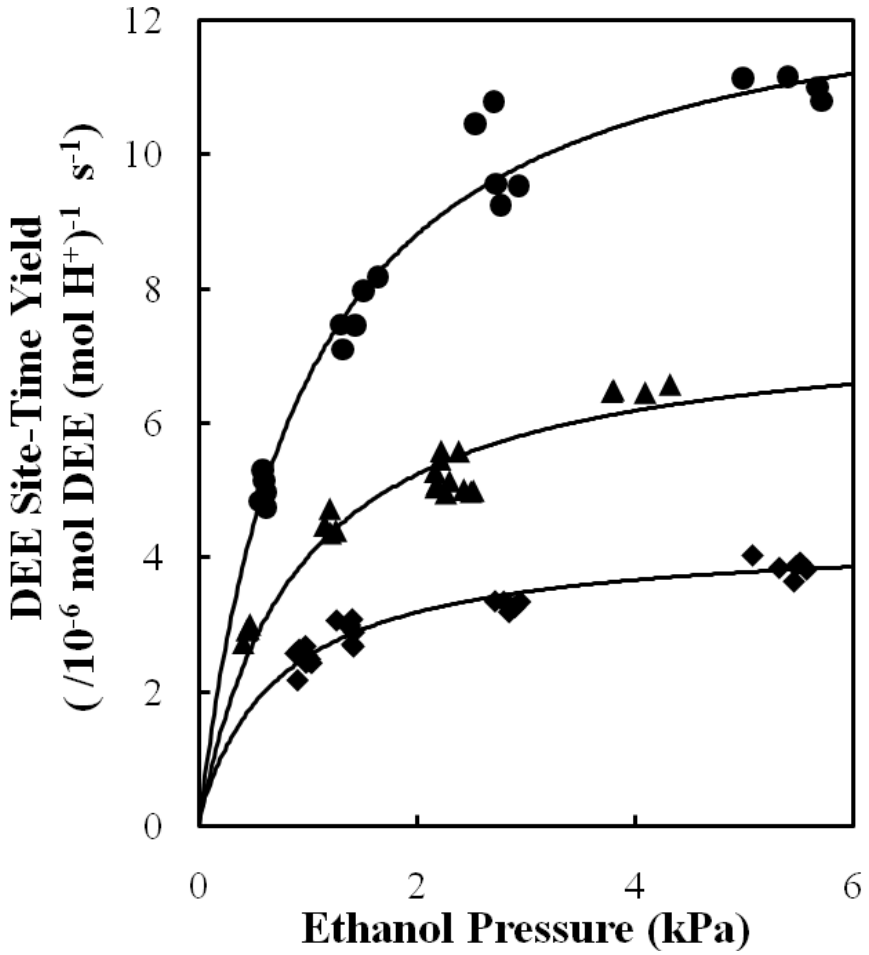

Figure 2.3.2. Measured diethyl ether (DEE) synthesis rate as a function of ethanol pressure over H-FER (Si/Al = 11.5) at 358 K (◆), 363 K (▲), and 368 K (●). The solid lines represent predictions from Equation 2.3.1.

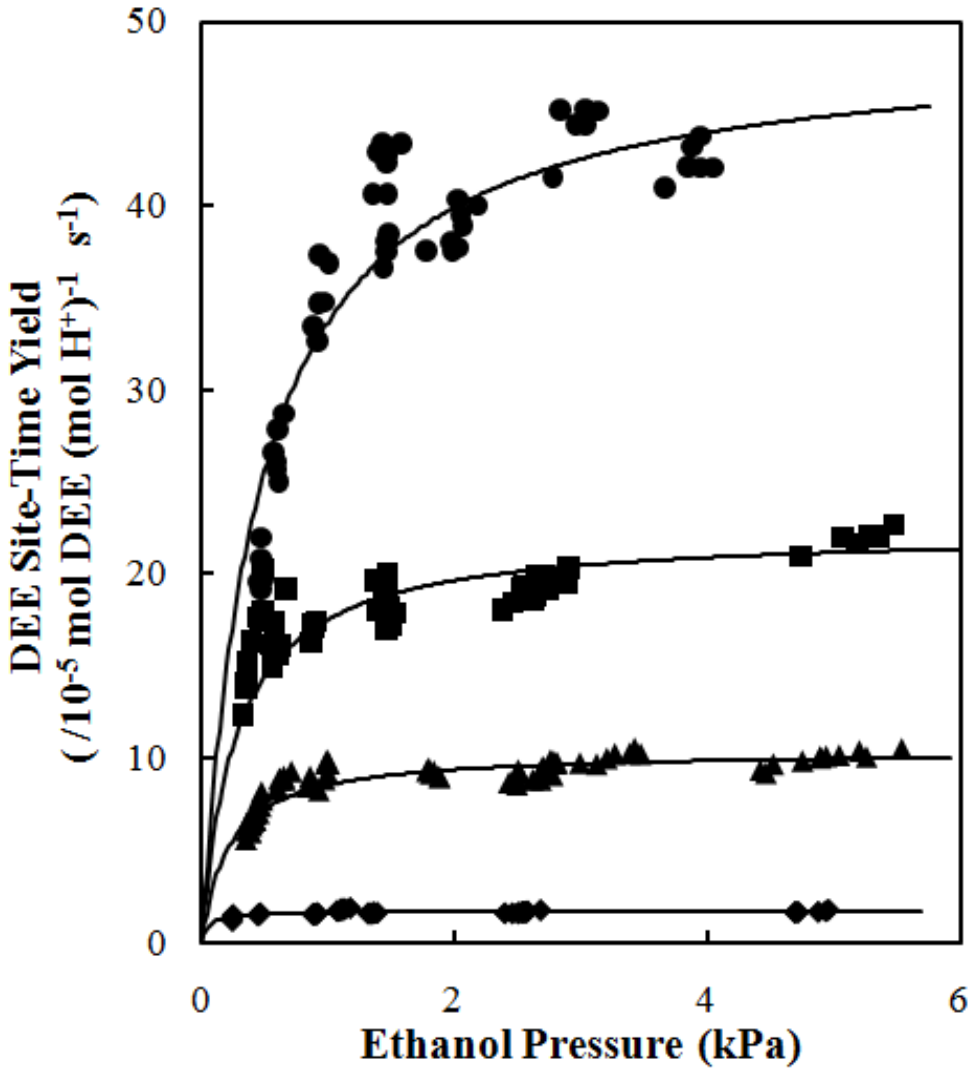

Figure 2.3.3. Measured diethyl ether (DEE) synthesis rate as a function of ethanol pressure over H-MFI (Si/Al = 42.6) at 368 K (◆), 388 K (▲), 398 K (■), and 409 K (●). The solid lines represent predictions from Equation 2.3.1.

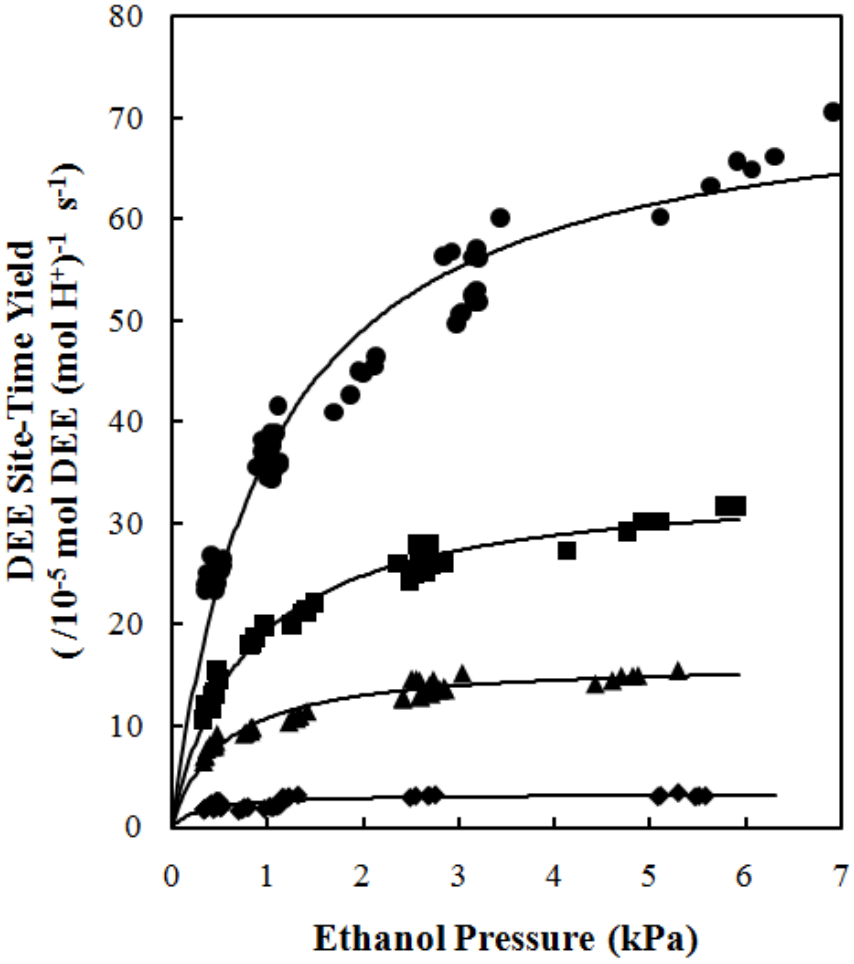

Figure 2.3.4. Measured diethyl ether (DEE) synthesis rate as a function of ethanol pressure for ethanol dehydration over H-MOR (Si/Al = 11.1) at 368 K (◆), 388 K (▲), 398 K (■), and 409 K (●). The solid lines represent predictions from Equation 2.3.1.

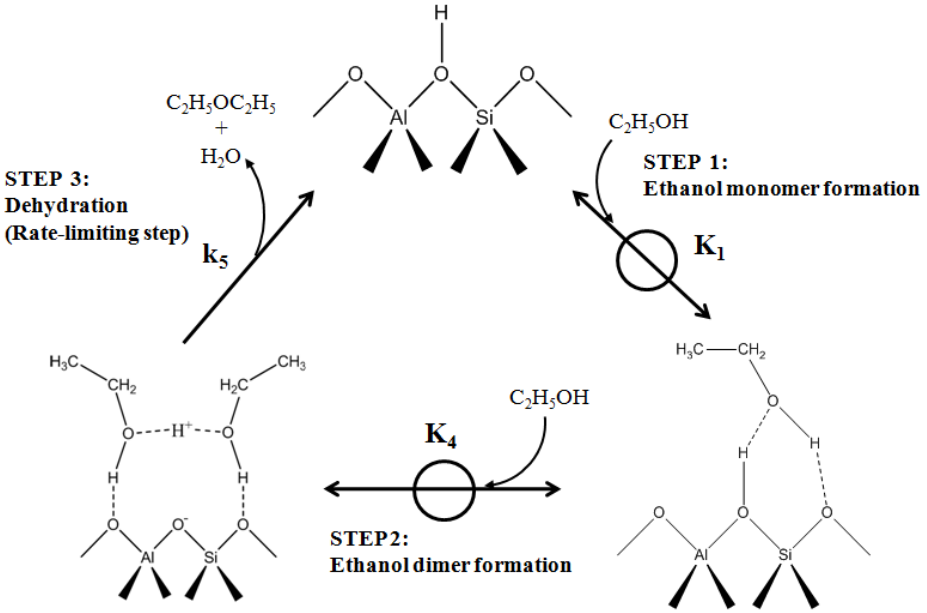

Figure 2.3.5. Proposed elementary steps for ethanol dimerization into diethyl ether via dimer activation over H^+ sites encapsulated in zeolite micropores.

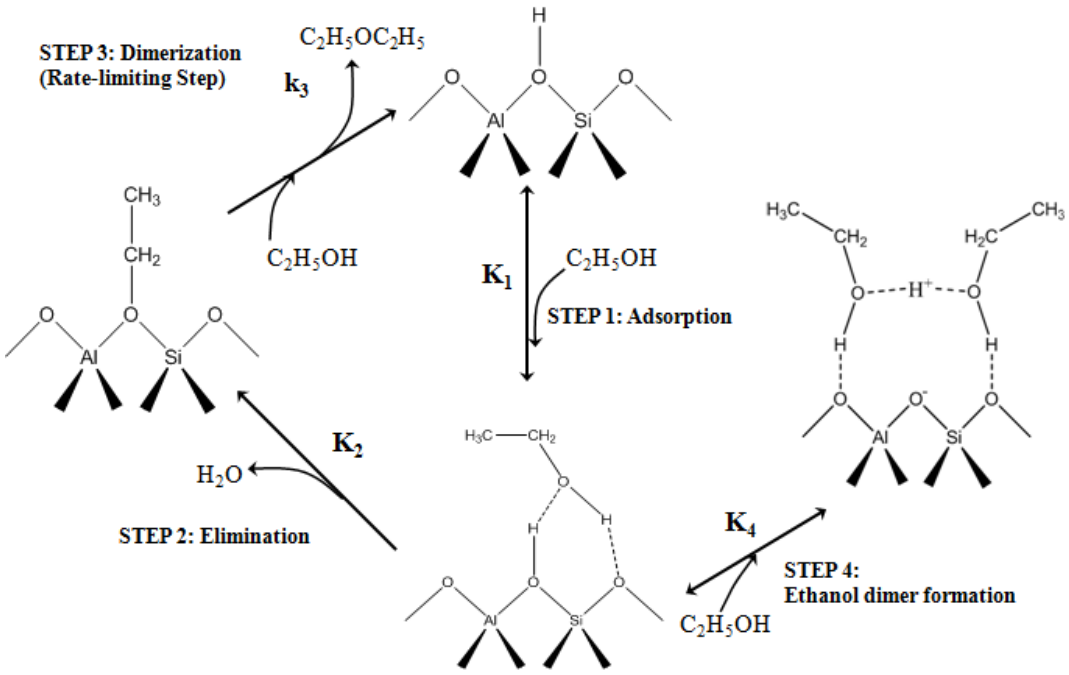

Figure 2.3.6. Proposed mechanism for ethanol conversion into diethyl ether via the formation of surface-bound ethoxide over H^+ sites encapsulated in zeolite micropores.

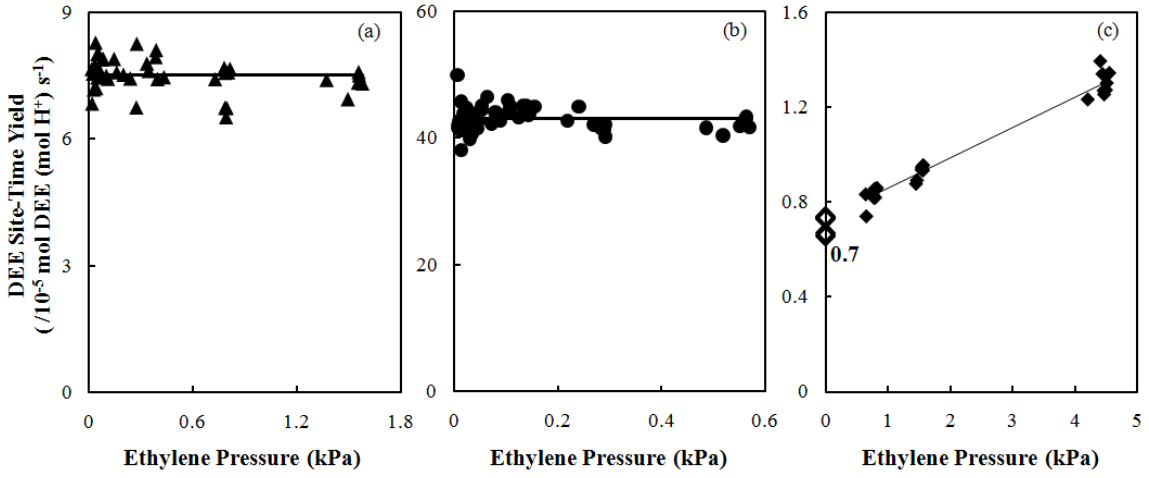

Figure 2.3.7. (a) the rate of DEE synthesis as a function of ethylene pressure over H-MFI (Si/Al = 42.6) at ethanol pressure = 1.4 kPa and T = 388 K (▲), (b) the rate of DEE synthesis as a function of ethylene pressure over H-MOR (Si/Al = 11.1) at ethanol pressure = 1.0 kPa and T = 409 K (●), (c) the rate of DEE synthesis as a function of ethylene pressure over H-FER (Si/Al = 11.5) at ethanol pressure = 1.4 kPa and T = 368 K (◆); the rates of DEE synthesis (average value = 7.0 x 10^{-6} mol DEE (mol H^{+})$^{-1}$ s^{-1}) using only ethanol at ethanol pressure = 1.4 kPa and T = 368 K (◇).

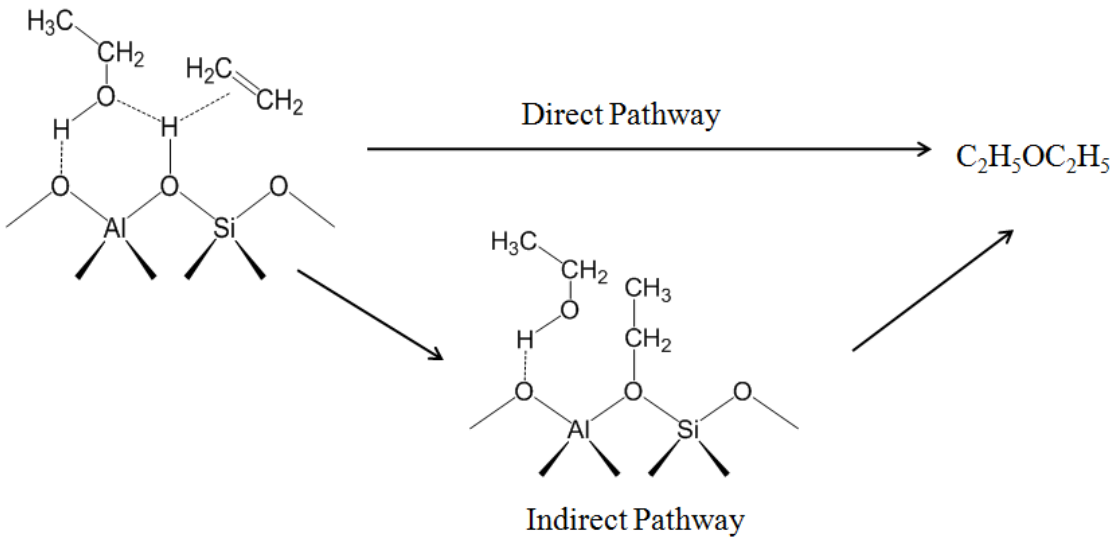

Figure 2.3.8. Direct and indirect routes for activating co-absorbed ethylene and ethanol to form diethyl ether over FER-type zeolites.

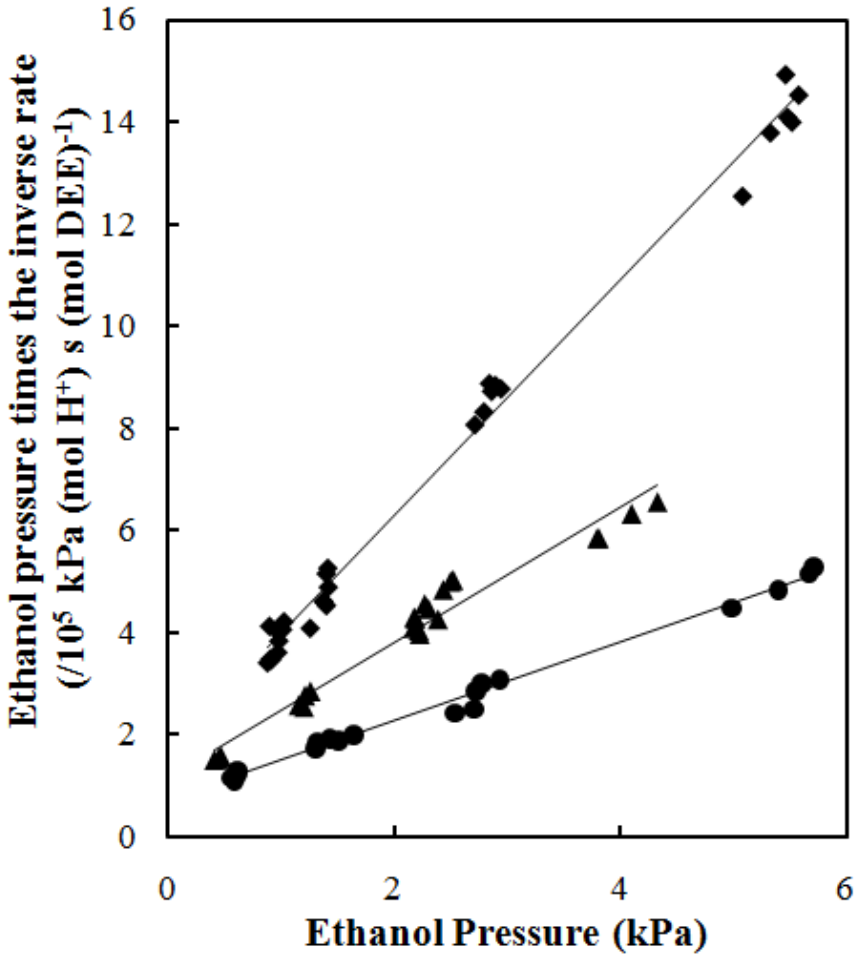

Figure 2.3.9. Ethanol pressure times the inverse rate of diethyl ether (DEE) synthesis as a function of ethanol pressure over H-FER (Si/Al = 11.5) at 358 K (◆), 363 K (▲) and 368 K (●).

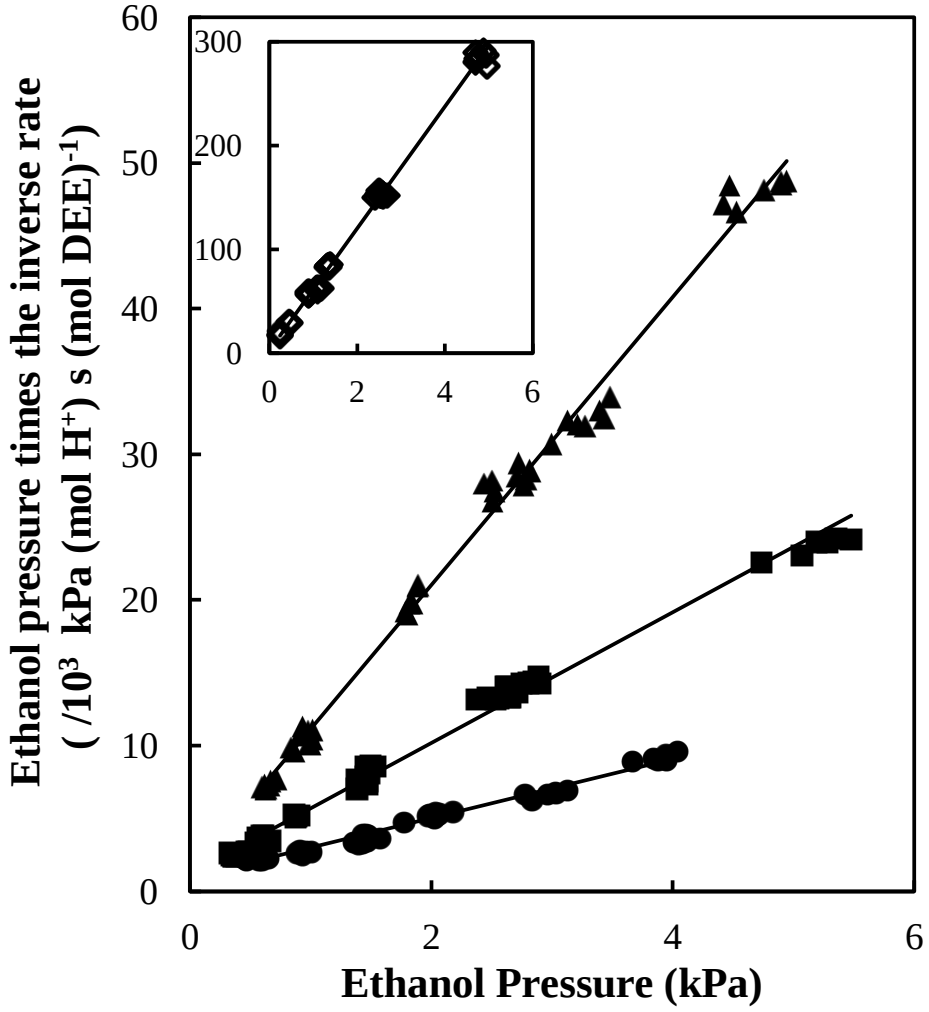

Figure 2.3.10. Ethanol pressure times the inverse rate of diethyl ether (DEE) synthesis as a function of ethanol pressure over H-MFI (Si/Al = 42.6) at 368 K (◇), 388 K (▲), 398 K (■), and 409 K (●).

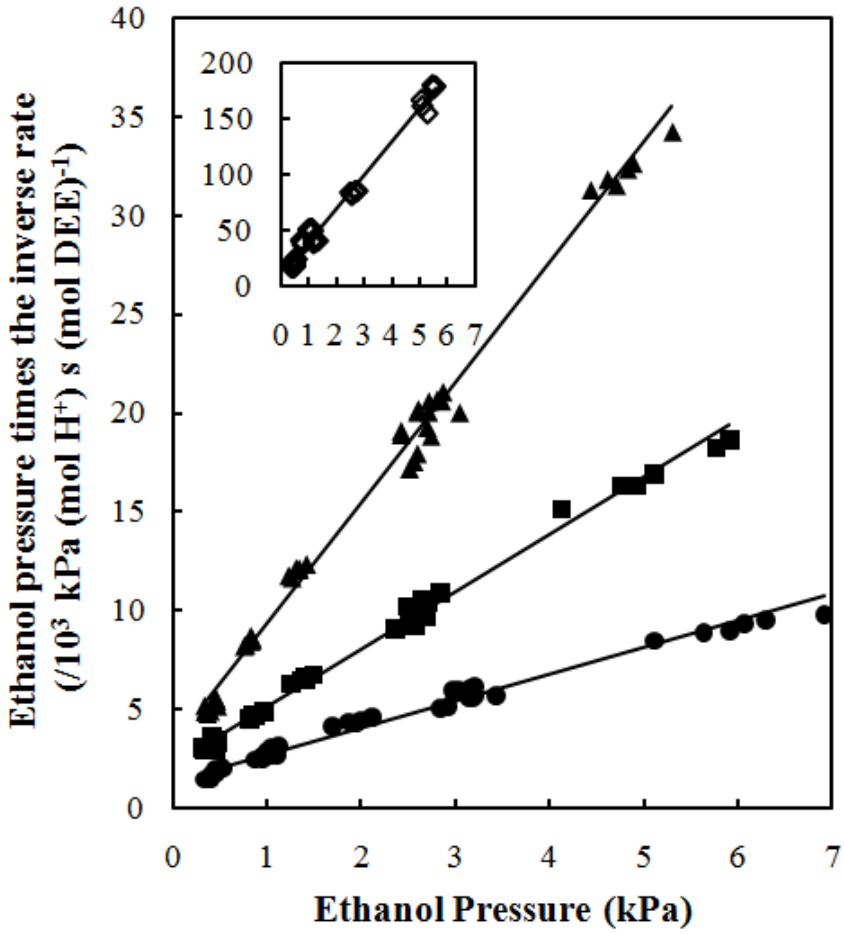

Figure 2.3.11. Ethanol pressure times the inverse rate of diethyl ether (DEE) synthesis as a function of ethanol pressure over H-MOR (Si/Al = 11.1) at 368 K (◇), 388 K (▲), 398 K (■), and 409 K (●).

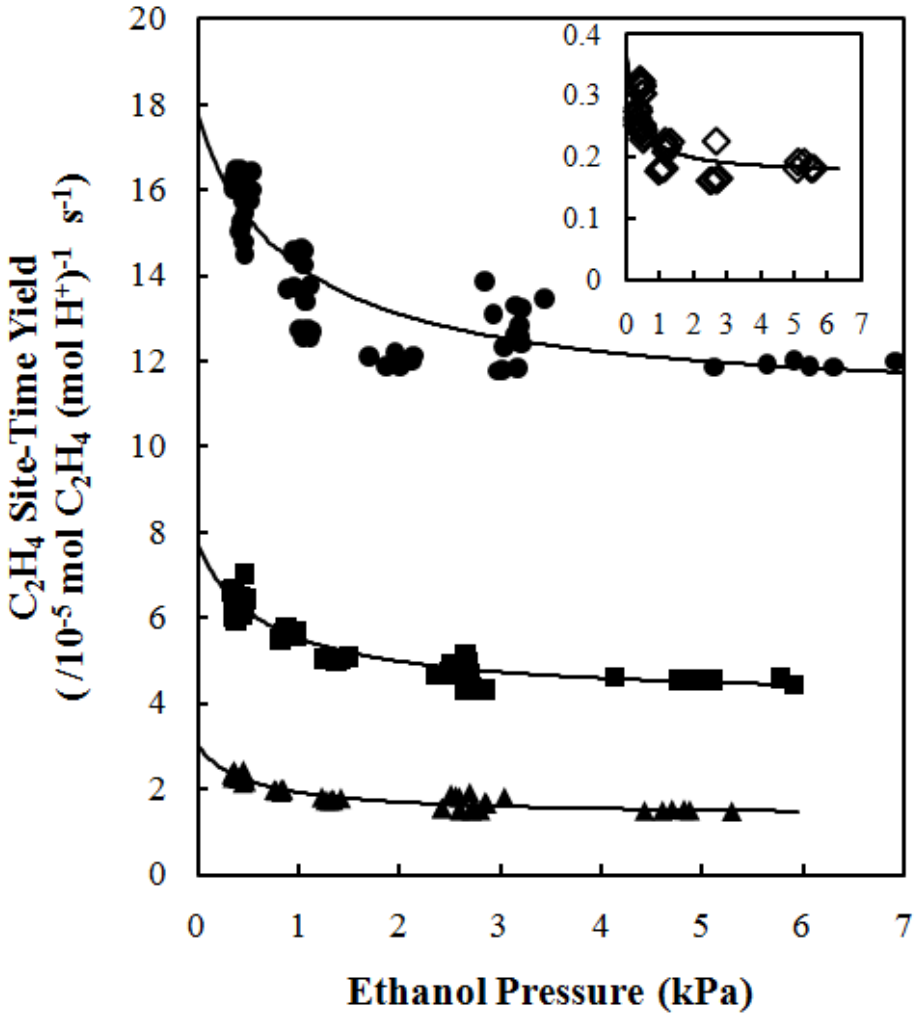

Figure 2.3.12. Ethylene synthesis rate as a function of ethanol pressure over H-MOR (Si/Al = 11.1) at 368 K (◇), 388 K (▲), 398 K (■), and 409 K (●). The solid lines present predictions from Equation 2.3.6.

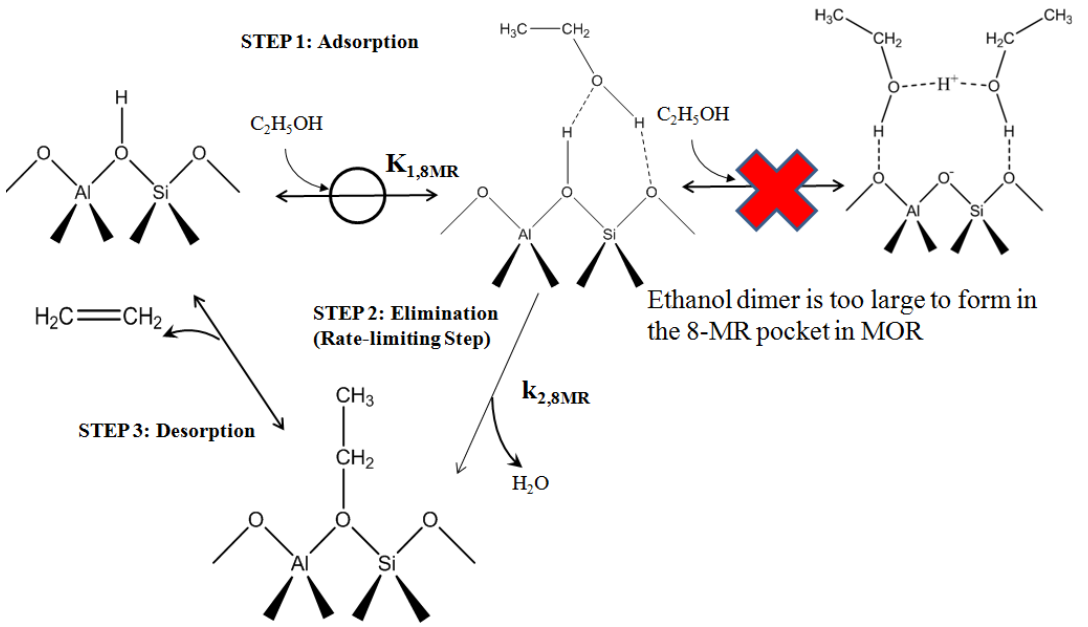

Figure 2.3.13. Proposed elementary steps for ethanol dehydration into ethylene within the 8-MR side pockets in MOR-type zeolites.

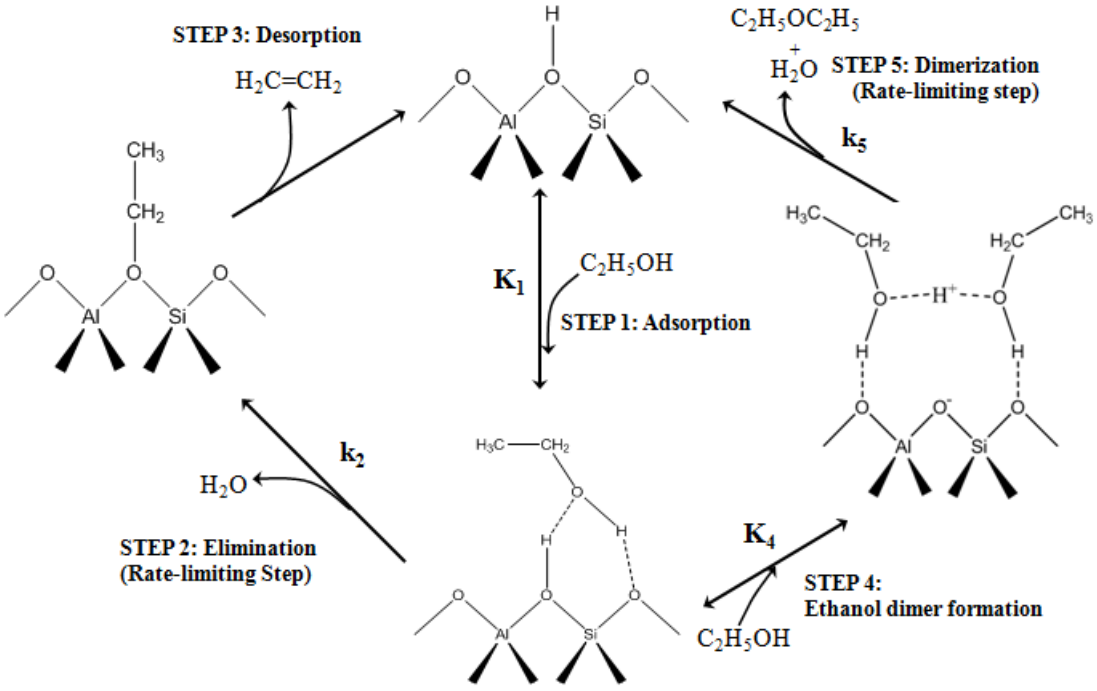

Figure 2.3.14. Proposed mechanism for ethanol conversion into ethylene and diethyl ether in the 12-MR channels in MOR-type zeolites.

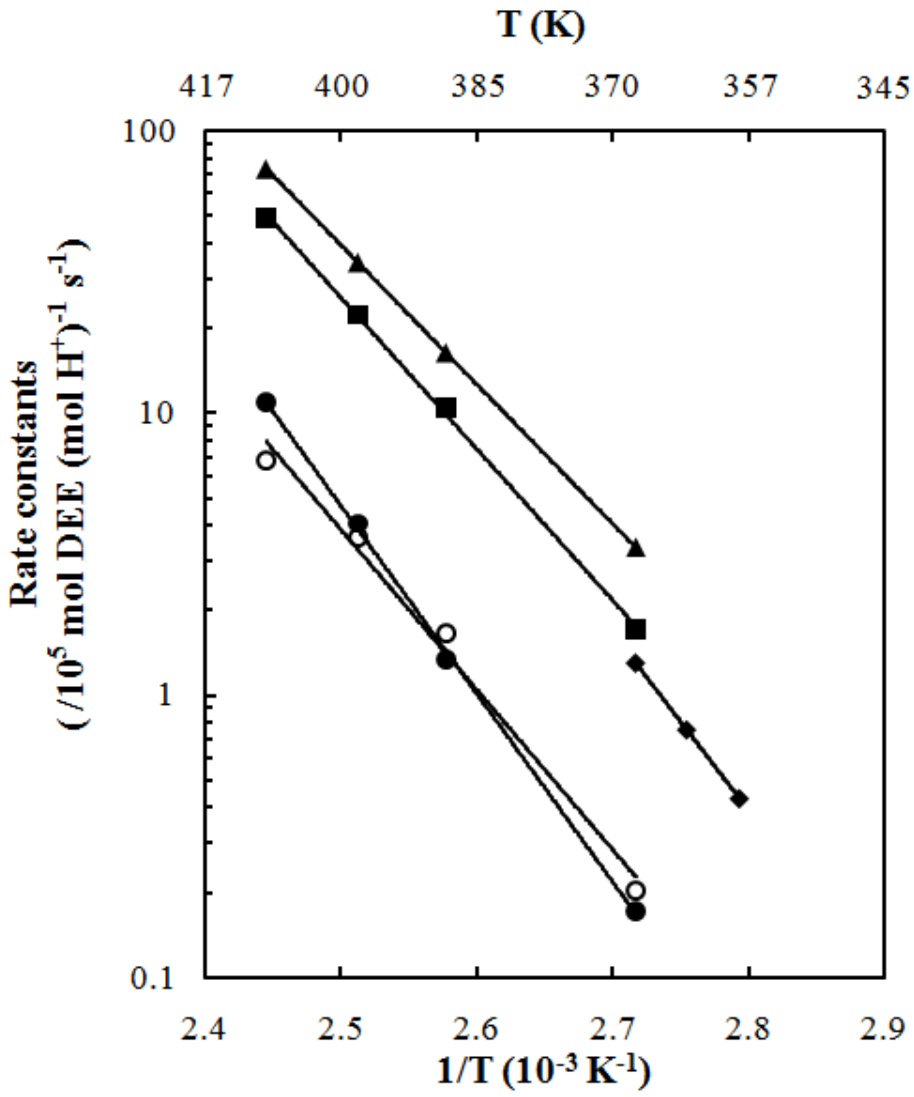

Figure 2.3.15. Measured intrinsic rate constant of DEE synthesis, k_5, over H-FER (◆), H-MFI (■), and H-MOR (▲); measured rate constants of ethylene production by 8-MR pockets (●), and by 12-MR channels (○) in H-MOR.

Table 2.3.1. Rate constants (k_5) and adsorption constants (K_4) for DEE synthesis at 368 K over the three types of zeolite frameworks.

Zeolite (Si/Al)	K_4	k_5 (/10^{-5} mol DEE (mol H^+)$^{-1}$ s^{-1})
H-FER(11.5)	107	1.3
H-MFI(42.6)	1859	1.7
H-MOR(11.1)	313	3.3

Table 2.3.2. The measured rates of ethylene synthesis (r_{C2H4}) using C_2H_5OH (EtOH), C_2H_5OD ($EtOD_1$) and C_2D_5OD ($EtOD_6$) at different pressures at 388 K.

	Pressure (kPa)	r_{C2H4} (10^{-5} (H^+ s)$^{-1}$)	$r_{C2H4,H}/r_{C2H4,D}$*
EtOH	2.7	1.8	-
$EtOD_1$	2.8	1.7	1.1
$EtOD_6$	2.8	1.2	1.5
EtOH	4.8	1.5	-
$EtOD_1$	5.6	1.5	1.1
$EtOD_6$	5.2	1.1	1.5
EtOH	0.46	2.3	-
$EtOD_1$	0.53	2.5	0.9
$EtOD_6$	0.51	1.6	1.4

* Subscript H means that reactant has no deuterium atoms and subscript D means that the reactant contains deuterium atoms

Table 2.3.3. Comparison of the adsorption constant, K_4, from ethylene production data and diethyl ether synthesis data over H-MOR (Si/Al = 11.1).

T(K)	$K_{4,12MR}$ (from C_2H_4)	K_4 (from DEE)
409	108	101
398	150	133
388	191	194
368	332	313

Table 2.3.4. Rate constants of ethylene production (k_2) at 388K, intrinsic activation energy of ethylene synthesis (E_{int}) and pre-exponential factor of ethylene synthesis over the three types of zeolite frameworks. x is the fraction of acid sites in 8-MR pockets or 12-MR channels.

H-MOR	**xk_2 (/ 10^{-5} mol C_2H_4 (mol H^+)$^{-1}$ s^{-1})**	**E_{int} (kJ mol^{-1})**	**Pre-exponential Factor (mol C_2H_4 (mol H^+)$^{-1}$ s^{-1})**
8-MR	1.3	128±10	$2.1x10^{12}$
12-MR	1.7	109±33	$5.8x10^{9}$

Chapter 3:

Catalytic consequences of hydroxyl group location on the kinetics of n-hexane hydroisomerization over acidic zeolites*

3.1. Introduction

The rates and selectivity of solid acid-catalyzed reactions are functions of the catalyst structure and acid strength. Since the acid strength of high-silica zeolites is almost invariant as assessed by calculations of the deprotonation energy (range: 1170-1200 kJ mol^{-1}) [77, 78], reactions of hydrocarbons catalyzed by high-silica zeolites are mainly affected by the micropore structure [9, 11, 13].

The zeolite environment that circumscribes acidic OH groups can result in remarkable differences in catalytic rates and selectivities that have been broadly described by the term shape selectivity and its specific manifestations such as "active site shape selectivity" and "restricted transition state selectivity" [5, 11]. Emerging research has particularly focused on the disparate OH group environments in 12- and 8-membered ring (MR) channels of MOR and the ability of OH groups in 8-MR channels to enable site specific catalysis for carbonylation of methyl groups and monomolecular dehydrogenation of alkanes as demonstrated in the recent work of Iglesia and co-workers [5, 23, 74, 75, 79]. We have shown that OH groups in 8-MR channels in MOR selectively dehydrate ethanol to ethylene because 8-MR pockets in MOR protect ethanol monomers from forming larger and more stable ethanol dimers due to size restrictions [80]. These recent examples in the literature demonstrate that hydroxyl groups circumscribed in smaller 8-MR channels of MOR catalyze reactions with rates and selectivity higher/different than in larger 12-MR channels of MOR for acid-catalyzed reactions mediated by charge, entropy, or size as specific considerations. In this work, we extend the scope of these recent reports to demonstrate the catalytic consequences of OH group environment on bifunctional n-hexane hydroisomerization reactions and

---

*Reported from H. Chiang, and A. Bhan, Journal of Catalysis 283 (2011) 98-107 © 2010 Elsevier Inc.

quantitatively discern enthalpic and entropic drivers for this reaction.

Alkane hydroisomerization catalyzed by bifunctional metal-acid formulations is an important reaction in petrochemical refining for transforming linear saturated hydrocarbons to branched hydrocarbons with higher octane rating. The mechanism and kinetics of bifunctional hydroisomerization have been extensively studied on solid acid catalysts [18-20]; we use it here as a probe reaction to assess whether the same mechanism is prevalent on acidic sites in all zeolite environments and to quantitatively assess how kinetic parameters within the proposed mechanism vary with OH group environment. The generally accepted pathway of hydroisomerization based on the study by Weisz and Swegler [21] includes dehydrogenation of the linear alkane to form a linear alkene on the metal surface. This linear alkene is isomerized into a branched alkene on the acidic site in the zeolite micropore environment; subsequently, this branched alkene is hydrogenated over the metal catalyst to generate a branched alkane. Alkane isomerization can be catalyzed by only the acidic zeolite but high temperatures are required (573 K on zeolite BEA) [22] for initial dehydrogenation of the alkane, and in absence of H_2 and metal catalysts, high concentrations of alkenes result in excessive oligomerization, cyclization, and aromatization reactions that form unreactive carbon deposits [22-25]. In bifunctional catalyst formulations, however, because the equilibrium of alkane, alkene, and hydrogen is established by platinum at lower temperatures (~473 K), low concentrations of olefins are maintained by adjusting the alkane to H_2 ratio in the feed [25].

The detailed mechanism for how linear alkenes are transformed into branched alkenes over acidic zeolites has also been extensively studied by computational chemistry methods. Hybrid quantum mechanical–molecular mechanical (QM/MM) calculations show that surface-bound, linear alkoxide intermediates formed upon chemisorption are more stable than physisorbed linear alkenes [26, 27] and that the stability of the linear alkoxide increases with increasing carbon number in FER (C_3-C_5) [26] and FAU (C_2-C_8) [27]. Linear alkoxide species have been observed as stable intermediates in ^{13}C-NMR and infrared spectra during alcohol dehydration and protonation of alkenes on zeolite surfaces [14, 28, 29]. The isomerization of a linear alkoxide into a branch alkoxide occurs via an

edge-protonated cyclo-propane species as a transition state which is energetically favored compared to directly shifting the alkyl group as shown by Demuth et al. [30] and Boronat et al. [31] using density functional theory (DFT).

In this study, three zeolite framework materials (H-BEA, H-FER, and H-MOR) were chosen to study the effects of zeolite pore connectivity, channel size, and location of OH groups on the rate and selectivity of n-hexane hydroisomerization over bifunctional catalysts consisting of physical mixtures of zeolites and Pt/Al_2O_3 (0.9-1 Pt/H^+ in molar ratio). The measured rate of isomerization over the three zeolite materials is a function of $n\text{-}C_6H_{14}/H_2$ (molar ratio), consistent with a bifunctional mechanism involving the facile dehydrogenation of n-hexane on the metal catalyst and a kinetically-relevant step involving isomerization of n-hexene on zeolitic acidic sites. Zeolite BEA has the highest rate among the zeolites considered because it has a lower activation energy than MOR and higher activation entropy than FER. The rate per proton in the 8-MR side pockets in MOR is five times higher than the rate in the 12-MR channels because the activation energy in 8-MR pockets is lower than that in 12-MR channels. The measured entropy of activation (-34.7 ± 9.8 J mol^{-1} K^{-1}) and selectivity to 2-MP and 3-MP (1.55:1) in the 8-MR pockets within MOR are similar to those in the 12-MR channels of MOR (-37.4± 9.7 J mol^{-1} K^{-1} and 1.5:1) and of BEA (-33.1± 4.3 J mol^{-1} K^{-1} and 1.35:1) suggesting that the n-hexene molecule is only partially confined in the 8-MR pockets of H-MOR.

3.2. Materials and methods

3.2.1 Catalyst preparation

FER (Si/Al = 11.5, CP 914c), MOR (Si/Al = 11.1, CBV 21A), and BEA (Si/Al=12.0, CP 814 E) zeolite samples from Zeolyst, where the silicon to aluminum ratio (Si/Al) was determined by elemental analysis (Galbraith Laboratories), in their NH_4^+ form were sieved to maintain particle sizes between 180 and 425μm (40-80 mesh) and subsequently treated in dry air (1.67 cm^3 s^{-1} at NTP conditions, ultrapure, Minneapolis Oxygen) to thermally decompose NH_4^+ to H^+ and $NH_{3(g)}$ by increasing the temperature from ambient

to 773 K at 0.0167 K s^{-1} and holding for 4h. The proton form FER, MOR, and BEA zeolite samples are abbreviated as H-FER, H-MOR, and H-BEA, respectively.

γ-Al_2O_3 (Sasol North America Inc., Lot # C1964, 189 m^2 g^{-1}, 0.44 cm^3 g^{-1} pore volume) was treated in flowing dry air (1.67 cm^3 s^{-1} at NTP conditions, ultrapure, Minneapolis Oxygen) to 923 K for 3 h (0.083 K s^{-1}) before adding the metal precursor. Pt/Al_2O_3 formulations (1.5 wt % Pt) were prepared by the incipient wetness impregnation of γ-Al_2O_3 using chloroplatinic acid solution (H_2PtCl_6•$6H_2O$, 99.95% (metal basis), Alfa Aesar) as precursor. After impregnation, samples (yellow in color) were treated in dry air (1.67 cm^3 s^{-1} at NTP conditions, ultrapure, Minneapolis Oxygen) at 383 K for 9h and subsequently heated to 823 K (0.083 K s^{-1}) for 4h to thermally decompose the precursors. After decomposing the precursor, the sample was treated in H_2 (3.3 cm^3 g^{-1} s^{-1}, ultra-pure carrier grade, Airgas) at 723 K (0.083 K s^{-1}) for 2 h and then cooled to ambient temperatures in dry He flow (1.67 cm^3 s^{-1}, ultrapure, Minneapolis oxygen). The Pt cluster surface was passivated by treating Pt/Al_2O_3 formulations (black color) in mixtures of dry air (0.1-0.3 cm^3 g^{-1} s^{-1}, ultrapure, Minneapolis Oxygen) and He (3.3 cm^3 g^{-1} s^{-1}, ultrapure, Minneapolis oxygen) at 298-303 K for at least 1.5 h.

NH_4-MOR (Si/Al = 11.1, 0.5-10 g, CBV 21A, Zeolyst) was mixed with 1.5 L $NaNO_3$ solution ($3.9x10^{-3}$-$1.2x10^{-2}$ M, Sigma-Aldrich) at 353 K for at least 12 h to exchange protons with sodium cations and then filtered and washed in 5L deionized water to remove unexchanged Na^+. The washed sample was dried in ambient air at 363 K for at least 12 h and then treated in dry air (1.67 cm^3 s^{-1} at NTP conditions, ultrapure, Minneapolis Oxygen) at 773 K (0.0167 K s^{-1}) for 5 h.

Chemical titration using dimethyl ether (DME) over H-FER, H-MOR, and H-BEA materials was performed to determine the framework Al content. The theory, procedure, and result of DME titration are described and tabulated (shown in Table S.3.2.2, Supplementary info) in the supplemental information. Our measurements for the samples reported in this study resulted in a DME per Al ratio of 0.5±0.08 for all three zeolites, showing that the concentration of Brønsted acid sites is nearly identical to the concentration of Al in the three zeolites.

3.2.2 Steady-state catalytic reactions of n-hexane-hydrogen mixtures

Steady-state isomerization reactions of n-hexane were carried out in a tubular packed-bed quartz reactor (10 mm inner diameter) under atmospheric pressure and differential conditions (< 8% for hydroisomerization). Catalyst samples were supported on a coarse quartz frit inside the reactor, and the temperature was controlled using a furnace (National Electric Furnace FA120 type) connected to a Watlow Temperature Controller (96 series). Catalyst temperatures were measured using a K-type thermocouple touching the bottom of a well on the external surface of the quartz reactor. Prior to measurement of n-hexane isomerization rates, catalyst samples (0.005-0.05 g proton form zeolites physically mixed with Pt/Al_2O_3 to achieve 0.9-1.0 Pt/H^+ molar ratio) were treated in H_2 at 673K for 4h (0.0167 K s^{-1}). When catalyst samples were insufficient in quantity to cover the thermowell, these samples were diluted with acid-washed quartz particles (0.5-0.8 g, 160-630 μm, European Commission, washed by 1M HNO_3). Liquid n-hexane ($4.6x10^{-5}$ mol s^{-1}) was vaporized at 383 K into a gas flow which contained He (1.8 cm^3 s^{-1} at NTP condition, Minneapolis oxygen), H_2 (0.15-1.75 cm^3 s^{-1}, ultra-pure carrier grade, Airgas), and a mixture of Ar/CH_4 (0.0137-0.0297 cm^3 s^{-1} at NTP conditions; 75% Ar and 25% CH_4, Minneapolis oxygen) as internal standard. The effluent from the reactor was sent via heated transfer lines to a mass spectrometer (MKS Cirrus 200 Quadrupole mass spectrometer system) and a gas chromatograph (Agilent 6890N GC) equipped with a methyl-siloxane capillary column (HP-1, 50.0m x 320 μm x 0.52 μm) connected to a flame ionization detector and a packed column (SUPELCO HAYESEP R 80/100 mesh packed column, 12ft) connected to a thermal conductivity detector. Activation energies and pre-exponential factors were calculated from Arrhenius plots where the reaction rate constants were measured as a function of temperature (358-409 K).

3.3. Results and discussion

3.3.1 Mechanism and kinetics for n-hexane hydroisomerization over bifunctional catalysts

The mechanism for n-alkane hydroisomerization over bifunctional catalysts has been extensively studied in both experimental [18-20, 22, 25] and computational studies [30, 31, 81] to show that the mechanism involves (i) dehydrogenation of n-hexane (nC_6) to form n-hexene ($nC_6^=$) over platinum clusters (Step 1, Figure 3.3.1) , (ii) $nC_6^=$ adsorption on the zeolite acid site to form a surface-bound, linear alkoxide species (Step 2, Figure 3.3.1), (iii) isomerization of this linear alkoxide species into a branched alkoxide species (Step 3, Figure 3.3.1), (iv) desorption of the branched alkoxide to form a mono-branched alkene and concurrent regeneration of the zeolitic acid site (Step 4, Figure 3.3.1), and (v) hydrogenation of the branched alkene on platinum clusters to generate mono-branched hexane (Step 5, Figure 3.3.1).

The role of platinum in the bifunctional pathway of hydroisomerization was studied by Kondo et al. [25] using in situ infrared (IR) spectroscopy. The introduction of n-heptane and D_2 over platinum clusters supported on deuterated form of BEA zeolite (Pt/D-BEA) at 498 K resulted in the appearance of a broad band centered at 2170 cm^{-1} (C-D bond stretching) and the appearance of bands attributed to zeolitic OH groups (3600-3700 cm^{-1}) with the concurrent disappearance of bands attributed to zeolitic OD groups (2750 cm^{-1}), showing that there is H/D exchange between OD groups in Pt/D-BEA and the C-H bonds of n-heptane. No bands attributed to C-D bonds appeared in the infrared spectra using deuterated form of BEA (D-BEA without platinum) when n-heptane and D_2 were introduced as reactants under the same reaction conditions, suggesting that Pt promotes rapid H/D exchange on Pt/D-BEA. These observations support the hypothesis that Pt clusters catalyze the dehydrogenation of alkane reactants to form unsaturated alkenes which can undergo rapid H/D exchange with OD groups.

Demuth et al. [30] show using periodic DFT that for 2-pentene on ZSM-22, isomerization of an alkoxide species through an edge-protonated transition state has an activation energy of 110 kJ mol^{-1}; this energy barrier is higher than that required for chemisorption of the alkene reactant (52 kJ mol^{-1}). Their calculations also show that the activation energy required for isomerization of the surface bound alkoxide through an edge-protonated transition state is considerably lower than that calculated for the isomerization reaction to occur via an alkyl shift transition state (180 kJ mol^{-1}), consistent

with results presented by Boronat et al. [31]. Calculations done using cluster-based DFT or hybrid QM/MM methods show that the branched alkoxide species is less stable than the linear alkoxide species on 8T [82] and 46T [83] clusters of MFI and FAU [27], suggesting that the energy barrier for desorption of the branched alkoxide is lower than that for desorption of the linear alkoxide. Aronson et al. [84, 85] observed rapid H/D exchange between C-H bonds of 2-methyl-2-propanol and D_2O using infrared spectroscopy and H-ZSM-5 catalysts at only 298 K, indicating the rate of adsorption and desorption of the branched alkoxide intermediate formed upon dehydration of the alcohol is fast. Therefore, in our reaction studies, desorption of branched hexoxide species (step 4, Figure 3.3.1) is unlikely to be the kinetically-relevant step.

Equations 3.3.1 and 3.3.2 are the rate laws derived from the bifunctional hydroisomerization mechanism shown in Figure 3.3.1 with the assumption that the surface is mainly occupied by surface-bound linear alkoxide species and empty Brønsted acid sites. In these two equations, K_{dehy} is the equilibrium constant for dehydrogenation of n-hexane on platinum surfaces (Step1, Figure 3.3.1); $K_{prot,2}$ and $K_{prot,3}$ are the equilibrium constants for formation of surface-bound 2-hexoxide and 3-hexoxide species by adsorption of n-hexene on Brønsted acid sites (Step2, Figure 3.3.1); K_{prot} is the equilibrium constant for formation of surface-bound hexoxide species including 1-hexoxide, 2-hexoxide and 3-hexoxide, so $K_{prot} = K_{prot,1} + K_{prot,2} + K_{prot,3}$; k_{iso} is the rate constant for isomerization of surface-bound alkoxide species (Step 3, Figure 3.3.1); $[H^+]_0$ is the number of initially accessible Brønsted acid sites; $[nC_6]$ is the partial pressure of n-hexane and $[H_2]$ is the partial pressure of hydrogen.

$$\frac{r_{2MP}}{[H^+]_0} = \frac{k_{iso,2} K_{prot,2} K_{dehy} \frac{[nC_6]}{[H_2]}}{1 + K_{prot} K_{dehy} \frac{[nC_6]}{[H_2]}} \tag{3.3.1}$$

$$\frac{r_{3MP}}{[H^+]_0} = \frac{k_{iso,3} K_{prot,3} K_{dehy} \frac{[nC_6]}{[H_2]}}{1 + K_{prot} K_{dehy} \frac{[nC_6]}{[H_2]}} \tag{3.3.2}$$

Equations 3.3.1 and 3.3.2 can be written in a linear form as Equations 3.3.3 and 3.3.4, which accurately describe the kinetic effects of H_2/n-C_6 molar ratio on the inverse rate of 2-methylpentane (2-MP) and 3-methylpentane (3-MP) formation over FER, MOR, and BEA as shown in Figures 3.3.2-3.3.4 (b). The values of the apparent rate constant, $k_{app,2}$ ($k_{app,2} \equiv k_{iso,2}K_{prot,2}K_{dehy}$), and K_{prot} can be obtained from the values of the slope and the intercept, respectively. Using the values of $k_{app,2}$, K_{prot} obtained from Figures 3.3.2-3.3.4 (b) along with the value of K_{dehy}, which is calculated from thermochemical data [20], we can accurately predict the rates of n-hexane isomerization as shown in Figures 3.3.2-3.3.4 (a). The isomerization rate over proton-form FER, MOR, and BEA can be described by the same rate equations (Equations 3.3.1 and 3.3.2), suggesting that the same mechanism is operative on these materials under these reaction conditions. The isomerization rate is a function of n-C_6/H_2 molar ratio as shown in Figures 3.3.2-3.3.4, consistent with the proposed bifunctional mechanism depicted in Figures 3.3.1 where the concentration of $nC_6^=$ is in equilibrium with the n-C_6/H_2 molar ratio.

$$\frac{[H^+]_0}{r_{2MP}} = \frac{1}{k_{iso,2}K_{prot,2}K_{dehy}}\frac{[H_2]}{[nC_6]} + \frac{K_{prot}}{k_{iso,2}K_{prot,2}} \qquad (3.3.3)$$

$$\frac{[H^+]_0}{r_{3MP}} = \frac{1}{k_{iso,3}K_{prot,3}K_{dehy}}\frac{[H_2]}{[nC_6]} + \frac{K_{prot}}{k_{iso,3}K_{prot,3}} \qquad (3.3.4)$$

To eliminate the possibility of diffusion effects playing a significant role in the measured catalytic rates or selectivity on the zeolites studied, we calculated the effectiveness factor (η) according to the procedure reported by Haag et al. [13]. The calculated η is equal to 1 for both FER and MOR using the diffusion coefficient of n-hexane in FER (3.5×10^{-8}) and MOR (2.8×10^{-8}) calculated by Schuring et al. [86] using canonical (NVT) molecular dynamics simulations. Experimentally, de Gauw et al. [20] also concluded that no diffusion limitations exist for 12-MR BEA and MOR zeolites or for 10-MR MFI and TON materials for n-hexane hydroisomerization because no effect on turnover frequency for MFI and TON and no effects on activation energy for BEA and MOR were noted with varying zeolite crystal size (0.6-3.5 μm for MFI, 1-4 μm for TON, 0.1-1 μm for BEA and 0.6-3.5 μm for MOR).

3.3.2 Assessment of the kinetics and rate of n-hexene isomerization in 8-MR side pockets and 12-MR channels within MOR using Na^+ exchanged samples

van de Runstraat et al. [19] suggested that two-thirds of the acid sites in MOR framework materials are inaccessible to n-hexane based on the observation that n-hexane adsorption capacity (0.07 ml g^{-1}) on their MOR-type material was only one-third of its BET volume (0.2 ml g^{-1}), and that the rate of n-hexane hydroisomerization on MOR per proton (9.7 mol mol^{-1} h^{-1}) was also ~ 1/3 of the rate on BEA (27.9 mol mol^{-1} h^{-1}) at 513 K. MOR consists of 12-MR main channels (denoted as MOR(12MR)) with intersecting 8-MR side pockets (denoted as MOR(8MR)) which may be inaccessible for n-hexane reactants due to the small pore opening (0.34 x 0.48 nm) [87]. Here, we used Na^+ to selectively replace the protons in 8-MR pockets of MOR to explore the accessibility of OH groups in 8-MR pockets for n-hexane reactions.

The asymmetric hydroxyl band corresponding to zeolitic OH groups (~3607cm^{-1}) in the infrared (IR) spectrum of MOR can be deconvoluted to infer the existence of two distinct bands, one corresponding to OH groups in 8-MR pockets (3590 cm^{-1}) and the other corresponding to the OH groups in 12-MR channels (3610 cm^{-1}) [75, 88]. Infrared spectra (shown in Figure S.3.1.1 and reported in Table S.3.1.1 in the Supplementary information) in the OH stretching region for H-MOR as Na^+ replaced some of the H^+ species show that the OH band in MOR became more symmetric with increasing Na^+ content because of a preferential weakening of the band corresponding to hydroxyl groups in 8-MR pockets implying that Na^+ selectively replaced H^+ in 8-MR pockets of MOR. Similar observations haves been reported by Veefkind et al. [89], Bhan et al. [75] and Maache et al. [90]. The number of H^+ in the 8-MR side pockets decreased ~50% when only ~20% of the total H^+ species were replaced in MOR. In contrast, the fraction of H^+ sites in 12-MR channels was largely unchanged by Na^+ when ~45% of the total H^+ sites were replaced in MOR.

The kinetics of n-hexane isomerization were measured on a series of Na^+ exchanged samples to show that k_{app} values for OH groups in 12-MR channels ($9.3x10^{-4}$-$1.0x10^{-3}$ molecules $(H^+\ s)^{-1}$) are nearly invariant with the concentration of OH groups ($H_{19}Na_{81}$MOR, $H_{32}Na_{68}$MOR and $H_{55}Na_{45}$MOR) as shown in Figure 3.3.5. The

measured k_{app} of n-hexane hydroisomerization over samples containing OH groups in both 8-MR and 12-MR channels ($H_{81}Na_{19}$MOR and $H_{100}Na_{0}$MOR) increased with the number of H^+ in the 8-MR pockets (Figure 3.3.5), indicating that Brønsted acid sites circumscribed in the constrained 8-MR side pockets of MOR catalyze n-hexane isomerization with higher rates than acid sites circumscribed by larger 12-MR channels.

Eder et al. [54] showed that OH groups in 8-MR side pockets of MOR are not accessible to n-hexane based on the observation that the infrared band corresponding to OH groups in 12-MR channels of MOR decreased upon introduction of n-hexane but the infrared band attributed to OH groups in 8-MR side pockets of MOR was nearly unperturbed even under 10 mbar of n-hexane at 303 K. In contrast, our results indicate that the OH groups in 8-MR pockets are accessible to n-hexene under hydroisomerization reaction conditions, suggesting that n-hexene is isomerized by the acidic OH groups contained within in 8-MR side pockets at high temperature (> 473 K). Carpenter et al. [91] studied the constraint index (CI) of proton form MOR and sodium exchanged MOR where the protons in 8-MR side pockets were selectively replaced by Na^+. Even though there was deactivation in both proton form MOR and sodium exchanged MOR, they found that the CI value (~1.5) of sodium exchange MOR was constant with time on stream (TOS), while the CI value of proton form MOR increased from 1.5 to 6 with TOS at 603 K. These findings suggest that deactivation in 12-MR channels is faster than in 8-MR pockets, and also show that n-hexane can enter the 8-MR side pockets of MOR at high temperatures relevant for hydrocarbon reactions on MOR. Low temperature adsorption studies suggest that n-hexane cannot access OH groups in 8-MR pockets of MOR, however, reaction studies done at higher temperatures lead us to conclude that at high temperatures C_6 molecules can access the OH groups in the 8-MR side pockets of MOR.

The measured rate of isomerization per H^+ over the $H_{32}Na_{68}$MOR sample is the rate per H^+ in the 12-MR channels of MOR, because only 12-MR channels have residual H^+ in this sample. The rate in the 8-MR pockets of MOR can be extracted by subtracting the rate in 12-MR channels of MOR from the rate in H-MOR. The measured rate of n-hexane isomerization in MOR(12MR) and the calculated rate in MOR(8MR) still follow

Equations 3.3.1 and 3.3.2 as shown by the reciprocal rate plots in Figure 3.3.6 and 3.3.7, respectively, indicating that the mechanism for n-hexane isomerization in MOR(8MR) and in MOR(12MR) can be accurately described by the bifunctional mechanism shown in Figure 3.3.1. The k_{app} for olefin isomerization normalized per proton in the 8-MR pockets is 5 times larger than that in 12-MR channels of MOR as shown by the data reported in Table 3.3.1. These data constitute another example showing that catalytic turnover rates vary depending on the location of OH groups within a particular zeolite framework. Prior reports have discussed the specificity of OH groups in 8-MOR side pockets of H-MOR for CO insertion in surface methyl groups and monomolecular dehydrogenation of saturated hydrocarbons [23, 75, 76]. The detailed discussion of the essential role of local zeolite environment in enthalpic and entropic stabilization and in determining selectivity of isomerization reactions is presented in section 3.3.4.

3.3.3 Effects of zeolite structure on n-hexane hydroisomerization

A comparison of kinetic and thermodynamic parameters assessed from linearized plots based on Equations 3.3.3 and 3.3.4 as shown in Figures 3.3.2-3.3.4 for FER, MOR, and BEA is reported in Table 3.3.1. Rate constants for n-C_6 isomerization at 473 K increase in the order FER < MOR(12MR) < MOR(8MR) < BEA, consistent with reports in the literature where BEA has been reported to have a rate higher than MOR, MFI, and TON [19, 92]. Regressed rate constants on acid sites in FER, BEA, MOR (12-MR) and MOR (8-MR) are shown as a function of temperature in Figure 3.3.8; these data were used to estimate the apparent activation energy (E_{app}) and entropy (ΔS_{app}) for n-hexane hydroisomerization. The values of E_{app} and ΔS_{app} compiled in Table 3.3.1 represent the difference in energy and entropy between n-hexane in the gas phase and the transition state as shown in Figure 3.3.9.

The apparent activation energy (E_{app}) of 2-MP formation decreases with decreasing the pore size as shown in Table 3.3.1. This trend may be caused by a decrease in the heat of physisorption (ΔH_{ads}) of linear hydrocarbons with increasing pore size [54, 72, 93-96], or caused by greater stabilization of electropositive transition states by negatively charged framework oxygen atoms in smaller channels as proposed by Rozanska et al. [97-99].

These authors studied the isomerization of toluene and xylene [99], cracking of thiophenic derivatives [98], and propylation of benzene [97] using periodic DFT methods and noted that cationic transition states are more stable when the electropositive hydrocarbon fragment is close to framework oxygen atoms and is surrounded by more framework oxygen atoms because of the partial negative charge on these oxygen atoms.

The measured activation energy, E_{app}, can be expressed as Equation 3.3.5 according to the energy profile for n-hexane hydroisomerization shown in Figure 3.3.9 where ΔH_{dehy} is the enthalpy of n-hexane dehydrogenation (118 kJ mol^{-1}) [20]; ΔH_{ads} is the heat of physisorption of n-hexene; ΔH_{alk} is the enthalpy of alkoxide formation by adsorption of n-hexene; and E_{int} is the intrinsic activation energy of alkoxide isomerization. The heat of physisorption of n-hexene can be estimated using the heat of n-hexane adsorption measured by Eder et al. [54, 72] and Denayer et al. [95] with the consideration that physisorption energies arise primarily due to confinement and are largely independent of chemical functionality. If we subtract the contribution of ΔH_{dehy} and ΔH_{ads} from the E_{app}, the remaining values ($\Delta H_{alk} + E_{int}$) do not increase with decreasing pore size as shown in Table 3.3.2. Since E_{int} is likely to decrease with decreasing pore size due to electrostatic stabilization of the cationic transition state [97], this result may indicate that the stability of alkoxide intermediate is not only related to the diameter of a pore but also to the local environment of Brønsted acid site. This observation has been noted previously in computational studies by Boronat et al. [100] based on the remarkable changes in the energy for alkoxide formation from physisorbed 1-butene (from -14.5 kcal on 3T cluster to 7.1 kcal mol^{-1} on 11T cluster for 2-butoxide formation) over four different clusters (3-26 T atoms) cut from zeolite theta-1 using DFT (B3PW91) and Hartree-Fock (HF) methods. In another computational study, Rozanska et al [101] studied the adsorption of propylene on zeolite CHA using periodic DFT (GGA) and their results show that the energy for alkoxide formation from physisorbed propylene changes from +23 kJ mol^{-1} to -27 kJ mol^{-1} upon increasing the flexibility of zeolite framework. These findings in the aforementioned computational studies also suggest that local geometry of zeolitic acid sites is an important parameter that determines the stability and reactivity of adsorbed hydrocarbon alkoxide species.

$$E_{app} = \Delta H_{dehy} + \Delta H_{ads} + \Delta H_{alk} + E_{int} \quad (3.3.5)$$

The rate of hydroisomerization on H-BEA catalysts is higher than that on FER and MOR materials due to the lower apparent activation energy in BEA compared to MOR and due to the higher activation entropy in BEA compared to FER. The higher entropy of activation in BEA than in FER is intuitively related to the large pore size of BEA and is consistent with the results reported by de Gauw et al. [20] for n-hexane hydroisomerization where they compare apparent rate constants for different zeolites and note that BEA has a larger pre-exponential factor than 10-MR zeolites ZSM-5 and ZSM-22.

Even though FER has the lowest E_{app}, it has the lowest reaction rate among the studied zeolites due to the larger entropy loss in FER compared to other zeolites studied as shown by the data reported in Table 3.3.1. The lowest ΔS_{app} and lowest E_{app} in FER are consistent with FER having smaller channels compared to MOR and BEA. FER has the highest $k_{app,2MP}/k_{app,3MP}$ ratio (2.1) among the zeolites studied, because FER has the largest difference in E_{app} between 3-MP formation and 2-MP formation (17 kJ mol^{-1} difference), in line with observations by van de Runstraat et al. [19] showing that 10-MR zeolites have a higher 2-MP/3-MP ratio (2.7-2.9 for TON and 3.4 for MFI) than 12-MR zeolites (1.5 for MOR and 1.6 for BEA), indicating that small pores put constraints on the formation of intermediates for 3-MP. The critical diameter for 2-MP and 3-MP is 0.54 nm [102, 103] and the heats of adsorption of 2-MP and 3-MP are the same on 10-MR zeolites (62 kJ mol^{-1} for TON and 66kJ mol^{-1} for MFI [95]), suggesting that the high $k_{app,2MP}/k_{app,3MP}$ observed in FER is not caused by any detectable differences in size or adsorption enthalpy of 2-MP and 3-MP.

The data reported in Table 3.3.1 show that ΔS_{app}, E_{app}, $k_{app,2MP}/k_{app,3MP}$ of the MOR(8MR) are closer to values in large 12-MR channels of MOR and BEA instead of medium pore FER materials. The possible reasons for the 8-MR pockets in MOR behaving like 12-MR channels are discussed in section 3.3.4.

3.3.4 Effects of partial confinement in 8-MR side pockets of MOR on n-hexane isomerization reactions

The size of 8-MR side pockets of MOR (0.34 x 0.48 nm) is smaller than the diameter of 12-MR channels of MOR (0.70 x 0.65nm), whereas the values of ΔS_{app} for 2-MP and 3-MP formation in MOR(8MR) are similar to those in larger 12-MR channels of MOR and BEA as shown in Table 3.3.1. Webster et al. [104] calculated the dimensions of different molecules along x, y and z axis using semi-empirical quantum chemistry methods and the length of n-hexane (1.03 nm) they calculated is consistent with the length calculated by Jimenez-Cruz (1.06 nm) using DFT methods [103]. The depth of 8-MR pockets (~0.37nm) [23] is much shorter than the length of n-hexane [104, 105]. Therefore, the similarity in ΔS_{app} measured for C_6 reactions in MOR(8MR), 12-MR channels of MOR, and BEA which is 46 J mol^{-1} K^{-1} higher than that measured in FER as shown in Table 3.3.1 may be caused by partial confinement effects first postulated by Gounder and Iglesia [23]. These authors showed that monomolecular alkane dehydrogenation was preferentially catalyzed by OH groups in 8-MR channels of MOR and that this specificity reflected transition states that were only partially confined within small 8-MR side pockets. This partial confinement resulted in entropic gains that compensated for enthalpic penalties incurred by incomplete containment within 8-MR pores and resulted in a lower overall free energy for monomolecular alkane cracking and dehydrogenation reactions. Carpenter et al. [91] suggested that the deactivation rate in 12-MR channels and 8-MR side pockets may be different based on the observation that the constraint index (CI) of proton form MOR increased from 1.5 to 6 with time-on-stream at 603 K. We note that the CI value is constant (CI = 6) after 5.2 h on proton form MOR, this value is much lower than the CI value in 8-MR zeolites (CHA>100 and ERI=38)[106], suggesting that OH groups in 8-MR pockets of MOR behave differently that OH groups in 8-MR channels of CHA and ERI for reactions of n-hexane and 3-methypentane. The similar entropy loss for n-hexane hydroisomerization reactions for Brønsted acid catalytic centers circumscribed in 8-MR pockets and 12-MR channels of MOR, the length of the n-hexane molecule compared to the size of the 8-MR pocket in MOR, and the anomalous CI value of 8-MR channels in MOR leads us to hypothesize that the n-hexene molecule is partially confined in the 8-MR side pockets.

The transition state of hexene isomerization has a positively charged three-carbon ring (Figure 3.3.9) which is expected to have a larger kinetic diameter than propane (0.43 nm) [23, 104] based on their structures. Because it is difficult for the three-carbon ring (> 0.43nm) to be fully contained in the 8-MR pockets of MOR (0.34 x 0.48 nm), the three-carbon ring may be located near the pore mouth of the 8-MR pockets or in the 12-MR channels as shown in Figure 3.3.10. The calculated 2-MP/3-MP selectivity in 8-MR pockets of MOR is similar to that in 12-MR channels of MOR and BEA but lower than that in FER as shown in Table 3.3.1, supporting our hypothesis that the 3-carbon ring is not completely contained within the 8-MR pockets of MOR.

The five fold larger rate in 8-MR side pockets compared to that in the 12-MR channels of MOR is a result of the lower activation energy in the 8-MR pockets. Rozanska et al. [99] studied isomerization of toluene and xylene and found that the CH_3^+ ion in the transition state of toluene isomerization is near the pore mouth of 8-MR side pockets in MOR such that it can be surrounded by more framework oxygen atoms even though the Brønsted acid site is located on the opposite side of these pore mouth oxygen atoms. We postulate that the cationic transition state of n-hexane isomerization may be located near the pore mouth of the 8-MR pockets and thereby be stabilized by framework oxygen atoms around the pore mouth of the 8-MR pockets which would result in the lower E_{app} in the 8-MR pockets compared to the 12-MR channels of MOR (Table 3.3.1). Pore mouth catalysis was first hypothesized by Martens et al. [107] to explain the high selectivity (~60%) for 2-methylnonane (2-MN) in decane hydroisomerization (2-MN/3-MN = 2.4) on 10-MR zeolite TON-type materials. They hypothesized that the reactant molecule is selectively adsorbed on the entrances of channels so that only part of the reactant is inside the channels but the rest of the molecule is on the "external surface" of the zeolite crystal [11]. Our hypothesis is that n-hexene isomerization occurs at the pore mouth of 8-MR pockets in MOR and is an example of "intracrystalline" pore mouth catalysis where the reaction occurs at the pore mouth of one channel which intersects with a larger channel.

Clark et al. [87] showed that the adsorption of argon, methane, CF_4, and SF_6 in the 8-MR pockets of MOR is 5-8 kJ mol^{-1} stronger than in 12-MR channels of MOR using

Grand Canonical Monte Carlo (GCMC) simulations. Therefore, another possible reason for the lower E_{app} in MOR(8MR) compared to that in MOR(12MR) is the larger heat of adsorption in smaller 8-MR pockets than in 12-MR channels mediated by confinement effects. The effective diameter of a pore is the average of the distances of the two axes of an elliptical pore after adding the oxygen atom diameter (0.27 nm) [23, 108] and Savitz et al. [108] predicted the heat of adsorption of C_2-C_3 accurately using an effective pore diameter in a Lennard-Jones 12-6 potential. Because the effective pore radius of the small 8-MR pockets of MOR (0.34 nm) is close to the effective radii of the 10-MR channels (0.37 nm) and 8-MR channels (0.34 nm) in FER [23], the heat of alkane adsorption in FER can be used to approximate the heat of adsorption of hydrocarbons in the 8-MR pockets of MOR [23]. The depth of the 8-MR pockets (0.37nm) is about 1/3 of the length of n-hexane (1.06 nm), so approximately two carbons can be accommodated in the 8-MR pocket. Therefore, the difference in the heat of n-hexane adsorption in 12-MR channels of MOR and n-hexane partially confined in 8-MR pockets can be estimated using the heats of ethane adsorption in the 12-MR channels of MOR and in FER. Eder et al. [54, 72] measured the heat of adsorption of propane in MOR (-41 kJ mol^{-1}) and FER (-49 kJ mol^{-1}) and found that the heat of adsorption increases -9 kJ mol^{-1} and -10 kJ mol^{-1} per CH_2 group for C_3 to C_6 alkanes on MOR and FER, respectively. From these values, we estimate the heat of ethane adsorption in MOR (-32 kJ mol^{-1}) and FER (-39 kJ mol^{-1}). The difference between these two heats of adsorption (-7 kJ mol^{-1}) is similar to the difference in E_{app} for n-hexane isomerization between MOR(12MR) and MOR(8MR). Therefore, the lower E_{app} in MOR(8MR) compared to the E_{app} in MOR(12MR) may be due to the larger heat of adsorption caused by the partial confinement of n-hexane in 8-MR side pockets.

The enhancement in the rate of n-hexane hydroisomerization in the 8-MR pockets of MOR is in line with recent reports demonstrating selective CO insertion into surface-bound methoxide species [6, 7, 10], higher rates for monomolecular cracking and dehydrogenation of propane and butane [23, 79], and selective unimolecular ethanol dehydration [80]. Collectively, these reports and our work for n-hexane hydroisomerization described above show that the location of zeolitic OH groups

strongly influences reaction rates and selectivity. The selectivity for 2-MP/3-MP and the entropy of reaction for 2-MP and 3-MP formation in 8-MR side pockets of MOR is similar to that in 12-MR channels of MOR and BEA instead of medium pore FER, showing that pore size cannot be used to accurately predict the occurrence or exclusion of a particular reaction within zeolitic solids. Our findings regarding intracrystalline pore mouth catalysis provide another conceptual consideration for rigorous and quantitative understanding of local environment effects of zeolite channel size and connectivity on the rate and selectivity of acid catalyzed reactions.

3.4 Conclusions

n-C_6H_{14} hydroisomerization reactions showed that measured rates of 2-methylpentane (2MP) and 3-methylpentane (3MP) formation were linearly proportional to the molar ratio of H_2 to n-C_6H_{14} over FER, MOR, and BEA zeolites, consistent with a bifunctional mechanism involving the facile dehydrogenation of n-hexane on the metal catalyst and a kinetically-relevant step involving isomerization of n-hexene on zeolitic acidic sites. The rate of n-hexane hydroisomerization increases in the order FER < MOR (12MR) < MOR(8MR) < BEA. The measured temperature dependence of hydroisomerization rates showed that the low isomerization rates in FER are primarily a result of entropy loss.

Na^+ selectively replaced protons within 8-MR pockets of MOR and led to a disproportionate decrease in hexane isomerization turnover rates per H^+, showing that the rate of n-hexane hydroisomerization in 8-MR pockets is five times larger than the rate in 12-MR channels of MOR. The similar entropy loss in small 8-MR channels compared to larger 12-MR channel in MOR is consistent with a partial confinement hypothesis, where adsorbates and activated complexes are only partially confined in the small 8-MR side pockets of MOR. The bulky 3-carbon ring of the cationic transition state may be located near the pore mouth, resulting in similar selectivity of 2MP to 3MP but lower apparent activation energy compared to 12-MR channels of MOR due to electrostatic stabilization by negatively charged framework oxygen atoms around the pore mouth of the 8-MR pockets or due to the partial adsorption in 8-MR pockets.

A positively charged transition state, reactant or intermediate located at the pore mouth of small zeolitic channels can optimize its free energy by partially protruding into the large channels in order to gain entropy and release energy through stronger dispersion forces or electronic stabilization as a result of partial confinement by the pore mouth of small channels. The concepts of intracrystalline pore mouth catalysis provide another fundamental consideration for zeolite catalyzed reactions when the dimension of a reactant or intermediates are larger than the dimension of a small channel intersecting with a larger channel.

Acknowledgement

The authors acknowledge the financial support from ARPA-E program (ARPA-E, Award number # DE-AR0000007). H. C. was partially supported by funds from the Petroleum Institute of Abu Dhabi through the ADMIRE (Abu Dhabi-Minnesota Institute for Research Excellence) partnership. Sasol North America Inc. donated Al_2O_3 samples. We acknowledge Dr. Do-Young Hong for the preparation and characterization of Na^+-MOR samples and also thank Mingwei Tian, Henry Kim, and Yasser Al Wahedi for assistance with the synthesis of Pt/Al_2O_3.

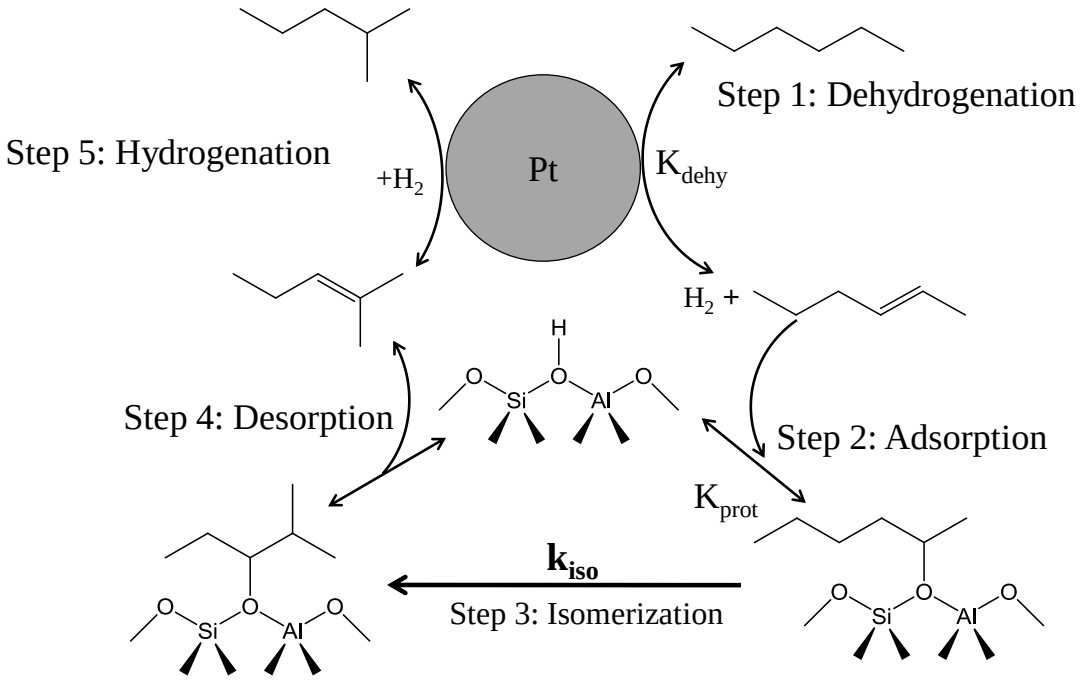

Figure 3.3.1. Bifunctional mechanism for n-hexane hydroisomerization.

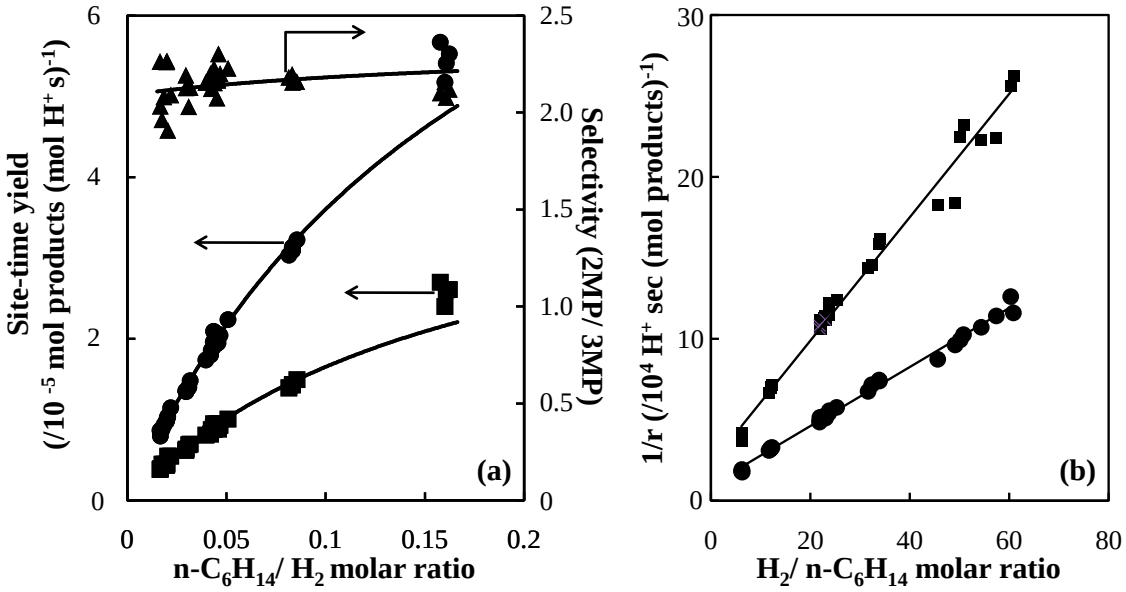

Figure 3.3.2. (a) Measured site-time yield of 2-methylpentane (●), 3-methylpentane (■) and ratio of 2-methylpentane to 3-methylpentane rates as a function of n-C_6/H_2 molar ratio (▲) over FER at 473 K. The solid lines represent predictions from Equations 3.3.1 and 3.3.2. (b) Reciprocal rates of 2-methylpentane (●) and 3-methylpentane (■) as a function of H_2/n-C_6 molar ratio over FER at 473 K.

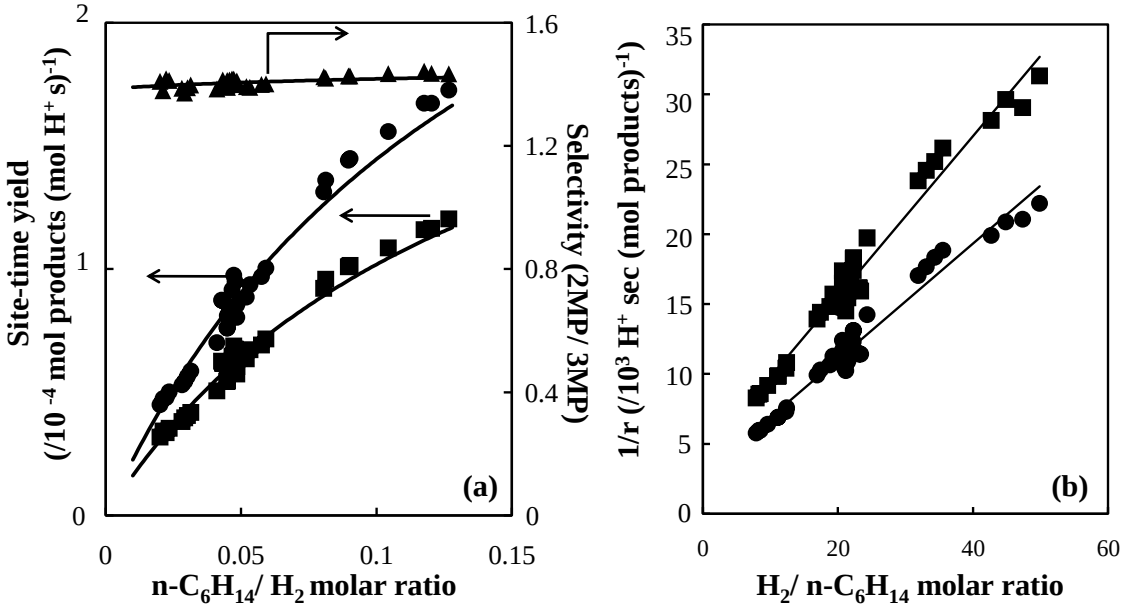

Figure 3.3.3. (a) Measured site-time yield of 2-methylpentane (●), 3-methylpentane (■) and ratio of 2-methylpentane to 3-methylpentane rates as a function of n-C_6/H_2 molar ratio (▲) over MOR at 473 K. The solid lines represent predictions from Equations 3.3.1 and 3.3.2. (b) Reciprocal rates of 2-methylpentane (●) and 3-methylpentane (■) as a function of H_2/n-C_6 molar ratio over MOR at 473 K.

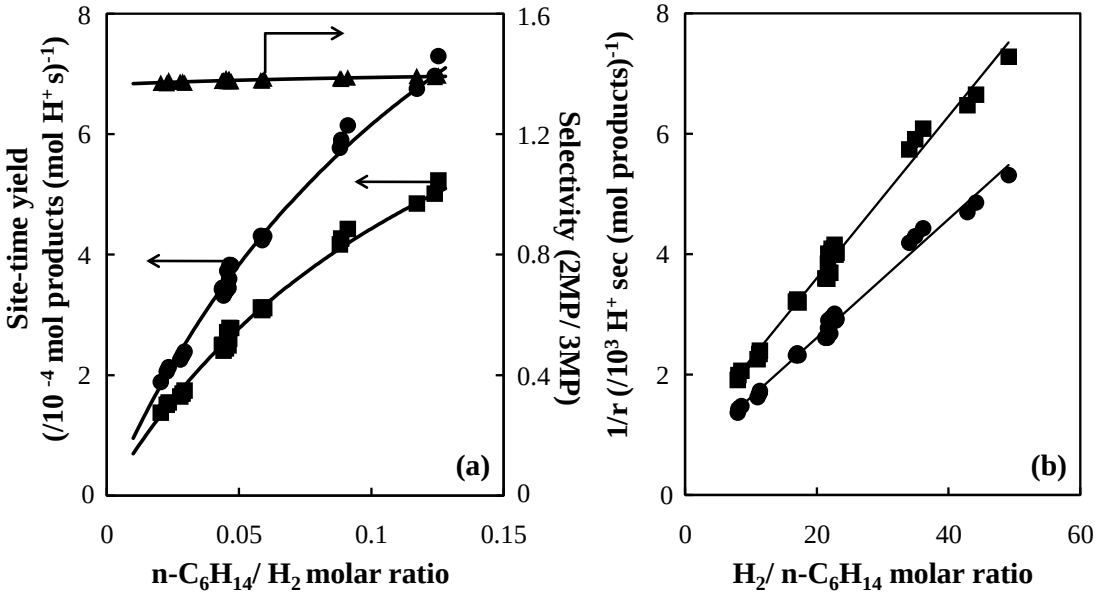

Figure 3.3.4. (a) Measured site-time yield of 2-methylpentane (●), 3-methylpentane (■) and ratio of 2-methylpentane to 3-methylpentane rates as a function of n-C_6/H_2 molar ratio (▲) over BEA at 473 K. The solid lines represent predictions from Equations 3.3.1 and 3.3.2. (b) Reciprocal rates of 2-methylpentane (●) and 3-methylpentane (■) as a function of H_2/n-C_6 molar ratio over BEA at 473 K.

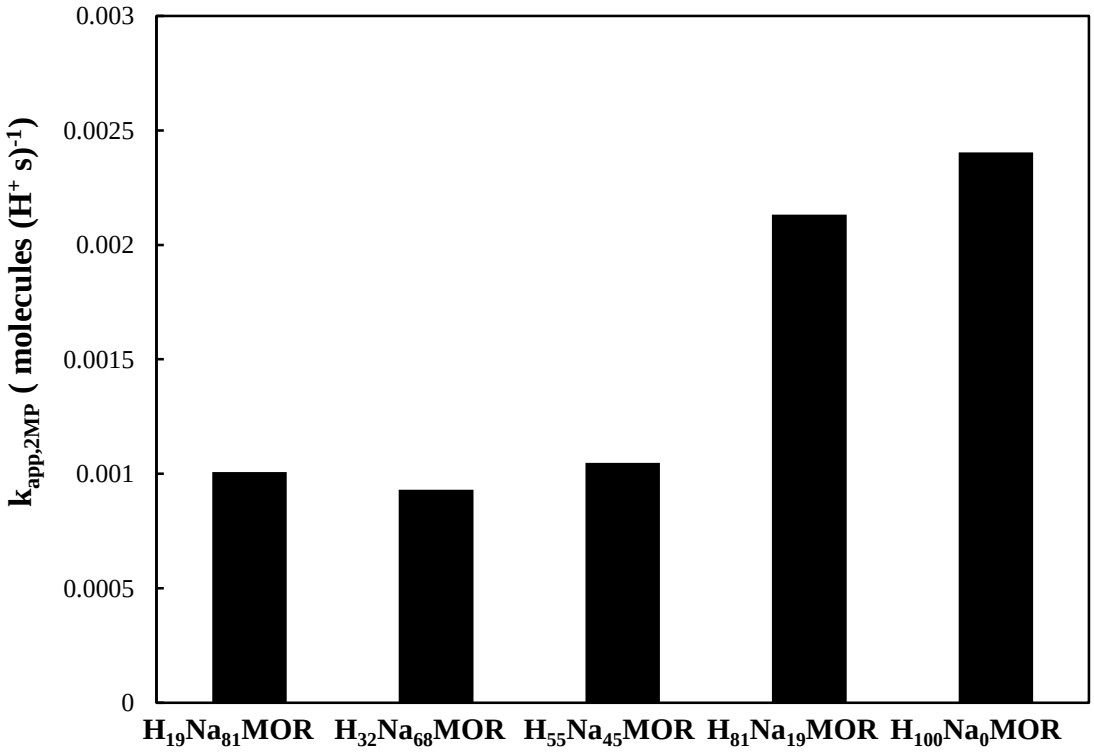

Figure 3.3.5. Apparent rate constants of 2-methylpentane formation ($k_{app,2MP}$) over different sodium exchanged MOR formulations at 473 K and n-C_6/H_2 ratio = 0.02-0.14; H_xNa_{100-x} represents the fraction of OH groups in Na-exchanged MOR samples.

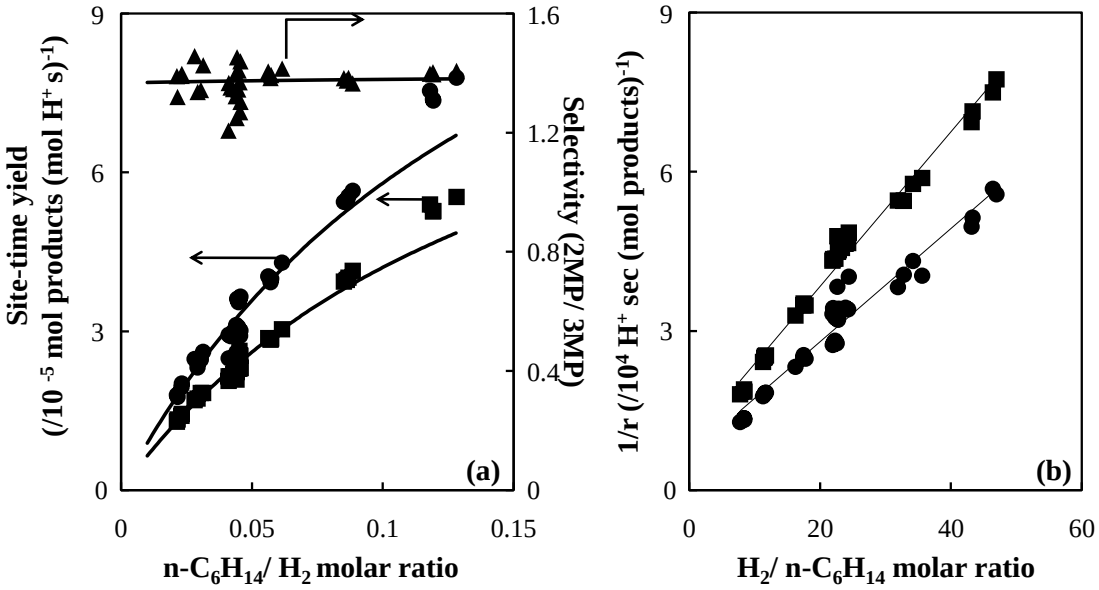

Figure 3.3.6. (a) Measured site-time yield of 2-methylpentane (●), 3-methylpentane (■) and ratio of 2-methylpentane to 3-methylpentane rates as a function of n-C_6/H_2 molar ratio (▲) over $H_{32}Na_{68}$MOR at 473 K. The solid lines represent predictions from Equations 3.3.1 and 3.3.2. (b) Reciprocal rates of 2-methylpentane (●) and 3-methylpentane (■) as a function of H_2/n-C_6 molar ratio over $H_{32}Na_{68}$MOR at 473 K.

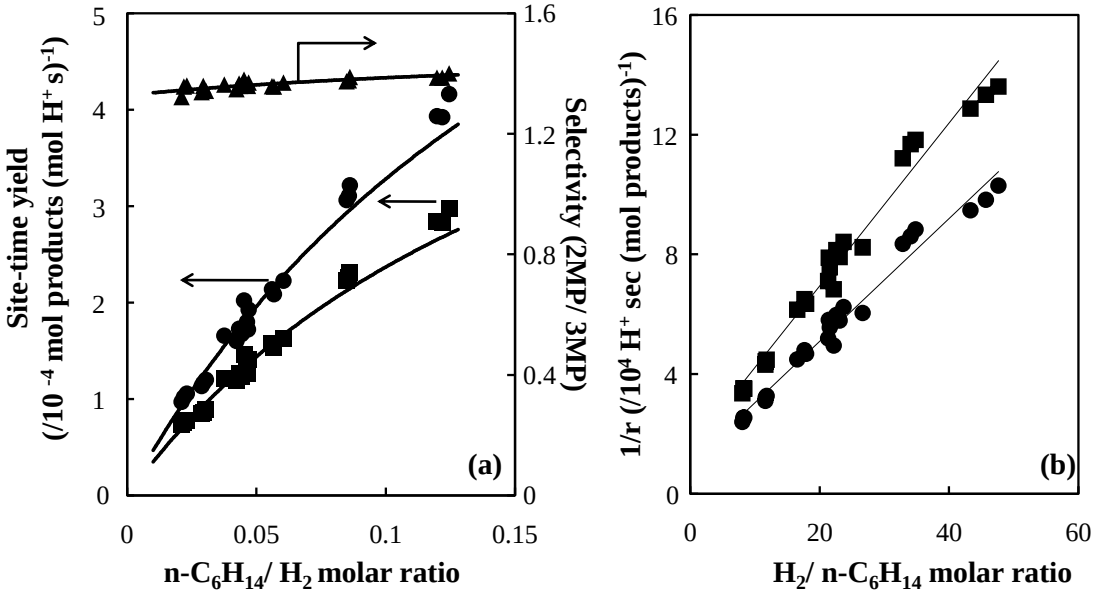

Figure 3.3.7. (a) Calculated site-time yield of 2-methylpentane (●), 3-methylpentane (■) and ratio of 2-methylpentane to 3-methylpentane rates as a function of n-C_6/H_2 molar ratio (▲) in the 8-MR side pockets within MOR materials at 473 K. The solid lines represent predictions from Equations 3.3.1 and 3.3.2. (b) Reciprocal rates of 2-methylpentane (●) and 3-methylpentane (■) as a function of H_2/n-C_6 molar ratio in the 8-MR side pockets within MOR materials at 473 K.

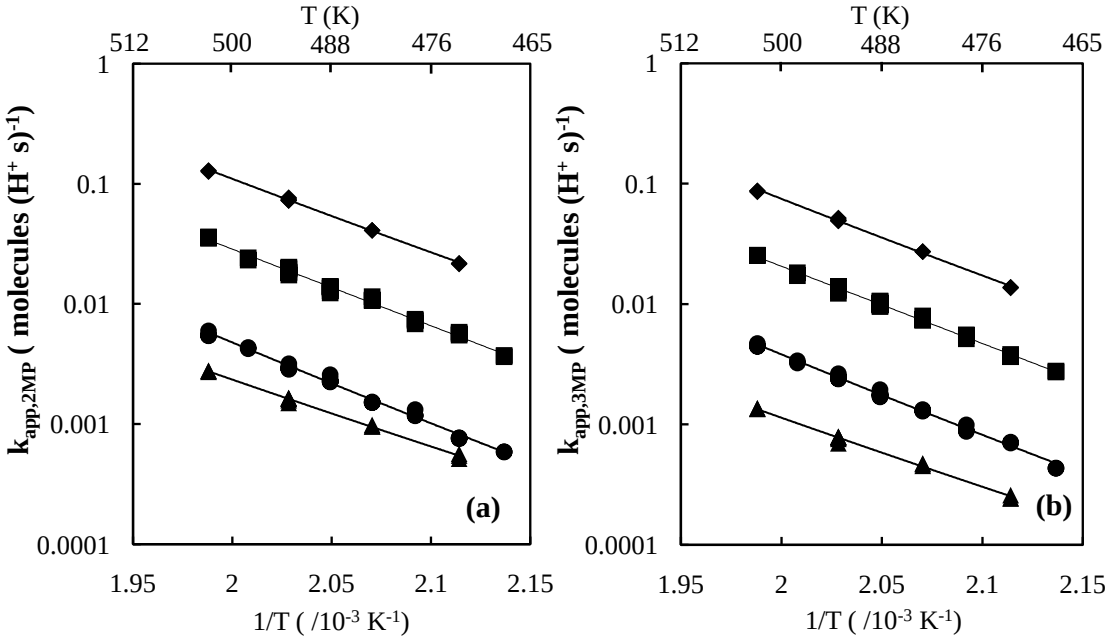

Figure 3.3.8. Measured apparent rate constants of (a) 2-methylpentane and (b) 3-methylpentane formation over BEA(◆), 8-MR pockets in MOR (■), 12-MR channels in MOR (●) and FER (▲) at n-C_6/H_2 ratio in the range 0.01-0.02.

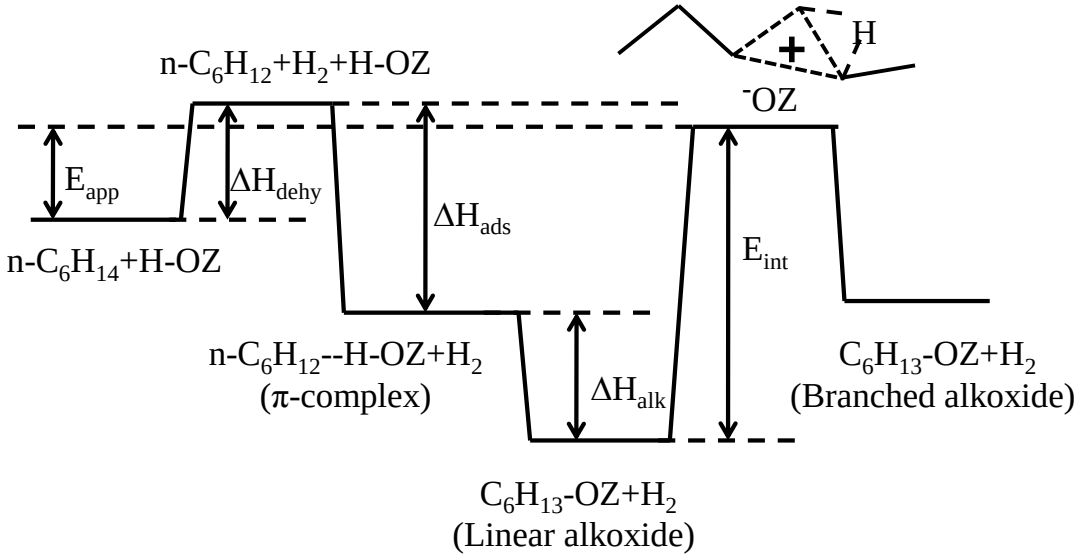

Figure 3.3.9. Energy diagram for n-hexane hydroisomerization.

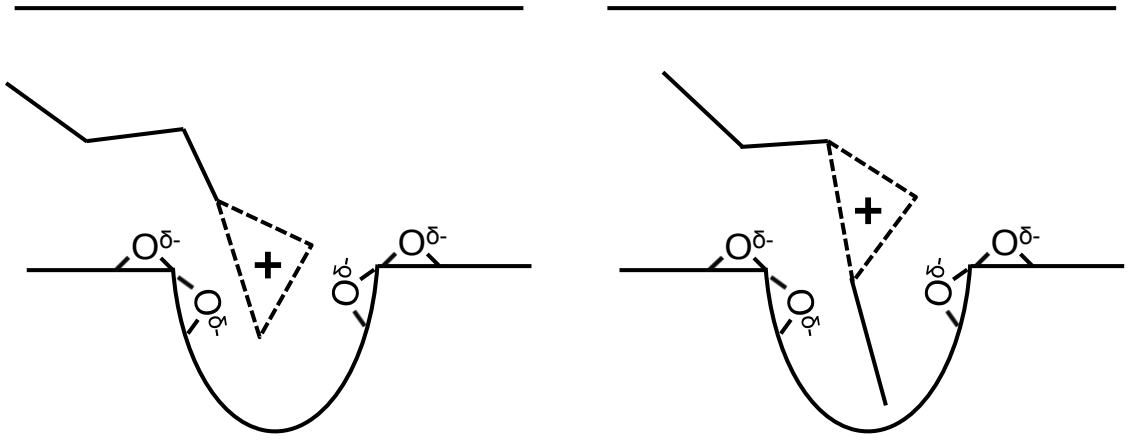

Figure 3.3.10. The postulated cyclopropyl transition state for n-hexene isomerization in the 8-MR channels of MOR.

Table 3.3.1. Rate constant of 2-methylpentane formation ($k_{app,2MP}$); ratio of rate constants for 2-methylpentane and 3-methylpentane formation ($k_{app,2MP}/k_{app,3MP}$) and apparent activation energy (E_{app}) and apparent entropy (ΔS_{app}) over proton form zeolite formulations.

Zeolite	$k_{app,2MP}$ at 473 K (molecules $(H^+ s)^{-1}$)	$k_{app,2MP}$ /$k_{app,3MP}$ at 473 K	2-Methylpentane		3-Methylpentane	
			E_{app} (kJ mol^{-1})	ΔS_{app} (J mol^{-1} K^{-1})	E_{app} (kJ mol^{-1})	ΔS_{app} (J mol^{-1} K^{-1})
FER	$5.4x10^{-4}$	2.09	106.5±3.6	-86.4±7.4	123.2±4.6	-86.4±9.3
12MR-MOR	$9.3x10^{-4}$	1.50	128.0±4.7	-37.4±9.7	127.2±3.5	-40.9±7.3
8MR-MOR	$4.9x10^{-3}$	1.55	121.9±4.7	-34.7±9.8	123.1±3.2	-35.0±6.6
BEA	$1.0x10^{-2}$	1.35	117.1±2.1	-33.1±4.3	121.7±3.0	-27.1±6.1

Table 3.3.2. Heat of adsorption of n-hexane (ΔH_{ads}), estimated energy difference between transition state and physisorbed hexene ($E_{int}+\Delta H_{alk}$) over proton form zeolite formulations.

Zeolite	ΔH_{ads} (kJ mol^{-1})	2-Methylpentane	3-Methylpentane
		$E_{int} + \Delta H_{alk}$ (kJ mol^{-1})	$E_{int} + \Delta H_{alk}$ (kJ mol^{-1})
FER	-79[72]	67	84
12MR-MOR	-69[54]	79	78
8MR-MOR	-92[a]	96	97
BEA	-63[93]	62	66

a. The heat of adsorption is estimated by assuming C_6 to be fully contained in the 8-MR pockets

Chapter 4:

Site requirements and mechanism of ethanol dehydration on γ-Al_2O_3 as probed by kinetic studies

4.1 Introduction

4.1.1 Structure of γ-Al_2O_3

Gamma alumina (γ-Al_2O_3) is an inorganic material widely used in chemical industry as an acid catalyst and a catalyst support [1, 2, 4, 32] due to its surface acid sites, its high surface area (50-300 m^2/g), and its high thermal stability (stable at temperatures as high as 873 K [1, 4, 33])). The precursors of γ-Al_2O_3 are boehmite (γ-AlO(OH)), bayerite (α-$Al(OH)_3$), or gibbsite (γ-$Al(OH)_3$), which can be transformed into different transition aluminas such as gamma (γ), eta (η), theta (θ), and others. depending upon the synthesis temperature [1, 2, 33]. Thermal treatment of all these precursors and transition aluminas above 1473 K will transform these materials into the most stable phase of alumina, a low surface area (3-5 m^2/g) material referred to as alpha (α) alumina [33].

The crystallographic structure of γ-Al_2O_3 is difficult to characterize due to its low crystallinity. Four popular models for the structure of γ-Al_2O_3 have been proposed. The defect spinel model proposed by Gutierrez et al. [109] postulates that γ-Al_2O_3 can be considered as having an $MgAl_2O_4$ spinel structure with all the cations in the lattice replaced by Al atoms or vacancies. In the defect spinel model, 37.5% Al atoms exist in tetrahedral sites while 62.5% exist in the octahedral sites[110]. A non-spinel model was proposed by Krokidis et al. [3] based on the idea that γ-Al_2O_3 is topotactically transformed from its precursor, i.e. γ-Al_2O_3 inherits the structural characteristics of its precursor. In their study, molecular dynamics (MD) simulations using Hellmann-Feynman forces and density functional theory (DFT) calculations using the Perdew-Zunger functional for local density approximation (LDA) were employed to simulate the transformation of boehmite (γ-AlO(OH)) to γ-Al_2O_3. The obtained theoretical γ-Al_2O_3 structure is consistent with X-ray diffraction (XRD) patterns and the tetrahedral Al

content based on the results of ^{27}Al nuclear magnetic resonance (NMR) spectra (25% based on the simulation and 30% from experiments) [111, 112]. Paglia et al. [113] studied approximately 1.47 billion spinel-based models and subsequently proposed the two most likely structures based on geometric analysis and DFT calculations (Perdew-Burke-Ernzerhof (PBE) exchange correlation functional). One of the proposed models has $Fd\bar{3}m$ symmetry and, in the $Al_{64}O_{96}$ super cell of this model, 22 Al atoms are located in the tetrahedral site, 41 atoms are located in the octahedral sites, and 1 Al atom is located in a penta-coordinated site. The other proposed model has $I4_1/amd$ symmetry with 21 Al atoms in tetrahedral sites and 43 Al atoms in octahedral sites in the $Al_{64}O_{96}$ super cell. Ferreira et al. [114] used DFT calculations (PBE and van der Waals-aware density functional (vdW-DF)) with gauge-including projector augmented wave (GIPAW) method to simulate the ^{27}Al NMR spectra of these four models. The simulated results suggested that the $Fd\bar{3}m$ model has the best agreement with experimental NMR spectra among the four models [115, 116].

4.1.2 Surface active sites of γ-Al_2O_3

The surface of γ-Al_2O_3 has been shown to possess Brønsted acid sites, Lewis acid sites, and basic sites [39, 117-121]. Infrared (IR) spectroscopy using pyridine as a probe molecule (Pyridine IR) is a well-known technique to probe the existence of Brønsted and Lewis acid sites. The protonation of pyridine by Brønsted acid sites to form pyridium ions which results in a band at approximately 1540 cm^{-1} in the infrared spectrum, while pyridine coordinated to Lewis acid sites results in a band at 1450 cm^{-1} [40, 122]. The pyridine IR spectra of γ-Al_2O_3 possesses a band at approximately 1450 cm^{-1} but not at 1540 cm^{-1} on γ-Al_2O_3 [40, 123-125], showing that no pyridium ion formation occurs, consistent with ^{15}N NMR studies by Ripmeester that also note the absence of a peak at approximately 170 ppm attributed to pyridinium ions after pyridine exposure to γ-Al_2O_3 surface [121]. These results suggest that γ-Al_2O_3 either has no Brønsted acid sites or the Brønsted acidity of surface hydroxyls is too weak to protonate pyridine [40]. Digne et al. [35] simulated the adsorption of pyridine onto γ-Al_2O_3 surface using DFT calculations (Perdew Wang 91 (PW91) functional) and found the proton transfer from surface

hydroxyl group to pyridine was energetically unfavorable. The authors also suggested that the adsorption energy of pyridine depends not only on the acidity of the surface hydroxyl groups but also on steric factors based on their observation that the most acidic hydroxyl group on γ-Al_2O_3 has lower adsorption energy than hydroxyl groups with weaker acidity due to steric hindrance.

Lewis acid sites including three (Al_{III}), four (Al_{IV}), and five coordinated Al (Al_V) are generated by removal of surface hydroxyl groups as water from γ-Al_2O_3. The existence of different types of Lewis acid sites has been revealed by both NMR [118, 119, 121, 126], and IR spectroscopy [39-41]. The dehydration of γ-Al_2O_3 plays an important role in determining the identity and number of active sites on γ-Al_2O_3. Alcohol dehydration rates on alumina were reported to change with the temperature of thermal treatment [43] due to the varying extent of dehydration of γ-Al_2O_3. Hendriksen et al. [127] observed that the coverage of surface hydroxyls on γ-Al_2O_3 and α-Al_2O_3 decreased with thermal treatment temperatures (373-873 K) and the heat of adsorption of water at 298 K decreased from 45.4 to 15.8 kcal mol^{-1} when water uptake increased from $1.0x10^{14}$ to $8.0x10^{14}$ molecules cm^{-2}. Digne et al. [35] used DFT calculations to investigate the hydration and dehydration processes on different faces of γ-Al_2O_3. On the (100) surface at low surface hydroxyl coverage (θ_{100} = 4.3 OH nm^{-2}), the adsorbed water molecule is dissociated to form two hydroxyl groups on the surface and saturate an Al_V atom. However, water molecules were found to be physisorbed only at θ_{100} above 17.1 OH nm^{-2}, the point at which all surface Al atoms become saturated. Similar observations were noted on the (110) surface but the dissociation of water on Al_{III} was highly exothermic (240 kJ mol^{-1}) due to the strong acidity of Al_{III}. The calculated heat of water adsorption decreased with increasing coverage of surface hydroxyl groups on both the (100) (105-65 kJ mol^{-1}) and (110) surfaces (240-87 kJ mol^{-1}) as shown in Figure 4.1.1. Calculations indicated that the desorption energy of water (149-192 kJ mol^{-1}) from the fully hydrated (111) surface at θ_{111} = 11-15 OH nm^{-2} is much larger than that of the (100) and (110) surfaces (65-88 kJ mol^{-1}), due to both the larger number of hydrogen bonds and the high coordination of the oxygen atoms in the hydroxyl groups [35]. Wischert et al. [128] observed that the amount of Al-CH_3 species formed from the reaction of CH_4 on γ-Al_2O_3

at 423 K increased with increasing thermal treatment temperature up to 973 K due to the increasing number of Lewis acid sites generated. Liu [120] observed that the amount of pyridine that could be adsorbed onto the surface increased with increasing thermal treatment temperatures. Additionally, Liu and Truiit [39] also observed that pyridine adsorbed on a Lewis acid site can interact with neighboring OH groups.

4.1.3 Adsorption of alcohol and water on γ-Al_2O_3

In heterogeneous catalysis, adsorption is one of the key steps in reaction mechanisms. Cai et al. [129] used the semi-empirical PM3 basis set to simulate the chemisorption of various alcohols on γ-Al_2O_3 surface including methanol, ethanol, 1-propanol, and 2-methyl-1-propanol. Their results indicated that, for the formation of surface-bound alkoxide species, O-H bond cleavage in the alcohol is favored over C_α-O cleavage. Conversely, DeCanio et al. [45] suggested that both O-H cleavage and C_α-O cleavage occur during the formation of alkoxide species shown in Figure 4.1.2. When DeCanio et al. used temperature programmed desorption (TPD) to examine the methanol-O^{18} and ethanol-O^{18} desorption behaviors on γ-Al_2O_3, they observed H_2O^{18}, H_2O^{16}, ether- O^{18}, and ether- O^{16}. Clayborne et al. [130] used TPD-Fourier transform infrared spectroscopy (TPD-FTIR) to study the adsorption and reaction of C_1-C_5 primary alcohols on γ-Al_2O_3. They found that the amount of adsorbed alcohol at maximum monolayer coverage is nearly a constant for all of the C_1-C_5 primary alcohols ($8.2 \times 10^{-4} \pm 0.2 \times 10^{-4}$ mole alcohol per gram of γ-Al_2O_3) except ethanol (7.4×10^{-4} mole ethanol per g γ-Al_2O_3), suggesting that the carbon chain of the adsorbed alcohol is perpendicular to the surface. The lower amount of ethanol absorbed was thought to be caused either by the non-perpendicular adsorption of ethanol or by the competitive adsorption by water. The investigation of the adsorption of methanol using PM3 calculations suggested that the oxygen atom in methanol interacts with the surface Lewis sites for physisorption. Dabbagh et al. [131] investigated the adsorption of (S)-2-butanol and (R)-2-butanol on (100) surface on γ-Al_2O_3 using DFT (The double numerical plus polarization function (DNP) and BLYP functional). The calculated adsorption energies indicated that adsorbed (S)-2-butanol is slightly more stable than (R)-2-butanol (-29.95 kcal mol^{-1} and -28.15 kcal mol^{-1},

respectively). The authors also studied the dissociation of an adsorbed alcohol by modeling the proton transfer from an alcohol to a surface oxygen atom, forming a surface-bound alkoxide species on a surface Al atom and a surface hydroxyl group. The stability of the formed alkoxide and hydroxyl groups, and the activation energy of alcohol dissociation on the surface vary significantly depending on to which oxygen atom adjacent to the Lewis site the proton of (S)-2-butanol transfers. For example, the energy for alkoxide formation from physisorbed (S)-2-butanol was found to change from -6.83 kcal mol^{-1} to 9.19 kcal mol^{-1} between two different oxygen atoms. Similarly, the activation energy for the dissociation of (S)-2-butanol was found to change from 69.34 kcal mol^{-1} to 13.56 kcal mol^{-1} depending onto which oxygen atom the proton transfers.

Greenler [132] investigated the adsorption of methanol and ethanol on alumina consisting mainly of γ phase using IR spectroscopy. When this alumina was exposed to methanol (40 mm Hg pressure of methanol) at 308 K, the resulting IR spectrum possessed a band at 1420 cm^{-1} attributed to hydrogen bonded OH groups in the alcohol, indicating that either the adsorbed alcohols interacted with each other through hydrogen bonds, or the adsorbed alcohol interacted with surface hydroxyl groups. After evacuation under the pressure 10^{-6} mm Hg for 15 minutes, the bands attributed to physisorbed species disappeared, and the remaining spectrum, possessing bands at 2940, 2840, 1190, 1100, and 1030 cm^{-1}, was similar to the spectrum of $Al(OCH_3)_3$, containing bands at 2940, 2840, 1190, 1100, and 1040 cm^{-1}. Based on these observations, the author concluded that species that remained on the surface after evacuation were surface-bound methoxide species and that the methoxide species remained on the surface even at 703 K. An additional three bands (approximately 1597, 1394, and 1377 cm^{-1}) appeared when the authors heated the alumina sample to 443 K or higher, indicating the formation of a new surface species. Based on a comparison among the IR spectrum recorded at 533 K, the IR spectra of sodium formate, calcium formate, and aluminum formate, the authors suggested the new species formed upon heating is a surface formate as shown in Figure 4.1.3 (a), and assigned the bands at 1597, 1394, and 1377 cm^{-1} to an asymmetric COO stretching mode, a CH in-plane bending mode, and the symmetric COO stretching mode, respectively. When the authors used isotopically-labeled $H_3C^{13}OH$ instead of $H_3C^{12}OH$,

the COO stretching bands shifted but the band attributed to CH bending mode did not. This result is consistent with the hypothesis that the new species formed at 443 K is a surface-bound formate species. The adsorption of ethanol on alumina was also investigated in the same manner by the authors. The similarity between the IR spectrum of adsorbed ethanol after evacuation at 308 K and the IR spectrum of $Al(OCH_2CH_3)_3$ suggested that surface ethoxide species formed on the surface. At 433 K or above, the authors suggested that surface-bound acetate species formed based on a comparison of the IR spectrum recorded at 483 K and the IR spectrum of aluminum acetate. Because the dissociation of an adsorbed alcohol forms a surface alkoxide on a Lewis acid site and a surface hydroxyl group on a neighboring surface oxygen atom, Jeziorowski et al.[133] suggested that the configuration of an adsorbed alcohol could be such that the oxygen atom of the alcohol interacts with a surface Lewis site, and the proton in the alcohol OH group interacts with a surface oxygen atom as described on Figure 4.1.3 (b). Knözinger and Stübner [134] observed a decrease in the intensity of the band at 3775 cm^{-1} attributed to free surface hydroxyl groups on the tetrahedral Al atoms close to vacancies next to two Lewis acid sites during isobutyl alcohol adsorption on η-Al_2O_3 and γ-Al_2O_3 as shown in Figure 4.1.3 (c). Therefore, the authors suggested that there exists a surface species such that the oxygen in the OH group of the adsorbed alcohol interacts with two Lewis acid sites and the proton in the OH group of the alcohol interacts with the oxygen atom of the surface hydroxyl group as shown in Figure 4.1.3(d). Beebe et al. [135] investigated the adsorption of CH_3Cl on aluminum oxide deposited on CaF_2 using IR spectroscopy. The authors observed the formation of HCl and a decrease in the intensity of bands at approximately 3732 cm^{-1} and 3691 cm^{-1} attributed to surface hydroxyl groups, and concluded that surface methoxide species could be formed from the reaction of CH_3Cl with a surface hydroxyl group.

4.1.4 The kinetics and mechanisms of unimolecular and bimolecular alcohol dehydration on γ-Al_2O_3

Many mechanisms have been proposed for alcohol dehydration on alumina-based catalysts. Knözinger and his co-workers [43] measured the effects of alcohol and water

pressure on the rate of olefin formation for the dehydration of isobutanol, tert-butanol, and cyclohexanol at low conversion (< 3%). The formation of olefin was found to be zero order in alcohol pressure at pressures above a certain level (80 torr at 513 K for iso-butanol, 150 torr at 453 K for tert-butanol, and 80 torr at 453 K for cyclohexanol). Additionally, a strong inhibition of the olefin formation rate by water was observed and the degree of this inhibition decreased with increasing alcohol pressure. Based on these kinetic measurements, the author proposed a rate equation (Equation 4.1.1) for olefin formation for alcohol dehydration on aluminum oxide capable of describing the measured reaction rates.

$$r = \frac{\sqrt{P_A}}{\sqrt{P_A} + bP_W} \tag{4.1.1}$$

Where r is the rate of olefin formation, b is a constant, and P_A and P_W are the pressures of alcohols and water, respectively.

Knözinger and Scheglila [44] concluded that the rate-determining step (RDS) for olefin formation involved the C_β-H bond cleavage rather than O-H bond cleavage of alcohols or water desorption. They observed that the alcohol with deuterium atoms on C_β showed primary kinetic isotope effects (KIE), but no isotope effects was noted on the alcohol with O-D group at 423-453 K. From these observations, the authors proposed an E2-type mechanism in which the RDS involves simultaneous bond cleavage of C_β-H bond and C_α-OH bond in alcohol for olefin formation on aluminum oxide. The authors observed the measured KIE values decreased to a larger extent than the predicted KIE values based on transition state theory with increasing temperatures (393-483 K), and hence they suggested that, at high temperatures, the mechanism will shift from E2- to E1-type mechanism where the transition state is a carbenium-ion-like transition state. In addition, the KIE increased with decreasing extent of branching of the alcohol (tert-butanol < sec-butanol < iso-butanol), showing that the transition state possessed some ionic nature. Knözinger [43] rejected the hypothesis that the formation of olefin is from the desorption of a surface-bound alkoxide bound to a Lewis acid site based on the result that the rate of olefin formation did not decrease after poisoning the Lewis acid sites with

pyridine. However, our study showed that pyridine can inhibit the rate of ethylene formation, as will be discussed in section 4.3.

Pines and Haag [136] studied the dehydration of 1-butanol and 2-butanol dehydration on alumina oxide. They found that the cis/trans ratio for 2- butene generation is nearly identical for 1-butanol dehydration and 1-butene double-bond isomerization (cis/trans ratio approximately equal to 2). The same observation was also found for 2-butanol dehydration and 2-butene isomerization (cis/trans = 4.3), suggesting that alcohol dehydration and alkene isomerization occur through the same intermediate. The authors proposed a mechanism that comprises of the following sequence of steps: (1) An alcohol is adsorbed on either Brønsted acid sites or Lewis acids to form an oxonium ion (Step 1 in Figure 4.1.4), (2) subsequently this oxonium ion is decomposed to form a proton-olefin complex responsible for the high cis/tran ratio (Step 2 in Figure 4.1.4), and (3) this proton-olefin complex eliminates a proton to form the olefin (Step 3 in Figure 4.1.4). However, Knözinger and Scheglila [44] argued that the proton-olefin complex is unlikely to exist because the transition state for the formation of the proton-olefin complex formation would likely be described by C-H bond bending which should result in a small KIE. The measured primary KIE using deuterated alcohols contradicted the small KIE predicted for the proton-olefin complex formation.

Knözinger et al. [137] studied the dehydration of 2-butanol, 2-pentanol, 3-pentanol, 2-methyl-3-pentanol, and 3-methyl-3-pentanol. They also observed that cis-olefins are preferentially formed over trans-isomers(cis/trans ratio = 2.3-5.1). To explain this high cis/trans ratio, the authors proposed a transition state in which the substitution groups are in the cis-position. This transition state results in less steric hindrance when the transition state is close to the surface. Dabbagh et al. [131] investigated the E2-type mechanism of 2-butanol dehydration using DFT calculations (BLYP functional), and the calculations suggested that the conformation of adsorbed alcohol plays a key role in the cis/trans selectivity. The interactions between the surface and the adsorbate were found to be more significant in determining the cis/trans selectivity than intramolecular interactions. Kwak et al. [46] investigated the effects of van der Waals interactions on 2-butanol dehydration through an E1-type mechanism using DFT calculations (PBE functional [138]) with a

correction for dispersion forces (DFT-D). The calculations indicated that van der Waals interactions stabilized surface butoxide species. This stabilization results in the higher formation energy (ΔE) and activation energy (ΔE^a) for cis-2-butene and trans-2-butene from desorption of surface-bound 2-butoxide than the energies calculated without van der Waals interactions (Table 4.1.1). Two low-energy conformations of surface-bound butoxide, A and B as shown in Figure 4.1.5, lead to the formations of cis- and trans-2-butene, respectively. The calculated activation energy for cis and trans-2-butene formation are significantly different (108 and 147 kJ mol^{-1}, respectively), indicating that conformation A leads to a more stable transition state than conformation B as shown in Figure 4.1.5.

Knözinger and his co-workers [43, 139] observed that the rate of ether formation from ethanol, n-propanol, and benzyl alcohol has a zero order dependence on alcohol pressure above 160 torr of alcohol at 473 K. There was no effect of the ether produced on the reaction rate of ether formation. However, there was a strong inhibition of ether formation by water, and the degree of this inhibition became less significant with increasing temperature or alcohol pressure. The authors proposed a rate equation identical to that shown in Eq. 4.1.1 which can quantitatively describe the effects of water and alcohol on measured rate of ether formation. The strong negative effect of water on alcohol dehydration indicates that water adsorption is strong on γ-Al_2O_3 surface. To verify this observation, Roy et al. [47] exposed the γ-Al_2O_3 sample to 3 torr water vapor and then evacuated the sample at 373 K. Even after evacuation at 373 K, the sample still contained residual water (1800 $\mu mol\ g^{-1}$). After the authors exposed this water-treated sample to 2-propanol, they observed the following phenomena: (1) the amount of adsorbed 2-propanol decreased compared to the sample without water treatment, (2) there was no difference in the temperature of olefin formation in temperature programmed desorption studies (TPD) between the water-treated sample and untreated sample, and (3) most of the adsorbed water was not replaced by 2-propanol at 373 K. Based on these observations, the authors concluded that the adsorption of water on γ-Al_2O_3 is stronger than the adsorption of alcohols, and water simply blocks the surface active sites. Delgado et al. [140] investigated water adsorption on γ-Al_2O_3 using ^{1}H-NMR and they used DFT

(PW91 functional) to assign the experimentally observed peaks to different surface species present when exposing water onto γ-Al_2O_3 surface. The authors suggested that water can either be molecularly adsorbed onto the surface through hydrogen bonds to either the surface oxygen atoms or surface hydroxyl groups or water can coordinate to a Lewis acid site as shown in Figure 4.1.6.

Knözinger et al. [141] observed that there were no primary KIE effects for dimethyl ether formation on γ-Al_2O_3 using either CD_3OD or CH_3OD at 403- 453 K, demonstrating that the RDS does not involve the C-H bond cleavage, O-H bond cleavage, or water desorption. The authors proposed a mechanism for ether formation that involved a surface-bound alkoxide species reacting with a physisorbed alcohol, and the RDS involving the cleavage of the RO-Al bond. However, DeCanio[45] concluded that the ether formation is not due to the reaction between a surface-bound alkoxide and a physisorbed alcohol based on their observation that no desorption of alcohol was measured above 373 K during the TPD of methanol, ethanol, 1-propanol, and other alcohols. In contrast to olefin formation, Knözinger [43] observed that the rate of ether formation decreased by more than 50% after poisoning the acid sites on γ-Al_2O_3 using pyridine. Based on this result, Knözinger suggested that surface OH groups, surface basic sites, and Lewis sites are all necessary for ether formation on aluminum oxide. However, Baertsch et al. [142] suggested that the Lewis acid sites may be too weak to adsorb pyridine irreversibly based on their result that the rate of 2-butanol dehydration decreased by only 50% even after γ-Al_2O_3 was fully saturated with pyridine. Kwak et al. [143] concluded that BaO can selectively occupy penta-coordinate Al^{3+} (Al_V) on γ-Al_2O_3 based on their result that the intensity of the ^{27}Al-NMR peak at approximately 23 ppm, which is attributed to penta-coordinate Al^{3+}, decreased with increasing BaO deposition on the γ-Al_2O_3 surface. Additionally, the number of BaO deposited on the surface is equal to the amount of Al_V consumed, indicating that only one BaO molecule occupied one Al_V site. Kwak and his co-workers [143] observed that: (1) the rate of methanol dehydration on BaO/ γ-Al_2O_3 decreased monotonically with increasing BaO loading, and (2) the amount of strongly adsorbed ethanol (desorbed as ethylene at temperatures above 473 K)

is equal to number of Al_V sites on the surface. Based on these results, the authors concluded that the active site for alcohol dehydration involves an Al_V atom.

Shi and Davis [42] observed that the percentage of di-2-butyl or dimethyl ether formed from 2-butanol and methanol dehydration, respectively, increased linearly with the square of the corresponding alcohol pressure at a constant total alcohol pressure. This observation contradicts the half order dependence of alcohol pressure proposed by Knözinger. Shi and Davis [42] observed that the ether formed during dehydration of (S)-2-butanol on aluminum oxide mainly consists of (S,R)-ether. Based on this observation, the authors proposed a S_N2 mechanism for ether formation and an E1-type mechanism for olefin formation on aluminum oxide as shown in Figure 4.1.7.

Due to the complexity of the surface sites on γ-Al_2O_3 surface and the undetermined structure of γ-Al_2O_3, the outstanding questions for alcohol dehydration on γ-Al_2O_3, including reaction mechanisms, rate equations, and site requirements for olefin and ether formation have not been resolved. Specifically, this research will attempt to describe a reaction scheme and associated kinetic model consistent with observations regarding (I) ethanol pressure dependence, (II) reversible inhibition by water, (III) KIE values of isotopically-labeled ethanol, (IV) titration of active site using pyridine, lutidine, and CO_2.

4.2 Materials and methods

4.2.1. Catalyst preparation

Gamma alumina (BET surface area =195 m^2/g^{-1}, pore volume =0.188 cm^3g^{-1}) from Alfa Aesar was used as a catalyst for kinetic experiments after treatment with a 1M NH_4NO_3 solution at 353 K for 3 h. The gamma alumina was sieved to maintain particle sizes between 180 and 425 μm (40–80 mesh) and subsequently treated in dry air (1.67 cm^3 s^{-1} at NTP conditions, Ind. Grade, Matheson Tri-gas) by increasing the temperature from ambient to 723 K at a rate of 0.0167 K s^{-1} and holding the temperature of the catalyst at 723K for 4 hrs to remove any organic impurities on the catalyst surface.

4.2.2. Steady-state catalytic reactions of ethanol dehydration

Steady-state ethanol dehydration reactions were carried out in a tubular packed-bed quartz reactor (10 mm inner diameter) under atmospheric pressure (He as carrier gas) and at differential conditions (<10% conversion). Catalyst samples (0.02 g) were supported on a coarse quartz frit inside the reactor, and the temperature was controlled using a furnace (National Electric Furnace FA120 type) connected to a Watlow Temperature Controller (96 series). Catalyst samples were diluted with acid-washed quartz particles (0.5–0.8 g, 152–422 μm, Acros Organics). Catalyst temperatures were measured using a K-type thermocouple touching the bottom of a well on the external surface of the quartz reactor. Catalyst samples were treated in air (1.67 cm^3 s^{-1} at NTP conditions, Ind. Grade, MATHESON TRI-GAS) at 723 K (0.0167 K s^{-1}) for 4 h and then the sample was cooled in air flow (1.67 cm^3 s^{-1}) to reaction temperatures (403-488 K). The catalyst was then exposed to 2.2 kPa of H_2O for 1 h at 488K prior to reaction to eliminate any active sites that would deactivate during reaction due to the irreversible adsorption of H_2O.

Liquid C_2H_5OH (≧ 99.5%, Decon Laboratories, Inc.), C_2H_5OD (99.5 at.% D, Sigma–Aldrich), C_2D_5OD (99.5 at.% D, Sigma-Aldrich) or water were vaporized at 405 K into a carrier gas flow, which contained He (0.55–3.3 cm^3 s^{-1}at NTP condition) and a mixture of Ar/CH_4 (0.0137–0.0297 cm^3 s^{-1} at NTP conditions; 75% Ar and 25% CH_4, Minneapolis oxygen) as an internal standard. Transfer lines were maintained at temperatures greater than 343 K by resistive heating to prevent any condensation of the reactants or products. The partial pressures of ethanol and water were always kept below their respective vapor pressures at ambient temperature to further avoid condensation.

To analyze the effects of ethylene pressure on ethanol dehydration, ethylene (chemically pure, MATHESON TRI-GAS) was introduced into the reactant stream after the ethanol dehydration reactions achieved steady-state at 458 K under atmospheric pressure. The partial pressure of ethylene (0.0–13.0 kPa) was controlled by adjusting the flow rate of ethylene at a fixed ethanol pressure (1.5 kPa).

Similarly, for CO_2 poisoning experiments, the ethanol dehydration reaction was allowed to reach steady state at 488K in 110 kPa of He before CO_2 (Grade 4, MATHESON TRI-GAS) was fed to the reactor. The flow rate of CO_2 to the reactor was

adjusted at a fixed ethanol pressure (0.8kPa) to control the partial pressure of CO_2 (0.0-47.0kPa).

To analyze the composition of the products, the reactor effluent was sent via heated transfer lines to a mass spectrometer (MKS Cirrus 200 Quadrupole mass spectrometer system) and/or to a gas chromatograph (Agilent 6890 N GC) equipped with a methyl-siloxane capillary column (HP-1, 50.0 m x 320 μm x 0.52 μm) connected to a flame ionization detector and a packed column (SUPELCO HAYESEP R 80/100 mesh packed column, 12 ft) connected to a thermal conductivity detector.

4.2.3 Estimation for parameters in kinetic models

Athena Visual Studio (v14.2, W. E. Stewart and M. Caracotsios) were used to optimize parameters in kinetic models proposed in this work and to evaluate uncertainties of these parameters based on Bayesian Estimation techniques. The uncertain reported in this work is the 95% marginal highest probability density intervals.

4.3 Results and discussion

4.3.1 Irreversible deactivation by water

Ethylene and diethyl ether (DEE) were observed as products of unimolecular and bimolecular dehydration ethanol at 488 K, respectively. In a γ-Al_2O_3 sample treated in air at 723 K for 4 h, reaction rates of ethylene and DEE formation slowly decreased with time as shown in Figure 4.3.1. However, on the γ-Al_2O_3 sample which was exposed to water (2.2 kPa) for 1h at 488 K before reaction, the rates of ethylene and DEE formation were found to be independent of time and lower than the sample without prior exposure to water as shown in Figure 4.3.1. These observations show that irreversible deactivation occurs for both ethylene and DEE formation when γ-Al_2O_3 is exposed to water. Thus, a fraction of sites on γ-Al_2O_3 that result in catalytic synthesis of ethylene and DEE are irreversibly deactivated by water produced during ethanol dehydration. Digne et al. [35] found that water adsorbed on Lewis acid sites preferentially dissociates to form surface hydroxyls on the γ-Al_2O_3 surface and that the acidity of these surface hydroxyl groups

formed is too weak to protonate pyridine based on their DFT calculations. Roy et al. [47] concluded that water blocks the surface active sites on γ-Al_2O_3 based on Temperature Programmed Desorption (TPD) experiments. The authors observed that (1) the amount of adsorbed 2-propanol on a sample that has been exposed to water (they exposed the γ-Al_2O_3 sample to 3 torr water vapor and then evacuated the sample at 373 K) decreased compared to a sample without water treatment (normal sample), and (2) there was no difference in the temperature at which olefin formation was observed between the water-treated sample and a normal sample. On the same lines, Wischert et al. [128] observed that the nunber of Al-CH_3 species formed from the reaction of CH_4 on γ-Al_2O_3 at 423 K increased with decreasing coverage of surface hydroxyl groups. Because water can cause irreversible deactivation of active centers involved in ethanol dehydration, all subsequent kinetic measurements for ethanol dehydration reported herein were performed after exposing the γ-Al_2O_3 sample to water.

4.3.2 Site requirements for ethanol dehydration

The surface of γ-Al_2O_3 contains Lewis acid sites, surface hydroxyl groups and basic sites [35, 38, 39, 121]. However, the types of surface sites required for olefin and ether formation in dehydration reactions of alcohols are still debated. Knözinger [43] suggested that the active sites required for olefin formation are either surface hydroxyl groups or basic sites based on their observation that pyridine poisoning had no effects on rate of olefin formation. Zotov et al. [36] used electron paramagnetic resonance (EPR) spectroscopy to characterize the number of strong electron acceptor site (strong acid site), weak electron acceptor site (weak acid site) and donor sites (basic site) on aluminum oxide samples doped with SO_4^{2-}, Cl^- and Na^+, individually. The authors found that SO_4^{2-} and Cl^- doping increased the number of weak acceptor acid sites, but Na^+ doping decreased the number of weak acceptor sites. Furthermore, they found that the correlation between the rate of ethylene formation and the number of weak acceptor sites is a straight line passing through the origin; showing that weak acceptor sites are responsible for ethylene formation instead of strong acceptor or basic sites. Because SO_4^{2-} doping is known to generate Brønsted acid sites and Na^+ can exchange with the Brønsted acid sites,

the authors suggested that weak acceptor sites are Brønsted sites (surface hydroxyl groups). Contrary to these results, Kwak and his co-workers [143] observed that: (1) the rate of methanol dehydration on BaO/ γ-Al_2O_3 decreased monotonically with increasing BaO loading, which can selectively occupy surface penta-coordinated Al atoms (Al_V), and (2) the amount of strongly adsorbed ethanol (desorbed as ethylene at temperatures above 473 K) is equal to number of Al_V sites on the surface. Based on these results, the authors concluded that the active site for alcohol dehydration involves an Al_V atom. In this work, CO_2, pyridine and 2,6-dimethylpyridine (lutidine) were used to study the site requirements for olefin and ether formation.

The measured rates of DEE and ethylene formation at 488 K are independent of CO_2 pressure up to 47 kPa as shown in Figure 4.3.2. It is likely that CO_2 was adsorbed onto the γ-Al_2O_3 sample under these conditions based on CO_2 adsorption experiments by Rosynek [38] who exposed a γ-Al_2O_3 sample to 700 torr of CO_2 at 295 K for 24 hrs and then measured the amount of CO_2 that remained on γ-Al_2O_3 after evacuation for 24 hrs at different temperatures (295-773 K). Based on these results, the amount of CO_2 that remained on the γ-Al_2O_3 at 488 K is approximately 2.4 CO_2 molecules nm^{-2}, which is ~ 40% of the amount of CO_2 adsorbed at 295 K. Therefore, CO_2 adsorption does not affect the rates of ethylene or DEE formation, indicating that basic sites are unlikely to be directly involved in either ethylene or DEE formation.

To verify the role of acid sites in ethylene and DEE formation from ethanol dehydration on γ-Al_2O_3, pyridine and lutidine were used to poison the acid sites on γ-Al_2O_3 during ethanol dehydration. When pyridine was introduced onto γ-Al_2O_3 during reaction, the rates of DEE and ethylene formation both decreased with increasing pyridine pressure and the rate of ethylene formation relative to the rate without pyridine poisoning decreased to a larger extent than that of DEE formation as shown in Figure 4.3.3, indicating that ethylene and DEE are formed on different types of acid sites. At a pyridine pressure of 0.3 kPa, the rate of DEE and ethylene formation decreased by 90% and 96%, respectively, showing that acid sites are necessary to DEE and ethylene formation. After stopping pyridine feed to the reactor, the rates of DEE and ethylene formation returned to the value before pyridine introduction, showing that pyridine is

reversibly adsorbed onto the acid sites of γ-Al_2O_3 and ethanol is able to replace the adsorbed pyridine. Lutidine was also found to inhibit the rates of DEE and ethylene formation, but the degree of this inhibition was weaker than that of pyridine as shown in Figures 4.3.3 and 4.3.4. The two methyl groups on lutidene are expected to cause steric hindrance during adsorption onto Lewis acid sites [144], and, hence, may result in weaker inhibition of ethanol dehydration rates than pyridine. As lutidine (0.56 kPa) was introduced to the reactor at 488 K, the rate of ethylene and DEE formation decreased by 48% and 79%, respectively, compared to the rate measured in absence of lutidine as shown in Figure 4.3.4, consistent with the hypothesis that ethylene and DEE formation occur on different sites.

Based on the observation above, we conclude that acid sites rather than basic sites are necessary for ethylene and DEE formation from ethanol dehydration on γ-Al_2O_3. Zotov et al. [36] found that the number of acid sites on γ-Al_2O_3 increased with increasing the concentration of SO_4^{2-} and Cl^- doped on γ-Al_2O_3, while the number of basic sites decreased. The observed rate of ethylene formation from ethanol dehydration at 503 K on γ-Al_2O_3 doped with SO_4^{2-} and Cl^- was larger than the rate on γ-Al_2O_3 without doping. Therefore, the authors also concluded that acid sites are related to ethylene formation. However, our pyridine and lutidine experiments are not able to distinguish the identity of the acid sites involved in the formation of DEE and ethylene from ethanol dehydration on γ-Al_2O_3 because they are unspecific titrants of Lewis acidity.

4.3.3 Kinetic isotope effects for isotopic labeling ethanol

C_2D_5OD and C_2H_5OD were used to probe the rate-determining steps (RDS) for DEE and ethylene formation on γ-Al_2O_3 at 488 K. The measured rates and kinetic isotope effects (KIE) are shown in Tables 4.3.1 and 4.3.2. No significant difference was observed for the rate of DEE formation from C_2H_5OH, C_2D_5OD, and C_2H_5OD as shown in Tables 4.3.1 and 4.3.2. Knözinger et al. [141] also observed no KIE for dimethyl ether formation using CD_3OH, CD_3OD, and CH_3OD, leading the authors to suggest that the RDS of ether formation involves either a C_α-O or an O-Al bond cleavage. A primary KIE was measured for ethylene formation when introducing C_2D_5OD, while no KIE was

observed when using C_2H_5OD. These observations show that the RDS of ethylene formation involves C-H bond cleavage. Similarly, Knözinger and Scheglila [44] observed that alcohols with deuterium atoms in the C_β position demonstrated primary kinetic isotope effects (KIE), but no isotope effects were noted for alcohols with an O-D group at 423-453 K. Therefore, the authors concluded that the RDS step for olefin formation involves C_β-H bond cleavage rather than O-H bond cleavage or water desorption. Here, we also conclude that the RDS of ethylene formation involves C_β-H bond cleavage.

4.3.4 Kinetics and mechanism for ethanol dimerization into diethyl ether on γ-Al_2O_3

It has been reported that alcohols react with surface Brønsted acid sites to form water and surface bound alkoxide species on both zeolites and heteropolyacids [69, 80]. If surface hydroxyl groups on γ-Al_2O_3 behave as Brønsted acid sites, then DEE formation may occur via the reaction of a surface-bound ethoxide species and an ethanol molecule as shown in Figure 4.3.5. The requirement of an ethoxide species for DEE formation was probed using ethylene co-feed experiments. If the formation of DEE involves an ethoxide species as an intermediate, the rate of DEE formation should increase with increasing ethylene pressure due to the increased coverage of ethoxide species with increasing pressure of ethylene (0-13 kPa). However, the rate of DEE formation at 485 K is independent of ethylene pressure as shown in Figure 4.3.6. These data suggested either that this mechanism does not occur or that ethylene does not adsorb on hydroxyl groups of γ-Al_2O_3 to form ethoxide species. Digne et al. [35] found that surface hydroxyl groups on γ-Al_2O_3 surface are not acidic enough to protonate pyridine.

The measured rate of DEE formation as a function of both ethanol and water pressure are shown in Figures 4.3.7 and 4.3.8. The rate of DEE formation on γ-Al_2O_3 increased with increasing ethanol pressure and the slope of the curve decreased at higher ethanol pressure as shown in Figure 4.3.7. At a water pressure of 0.4 kPa, the rate of DEE formation was found to be independent of ethanol pressure above 4 kPa ethanol. Because DEE formation involves bimolecular dehydration of ethanol, this observed zero order dependence in ethanol pressure implies the existence of surface ethanol dimeric species

(ethanol dimer) on γ-Al_2O_3 surface. The measured rate of DEE formation decreased significantly with increasing water pressure as shown in Figure 4.3.8. A dimer-mediated mechanism for DEE formation was proposed (Figure 4.3.9) which would account for these observed pressure dependence. The mechanism involves ethanol adsorption onto an acid site to form an ethanol monomer (Step 1, Figure 4.3.9) and co-adsorption of a second ethanol molecule onto the same acid site to form an ethanol dimer (Step 2, Figure 4.3.9). Subsequent dehydration of the two co-adsorbed molecules forms DEE and water and regenerates the acid site (RDS, Step 3, Figure 4.3.9). Alternatively, a water molecule can absorb onto an acid site to form water monomer (Step 4, Figure 4.3.9), and subsequent co-adsorption of a second water (Step 5, Figure 4.3.9) or ethanol molecule (Step 6, Figure 4.3.9) onto the same acid site to form either a water dimer or a co-adsorbed water-ethanol complex, respectively. Shi and Davis [42] concluded that ether formation on aluminum oxide is through an S_N2 mechanism based on their observation that the ether formed during dehydration of (S)-2-butanol on aluminum oxide mainly consists of (S,R)-ether. Therefore, dimer activation is likely through an S_N2 transition state.

The rate equation derived from this mechanism based on quasi-equilibrium assumption is shown in Eq. 4.3.1. If the surface is mainly occupied by water-ethanol complexes and ethanol dimers, Eq. 4.3.1 can be simplified into Eq. 4.3.2. Eq. 4.3.2 is consistent with both the observed zero-order dependence in ethanol pressure and the negative effects of water on the rate of DEE formation (fit to experimental data is shown in Figure 4.3.10).

$$r_{DEE} = \frac{k_{DEE} K_{A1} K_{A2} P_{EtOH}^2}{(1 + K_{A1} P_{EtOH} + K_{W1} P_{H_2O} + K_{W1} K_{AW} P_{EtOH} P_{H_2O} + K_{A1} K_{A2} P_{EtOH}^2 + K_{W1} K_{W2} P_{H_2O}^2)} \quad (4.3.1)$$

$$r_{DEE} = \frac{k_{DEE} K_{A1} K_{A2} P_{EtOH}^2}{(K_{W1} K_{AW} P_{EtOH} P_{H_2O} + K_{A1} K_{A2} P_{EtOH}^2)} \quad (4.3.2)$$

The rate parameter, k_{DEE}, is the intrinsic rate constant for dimer activation (Step 3, Figure 4.3.9); K_{A1} and K_{A2} are the adsorption equilibrium constants for ethanol monomer (Step 1, Figure 4.3.9) and dimer (Step 2, Figure 4.3.9) formation, respectively; K_{W1} and K_{W2} are the adsorption equilibrium constants for water monomer (Step 4, Figure 4.3.9)

and dimer (Step 5, Figure 4.3.9) formation, respectively; K_{AW} is the adsorption equilibrium constant for water-ethanol complex (Step 6, Figure 4.3.9). P_{EtOH} and P_{H_2O} are partial pressures of ethanol and water, respectively. The values of these rate and equilibrium constants in Eq. 4.3.2 are shown in Table 4.3.3. The ratio of equilibrium constants, $K_{W1}K_{AW}/ K_{A1}K_{A2}$ is 4.28, indicating that water-ethanol complexes are more stable than ethanol dimers at 488 K, which explains the strong inhibition of water on DEE formation.

4.3.5 Kinetics and mechanism for unimolecular ethanol dehydration into ethylene on γ-Al_2O_3

The measured rate of DEE formation on γ-Al_2O_3 is approximately one order of magnitude greater than the rate of ethylene formation at 488 K as shown in Table 4.3.1. It has been reported that DEE can be converted to form ethylene on solid acid catalysts [43, 145]. To verify the source of ethylene formed under our reaction conditions (T= 488 K, conversion < 10%), ethanol and DEE was co-fed onto γ-Al_2O_3 and the resulting rate of ethylene formation was measured and is shown in Figure 4.3.11. No significant difference in the rate of ethylene formation was observed between the reaction with DEE co-feed (0.2 kPa DEE) and without DEE co-feed (0.04 kPa DEE pressure, which is from the DEE produced when only ethanol was fed at 488 K). This result shows that the ethylene formed on γ-Al_2O_3 under our reaction conditions (T=488 K, conversion < 10%) is produced predominantly from the dehydration ethanol.

The measured rate of ethylene synthesis as a function of ethanol pressure and water pressure are shown in Figures 4.3.12 and 4.3.13. The measured rate of ethylene formation on γ-Al_2O_3 was largely independent of ethanol pressure at different water pressures, as shown in Figure 4.3.12. Additionally, the measured rate of ethylene formation decreased with increasing water pressure, as shown in Figure 4.3.13. However, the degree of this water inhibition decreased with increasing ethanol pressure as shown in Figure 4.3.13, implying competitive adsorption of water and ethanol. The rates of ethylene and DEE formation returned to the rate before water introduction, showing that water inhibition is reversible after treating γ-Al_2O_3 with water (2.2 kPa) for

1 h prior to reaction. The hydration processes on γ-Al_2O_3 surface was investigated by Digne et al. [35] using DFT calculations. Their calculations show that water preferentially dissociates on Lewis acid sites to form surface hydroxyl groups. After water saturates all available surface Lewis acid sites, water becomes molecularly adsorbed on the surface. Therefore, the observed reversible inhibition by water from our data are consistent with these DFT reports and show that water is molecularly adsorbed on the surface of γ-Al_2O_3 treated with water.

Pines and Haag [136] studied the dehydration of 1-butanol and 2-butanol dehydration on alumina oxide. They found that the cis/trans ratio for 2-butene generation is nearly identical for both 1-butanol dehydration and 1-butene double-bond isomerization (cis/trans approximately equal to 2). The same observation was also found for 2-butanol dehydration and 2-butene isomerization (cis/trans = 4.3), suggesting that alcohol dehydration and alkene isomerization occur through the same intermediate. However, the same cis/trans ratio for alcohol dehydration and olefin double bond isomerization cannot be explained by the E_2-type mechanism proposed by Knözinger and Scheglila [44], where the RDS involves the simultaneous C-H and C-OH bond cleavage in an alcohol adsorbed on γ-Al_2O_3 surface. Macht et al. [68] also observed that the cis/trans 2-butene ratio is nearly identical for 2-butanol dehydration and 1-butene isomerization on polyoxometalate. As a result, the authors suggested that surface-bound alkoxide species are common intermediates for these two reactions. Thus, a mechanism, that is ethoxide-mediated as shown on Figure 4.3.14, was proposed and this mechanism would account for the observed pressure dependence in ethanol and water for unimolecular ethanol dehydration. This mechanism includes adsorption of an ethanol molecule on an acid site to form an ethanol monomer (Step 1, Figure 4.3.14) and subsequent decomposition of this ethanol monomer to form a surface-bound ethoxide species and surface-bound hydrogen atom in the form of a hydroxyl group on the γ-Al_2O_3 surface (Step 2, Figure 4.3.14). Desorption of the surface-bound ethoxide intermediate generates ethylene and leaves a surface hydroxyl group on the surface (RDS, Step 3, Figure 4.3.14). Subsequent desorption of the surface hydroxyl group and hydrogen atom form a water molecule (Step 4, Figure 4.3.14). Alternately, water can absorb onto an acid site to form a water

monomer (Step 5, Figure 4.3.14) and co-adsorption of a second water (Step 6, Figure 4.3.14) or an ethanol molecule (Step 7, Figure 4.3.14) on the same acid site forms a water dimer or a co-adsorbed water-ethanol complex, respectively. Ethanol monomers can interact with other ethanol molecules to form ethanol dimers (Step 7, Figure 4.3.14).

The rate equation derived from this mechanism is shown in Eq. 4.3.3. If the surface is mainly occupied by ethanol monomers, water-ethanol complexes, ethanol dimers, and water dimers, Eq. 4.3.3 can be simplified to Eq. 4.3.4. Eq. 4.3.4 is consistent with both the observed zero-order dependence in ethanol pressure and negative effects of water pressure on the rate of ethylene formation (fitting to experimental data shown in Figure 4.3.15).

$$r_{C_2H_4} = \frac{k_{C_2H_4} K_{A1} K_d P_{EtOH}}{(1+K_{A1}P_{EtOH}+K_{W1}P_{H_2O}+K_{W1}K_{AW}P_{EtOH}P_{H_2O}+K_{A1}K_{A2}P_{EtOH}^2+K_{W1}K_{W2}P_{H_2O}^2)} \quad (4.3.3)$$

$$r_{C_2H_4} = \frac{k_{C_2H_4} K_{A1} K_d P_{EtOH}}{(K_{A1}P_{EtOH}+K_{W1}K_{AW}P_{EtOH}P_{H_2O}+K_{A1}K_{A2}P_{EtOH}^2+K_{W1}K_{W2}P_{H_2O}^2)} \quad (4.3.4)$$

The rate parameter $k_{C_2H_4}$ is the intrinsic rate constant for ethoxide desorption (Step 3, Figure 4.3.14) and K_d is the equilibrium constant for ethanol dissociation (Step 2, Figure 4.3.14); K_{A1} and K_{A2} are the adsorption equilibrium constants for ethanol monomer (Step 1, Figure 4.3.14) and dimer formation (Step 8, Figure 4.3.14), respectively; K_{W1} and K_{W2} are the adsorption equilibrium constants for water monomer (Step 5, Figure 4.3.14) and dimer formation (Step 6, Figure 4.3.14), respectively; K_{AW} is the adsorption equilibrium constants for water-ethanol complex formation (Step 7, Figure 4.3.14). P_{EtOH} and P_{H_2O} are partial pressures of ethanol and water, respectively.

The values of rate and equilibrium constants in Eq. 4.3.4 are shown in Table 4.3.4. The calculated values for $K_{A1}K_{A2}/K_{W1}K_{AW}$ and $K_{A1}K_{A2}/K_{W1}K_{W2}$ using values in Table 4.3.4 are 0.043 and 0.063, respectively, indicating that water-ethanol complexes and water dimers are more stable than ethanol dimers on the acid sites responsible ethylene generation at 488 K. Therefore, to observe the inhibition of DEE formation by ethanol dimer requires ethanol pressure at least an order of magnitude larger than the water pressure. The calculated value of $K_{W1}K_{AW}/ K_{W1}K_{W2}$ and $K_{W1}K_{AW}/K_{A1}$ are 1.5 and 0.83,

respectively, indicating that the stability of ethanol monomer is comparable to the stability of water-ethanol complexes and water dimers, which explains why the degree of water inhibition decreases with increasing ethanol pressure.

For ethanol dehydration on γ-Al_2O_3, water can irreversibly deactivate the rates of ethylene and DEE formation. This irreversible deactivation is likely due to saturation of surface Lewis acid sites by water dissociation. Acid sites are responsible for ethylene and DEE formation but ethylene and DEE occur on different acid sites, reflecting the complexity of surface acid sites on γ-Al_2O_3. However, the identity of the acid sites related to DEE and ethylene formation could not be determined in this work. The mechanism proposed for unimolecular dehydration of ethanol, where ethylene formation is through desorption of surface-bound ethoxide species, is consistent with measured primary KIE for C-H bond cleavage and the same cis/trans ratio for alcohol dehydration and olefin double-bond isomerization reported in the literature [136]. The mechanism proposed for bimolecular dehydration of ethanol, where DEE formation is through the activation of surface ethanol dimer, is consistent with measured KIE for C-O bond cleavage and the measured zero-order dependence in ethanol.

4.4 Conclusions

Steady-state kinetic measurements of ethanol dehydration on γ-Al_2O_3 showed that γ-Al_2O_3 can catalyze the dehydration of ethanol to both diethyl ether (DEE) and ethylene, but the rate of DEE formation is approximately an order of magnitude larger than the rate of ethylene formation at 488 K. The introduction of pyridine on γ-Al_2O_3 reversibly inhibits both DEE and ethylene formation while CO_2 co-feed has no effect on the rates of DEE and ethylene formation, indicating that acid sites and not the basic sites, are required for DEE and ethylene formation. Lutidine decreased the rates of DEE and ethylene formation to varying extents, suggesting that DEE and ethylene formation require different types of acid sites. The measured kinetic isotope effects (KIE) for C_2D_5OD and C_2H_5OD dehydration show that the rate determining step (RDS) for ethylene formation involves C_β-H bond cleavage and that the RDS for DEE formation involves C_α -O bond cleavage. The measured rates of DEE and ethylene formation increased with increasing

ethanol pressure and then became independent of ethanol pressure, while the presence of water had a negative effect on the rates of both DEE and ethylene formation. These observations are consistent with the proposed mechanisms in which DEE formation occurs via the activation of surface-bound ethanol dimer species and ethylene formation occurs via the desorption of surface-bound ethoxide species.

Acknowledgement

We acknowledge the financial support from Dow Chemical Coporate. We acknowledge Joseph DeWild, and Chris Ho for assistance with reaction studies.

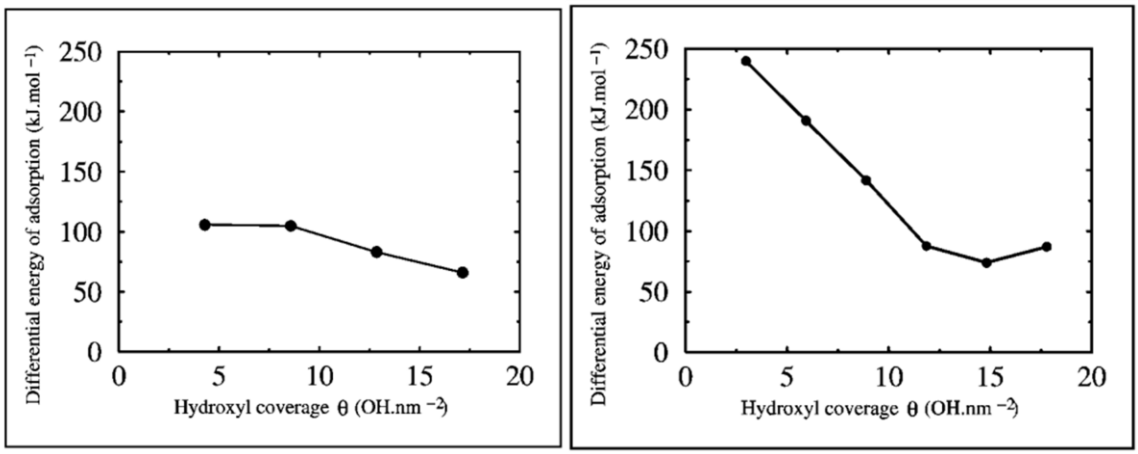

Figure 4.1.1 The absolute value of the differential energy of adsorption as a function of surface hydroxyl coverage (θ) on the (a) γ -Al_2O_3(100), (b) γ -Al_2O_3(110). This figure was adapted from [35].

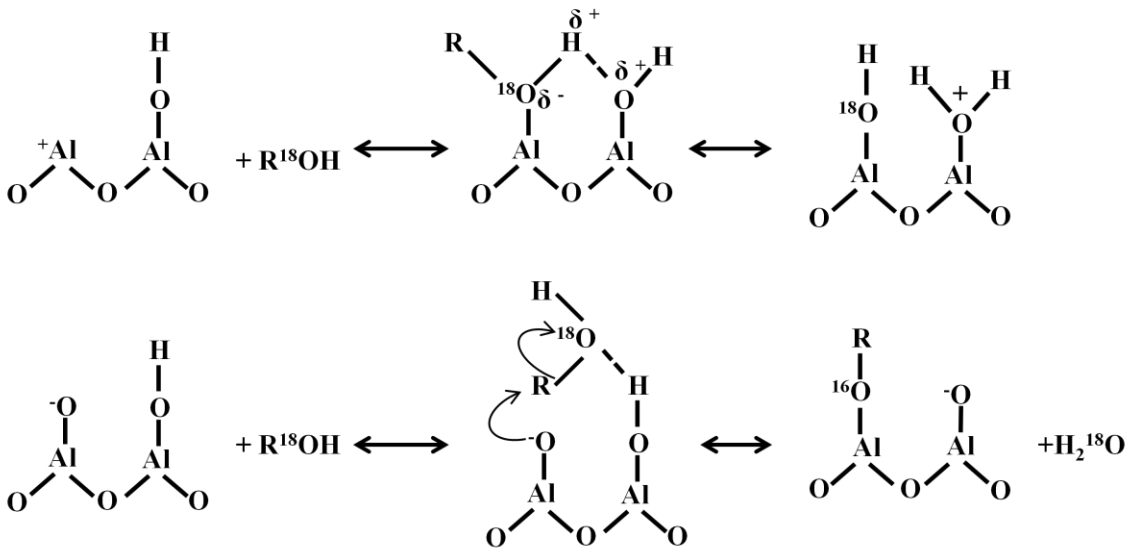

Figure 4.1.2. Two mechanisms for alkoxide formation on aluminum oxide. The mechanisms were adspted from [45].

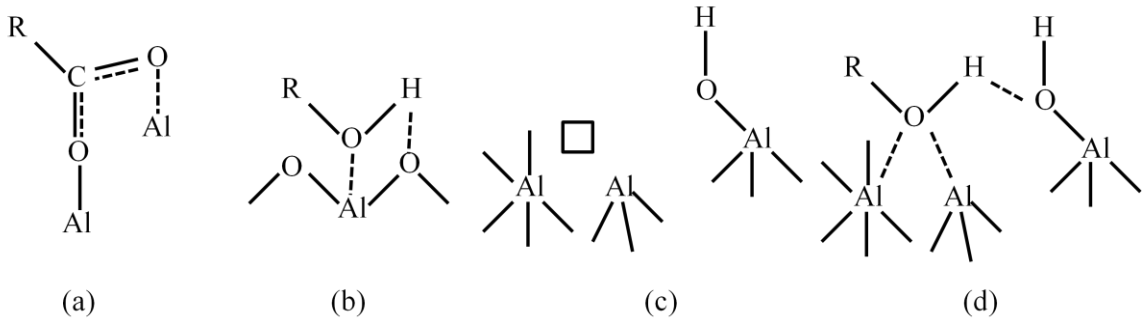

Figure 4.1.3. Surface species on aluminum oxide during alcohol adsorption. □ corresponds to an empty site. The figure was adapted from [134].

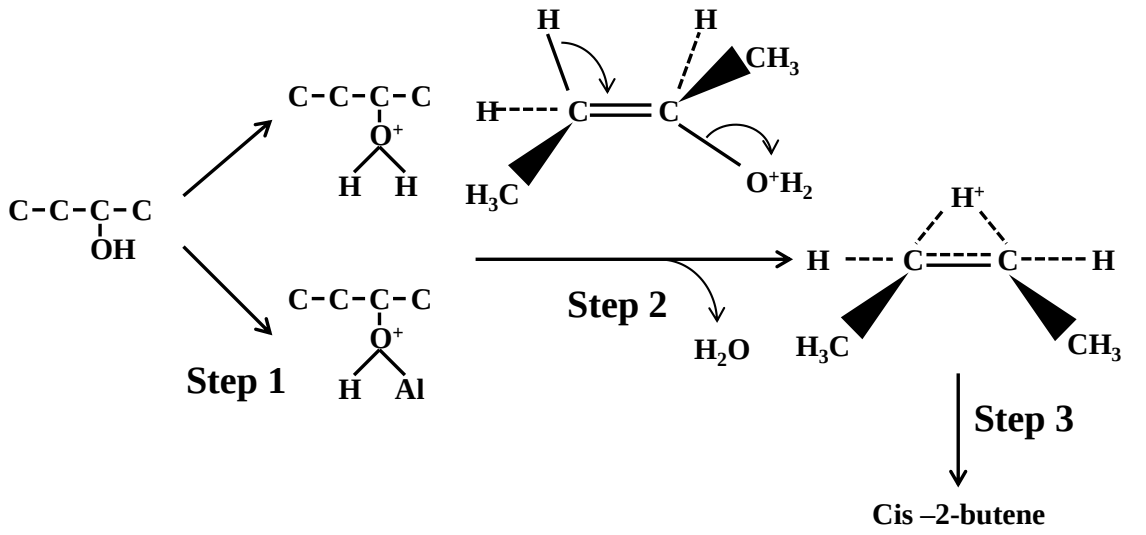

Figure 4.1.4. The mechanism for olefin formation proposed by Pines and Haag. The mechanism was adapted from [136].

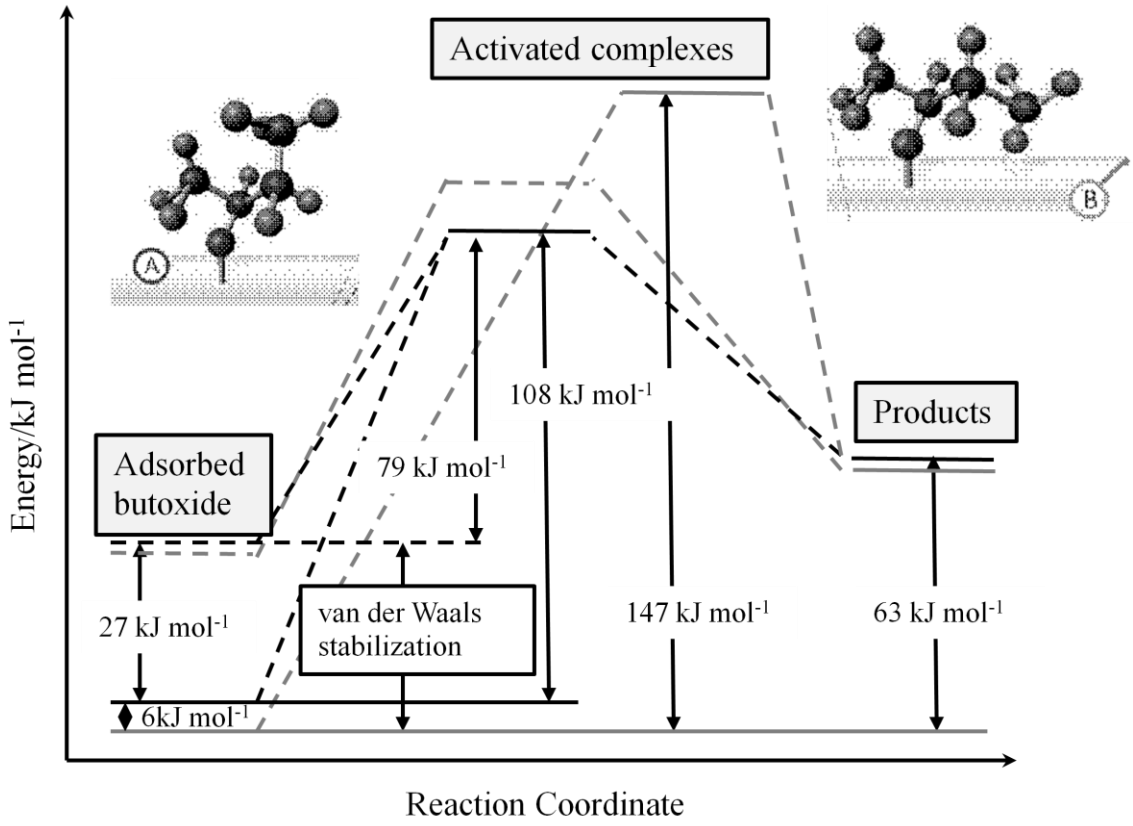

Figure 4.1.5. The conformations of the surface-2-butoxide and the energy profiles for the cis- and trans-2-butene formations. This figure was adapted from [46].

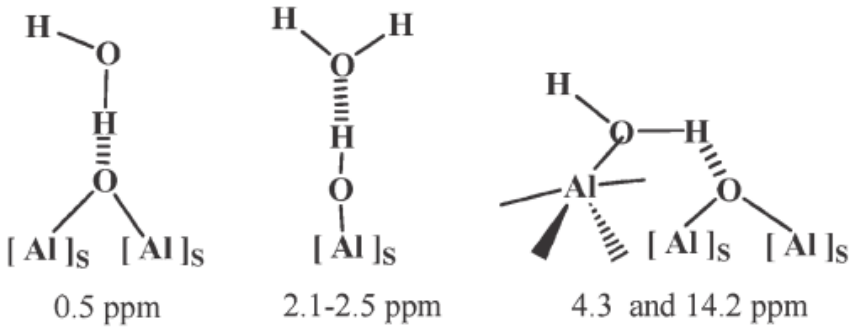

Figure 4.1.6. The structures of adsorbed water on γ-Al_2O_3 and the corresponding chemical shift on ^{1}H-NMR from [140].

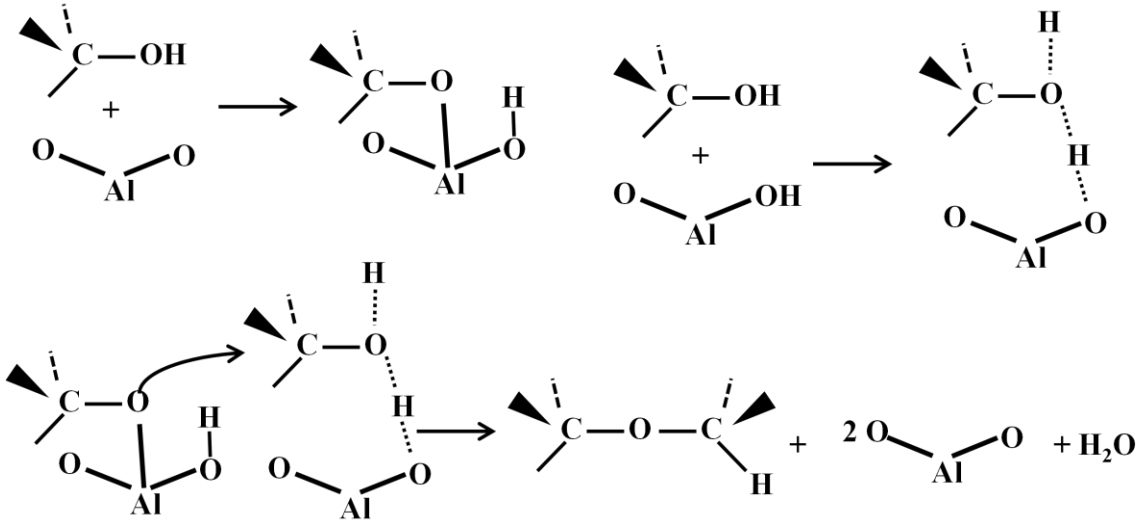

Figure 4.1.7. The mechanism for ether formation and olefin formation proposed by Shi and Davis. The mechanism was adapted from [42].

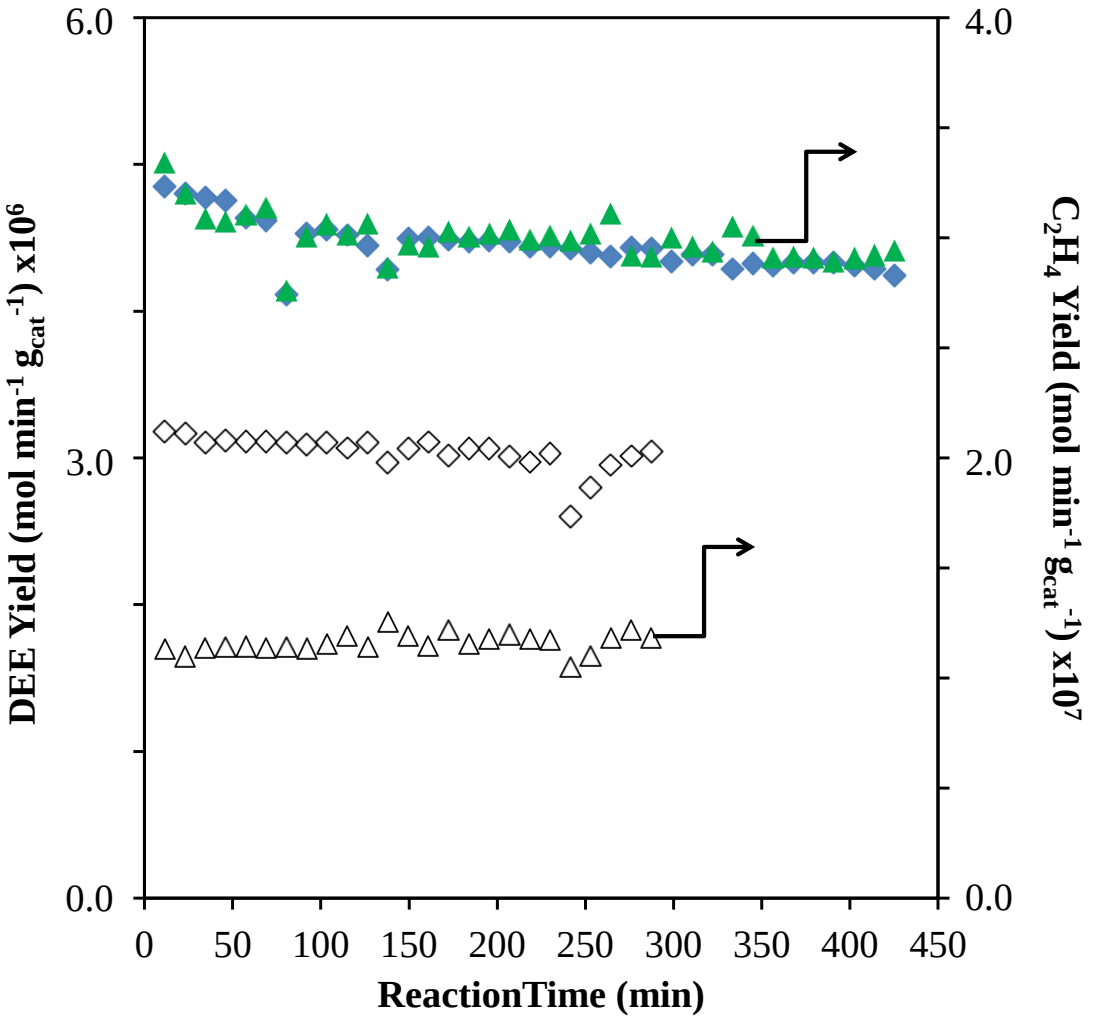

Figure 4.3.1. Measured DEE yield as a function of time on the γ-Al_2O_3 sample which was exposed to 2.2 kPa water for 1 h(◇) and on the sample without prior exposure to water (◆). Measured DEE yield as a function of time on the γ-Al_2O_3 sample which was exposed to 2.2 kPa water for 1 h(△) and on the sample without prior exposure to water (▲). pressure 0.8 kPa.

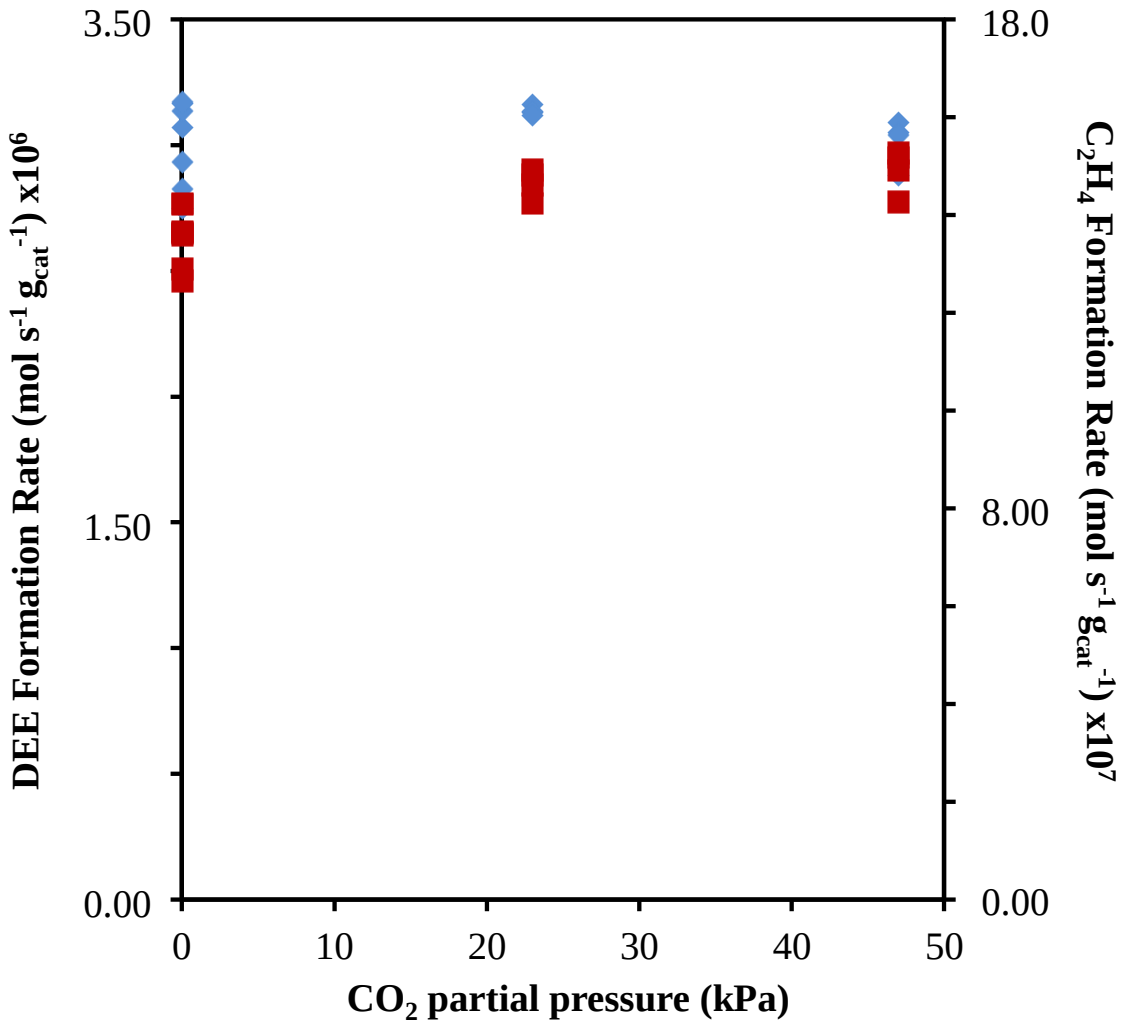

Figure 4.3.2. Measured rate of DEE (◆) and ethylene (■) formation as a function of CO_2 pressure for ethanol dehydration on γ-Al_2O_3 at 488 K under ethanol pressure 0.8 kPa.

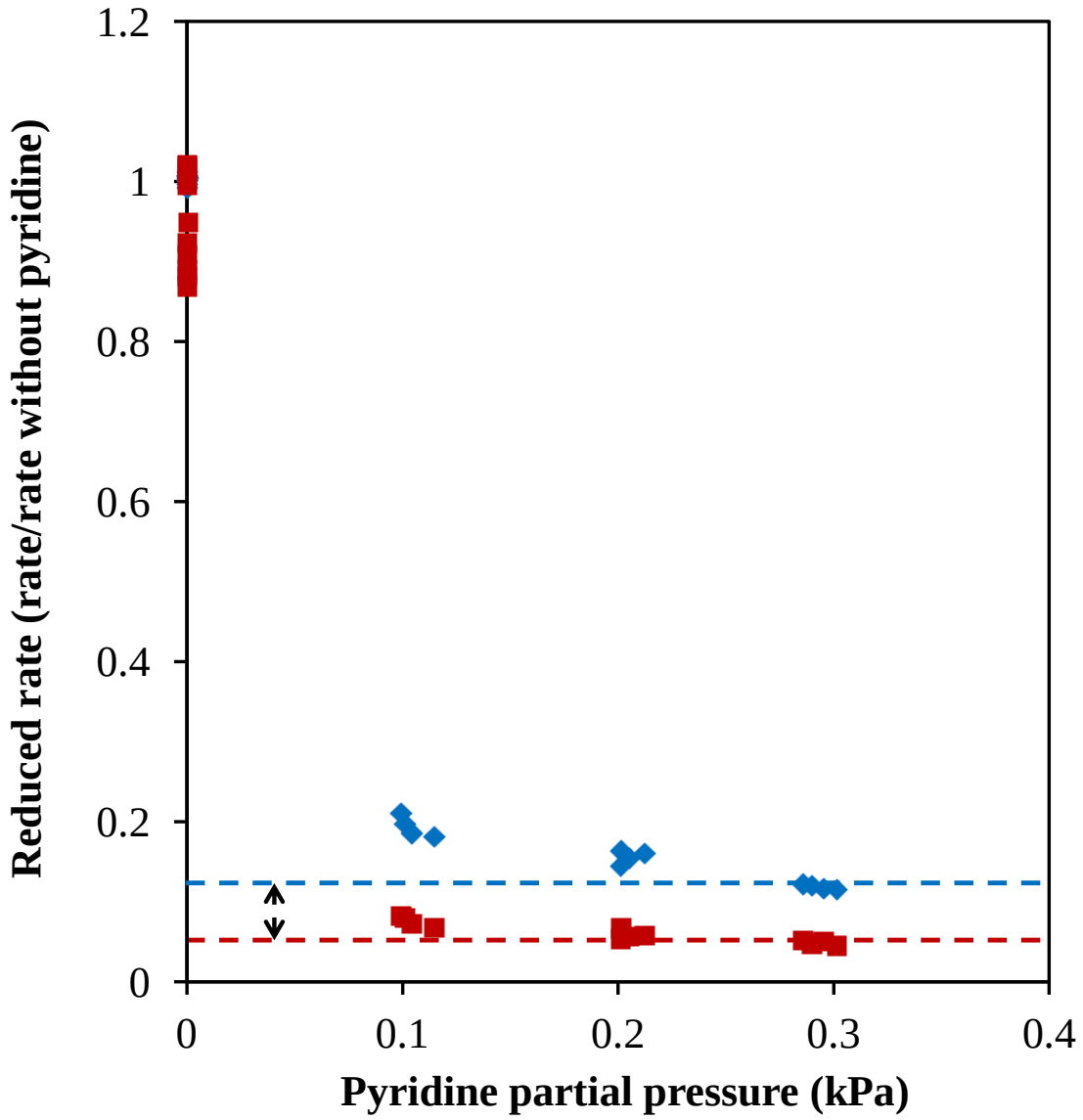

Figure 4.3.3. Measured rate of DEE (◆) and ethylene (■) formation as a function of pyridine pressure for ethanol dehydration on γ-Al_2O_3 at 488 K under ethanol pressure 0.9 kPa.

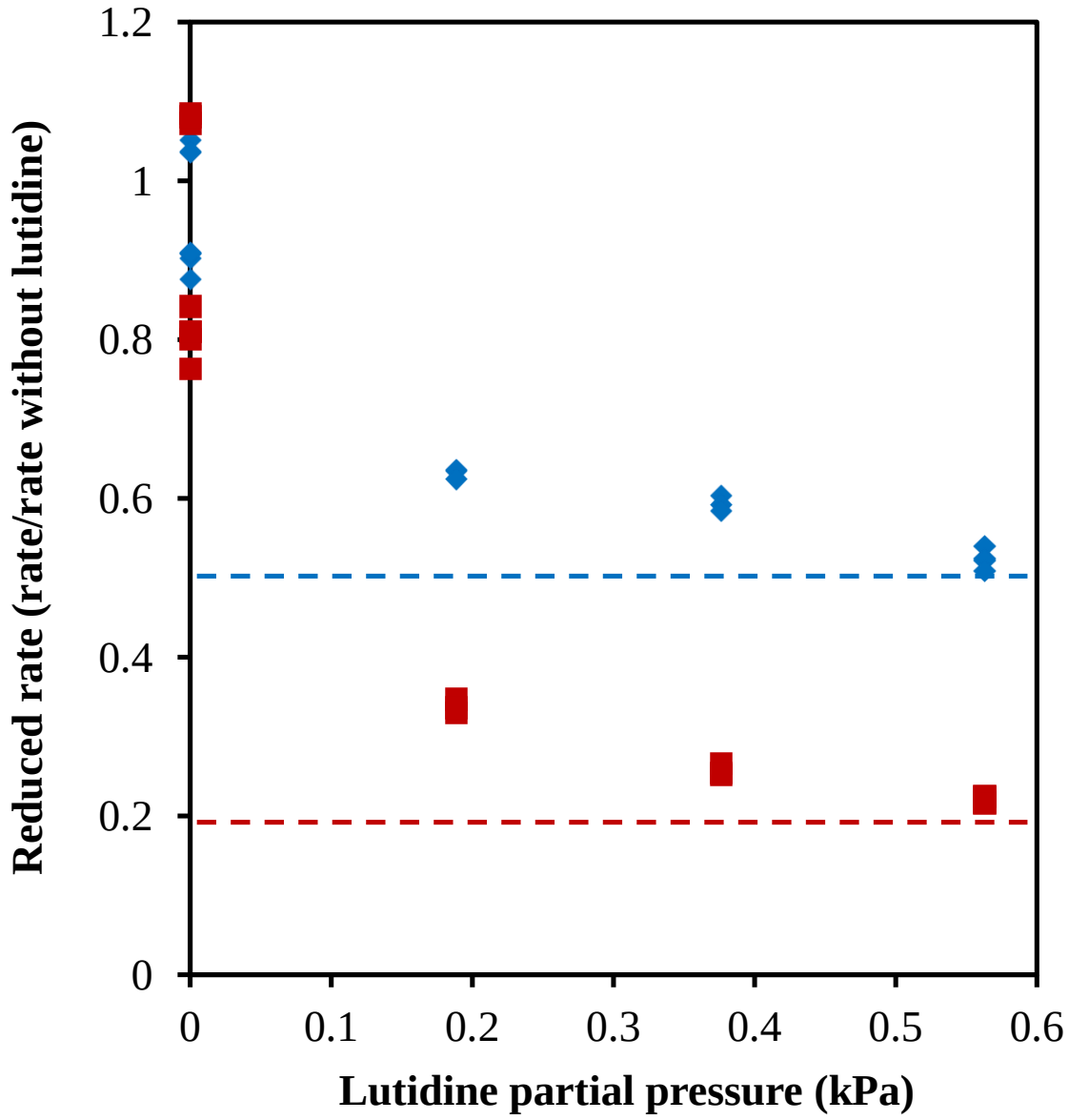

Figure 4.3.4. Measured rate of DEE (◆) and ethylene (■) formation as a function of lutidine pressure for ethanol dehydration on γ-Al_2O_3 at 488 K under ethanol pressure 0.9 kPa.

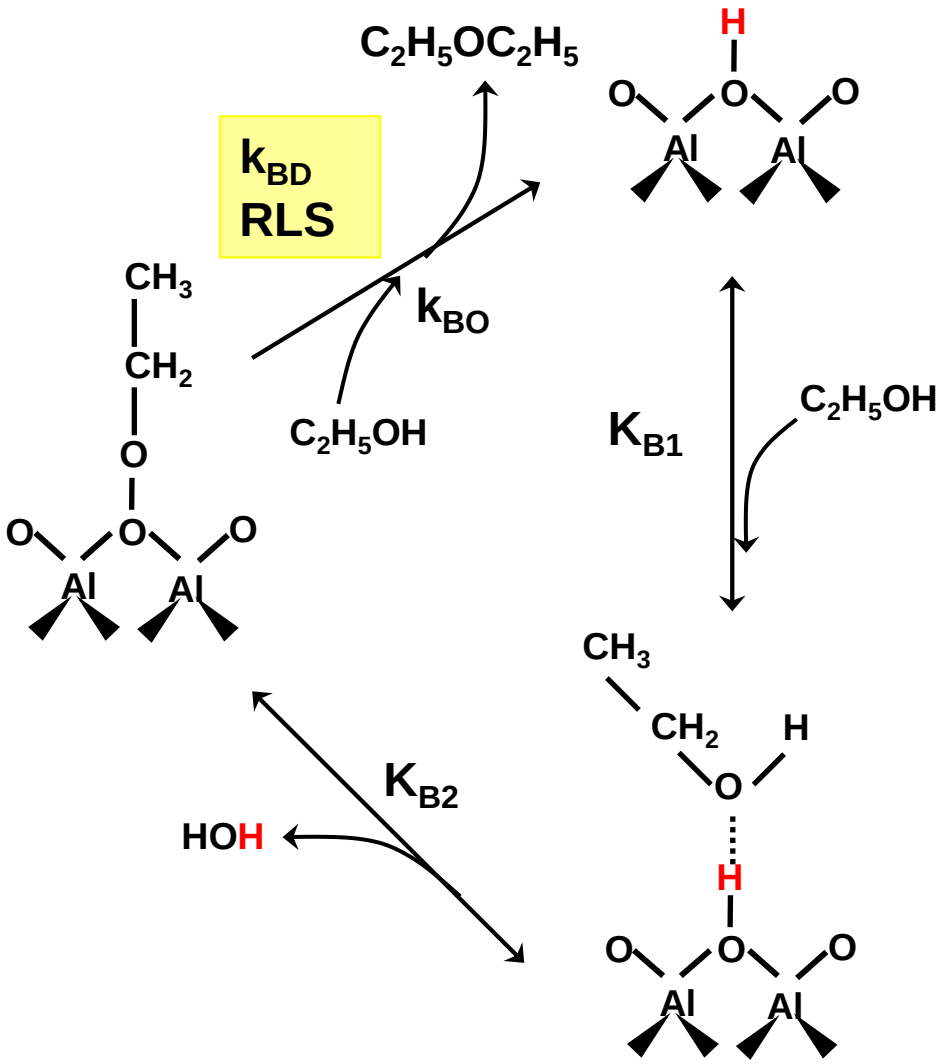

Figure 4.3.5. Possible elementary steps for ethanol dimerization into DEE via the reaction of a surface-bound ethoxide species and an ethanol molecule on γ-Al_2O_3.

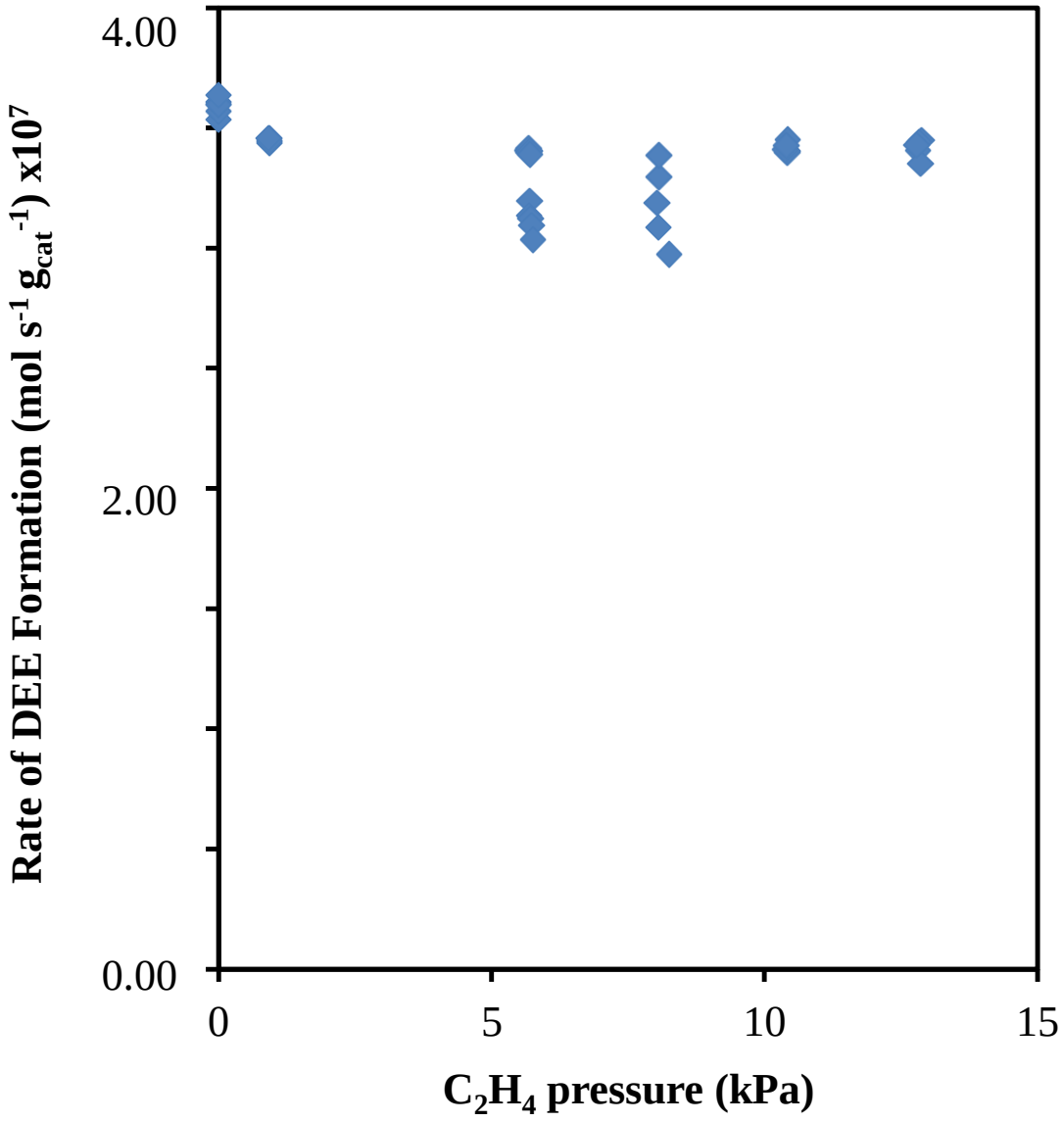

Figure 4.3.6. Measured rate of DEE formation as a function of ethylene pressure for ethanol dehydration on γ-Al_2O_3 at 458 K at ethanol pressure 1.6 kPa.

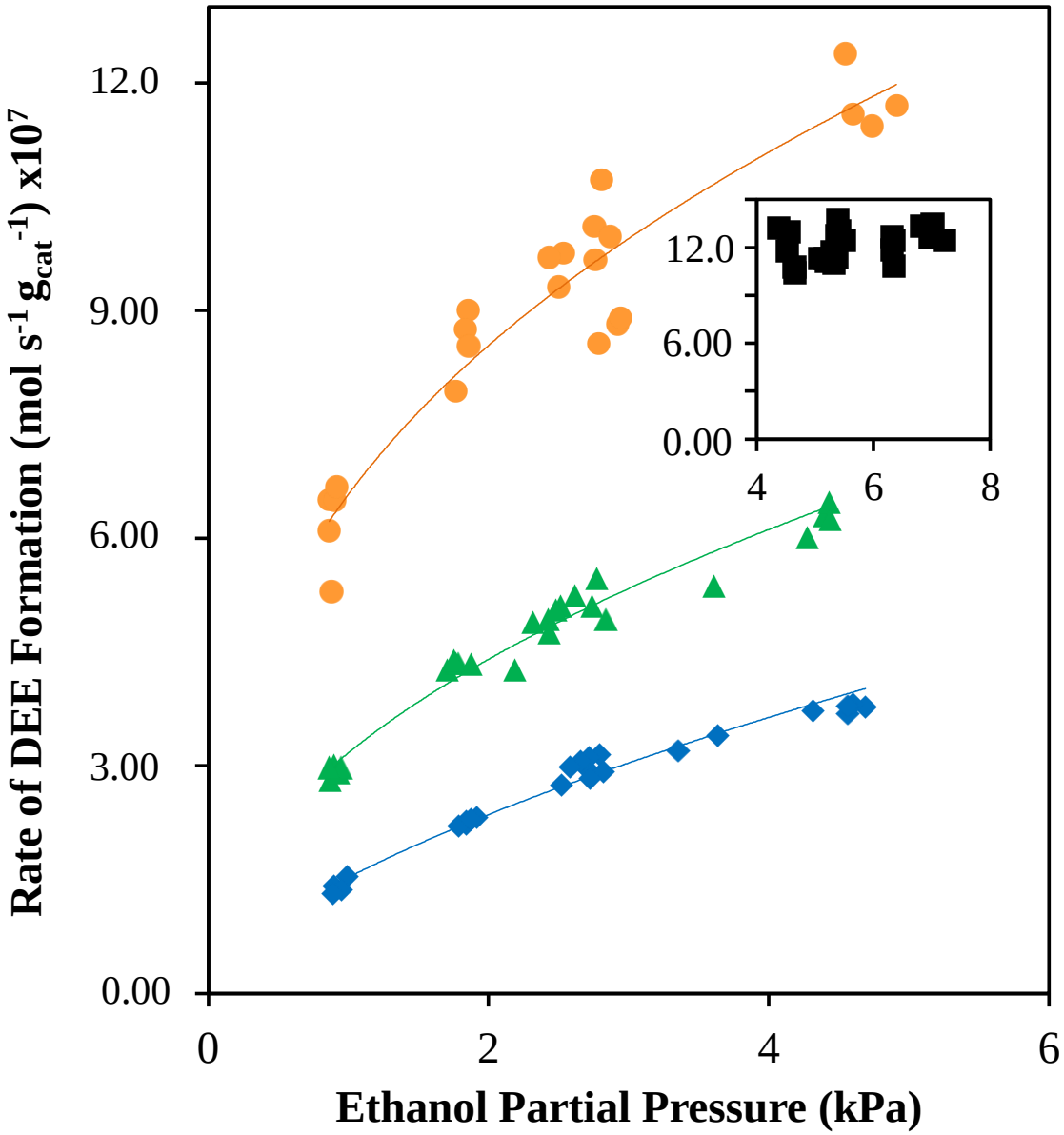

Figure 4.3.7. Measured rate of DEE formation for ethanol dehydration on γ-Al_2O_3 as a function of ethanol pressure at 488 K under water pressures 0.4 kPa (■),0.6 kPa (●), 1.2 kPa (▲), and 2.2 kPa(◆).

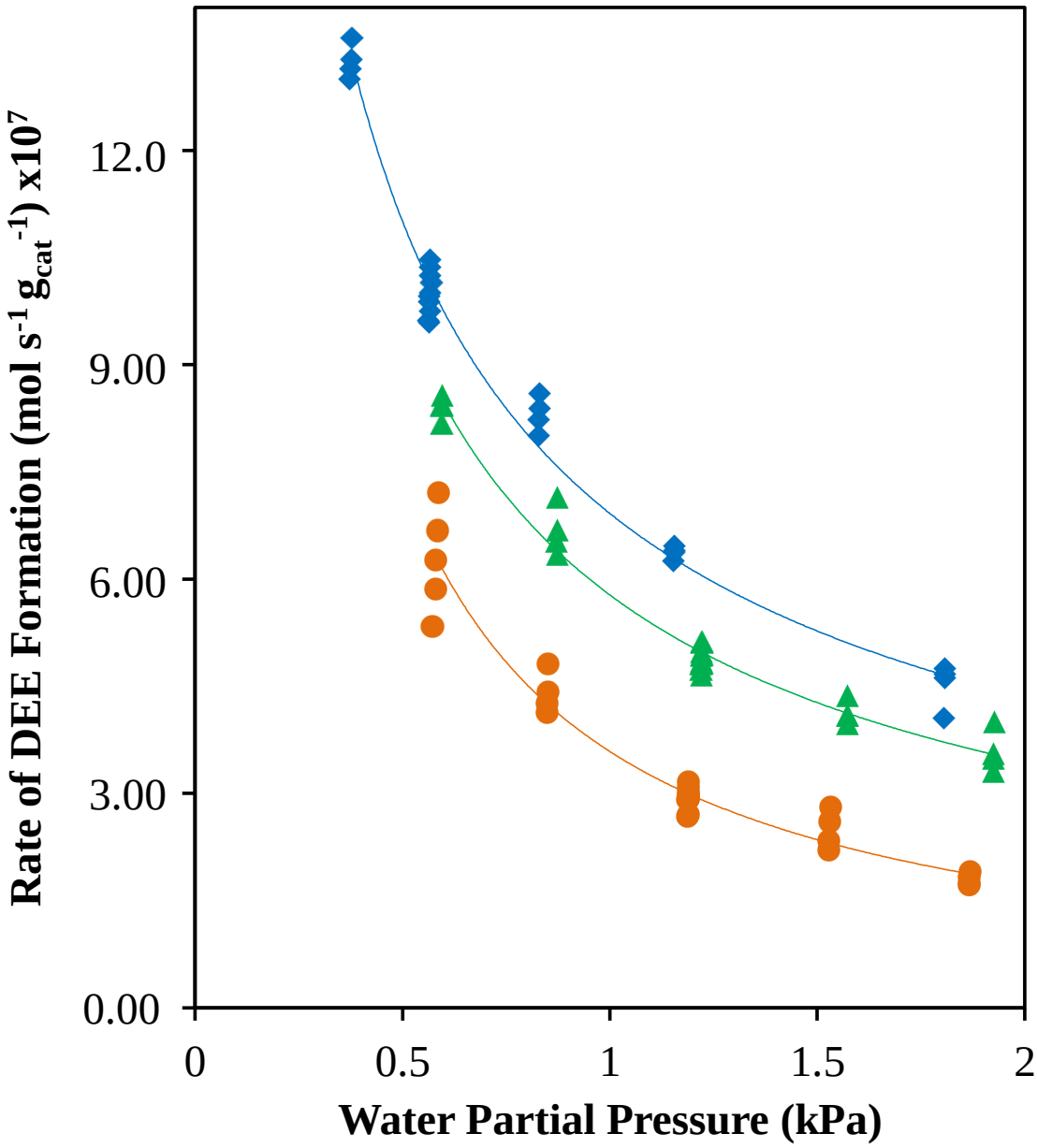

Figure 4.3.8. Measured rate of DEE formation for ethanol dehydration on γ-Al_2O_3 as a function of water pressure at 488 K under ethanol pressures 0.9 kPa (●), 2.9 kPa (▲) and 4.2 kPa(◆).

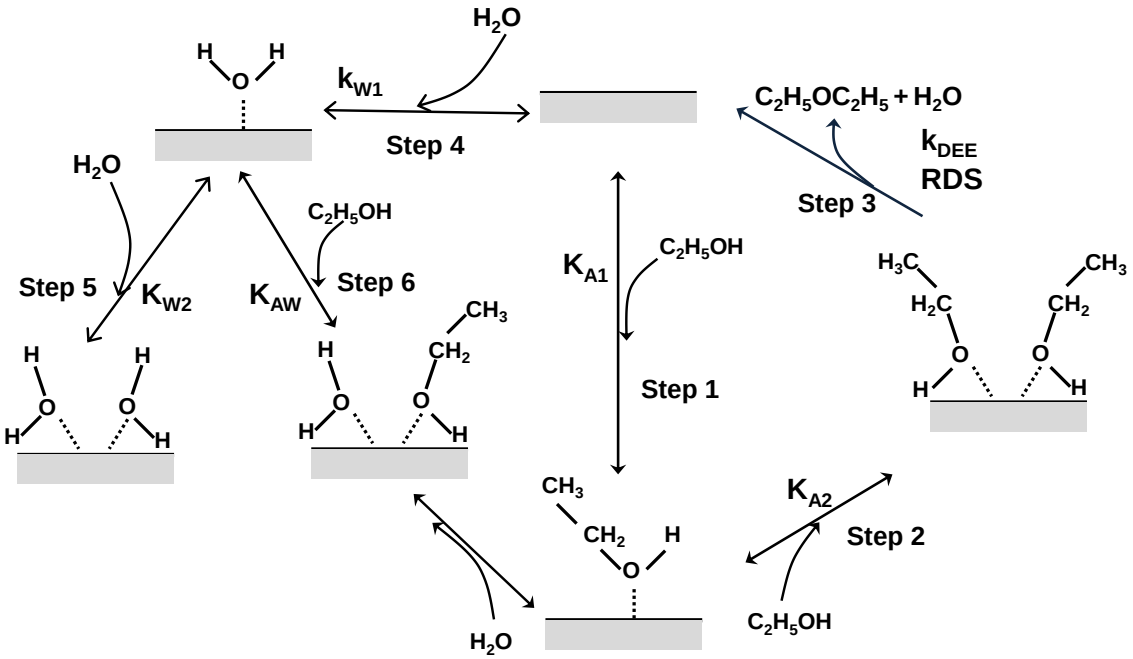

Figure 4.3.9. Proposed elementary steps for bimolecular dehydration of ethanol via the activation of ethanol dimer on γ-Al_2O_3.

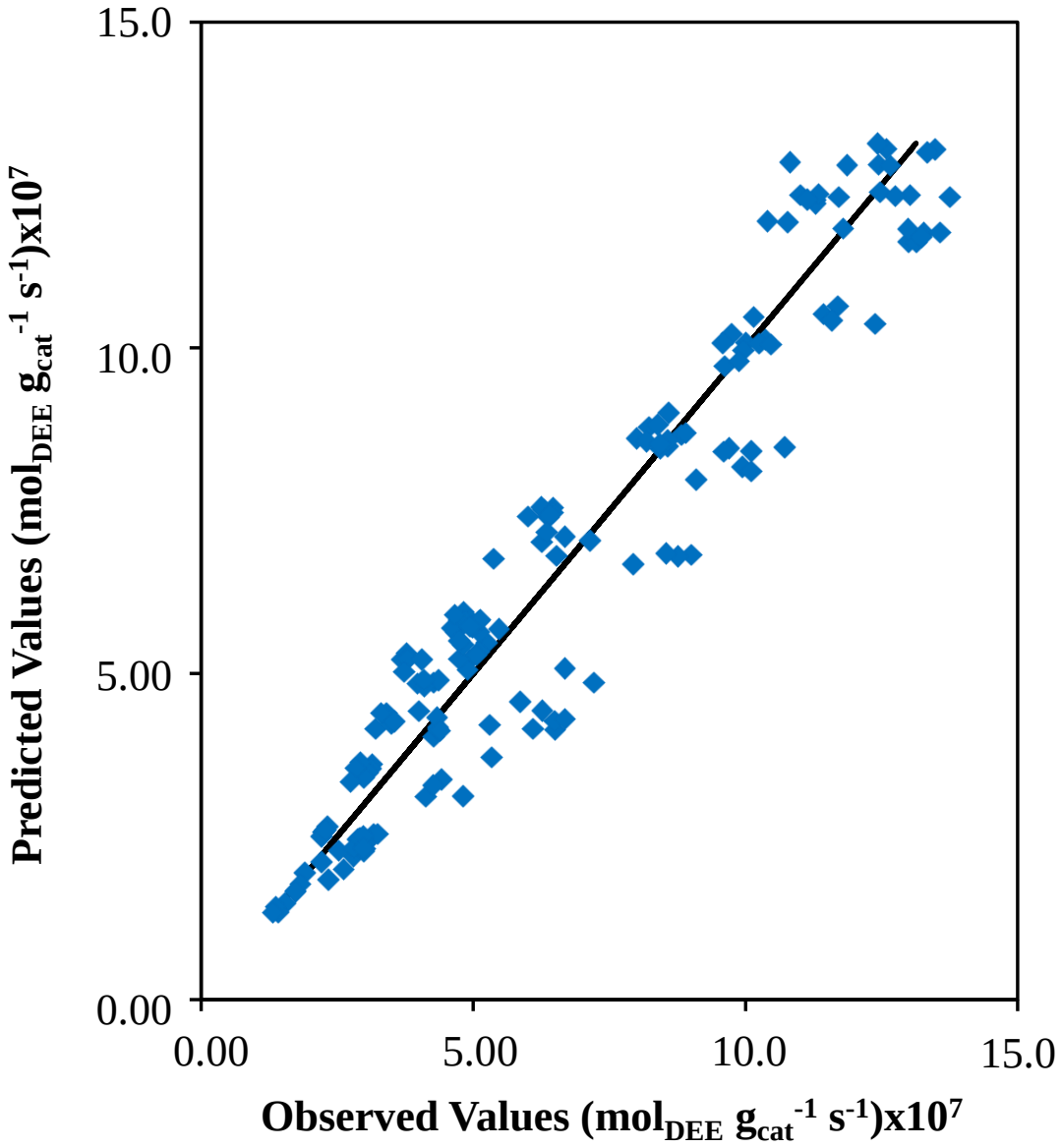

Figure 4.3.10. Predicted rate of DEE formation using equation 4.3.2 as a function of measured rate at 488 K.

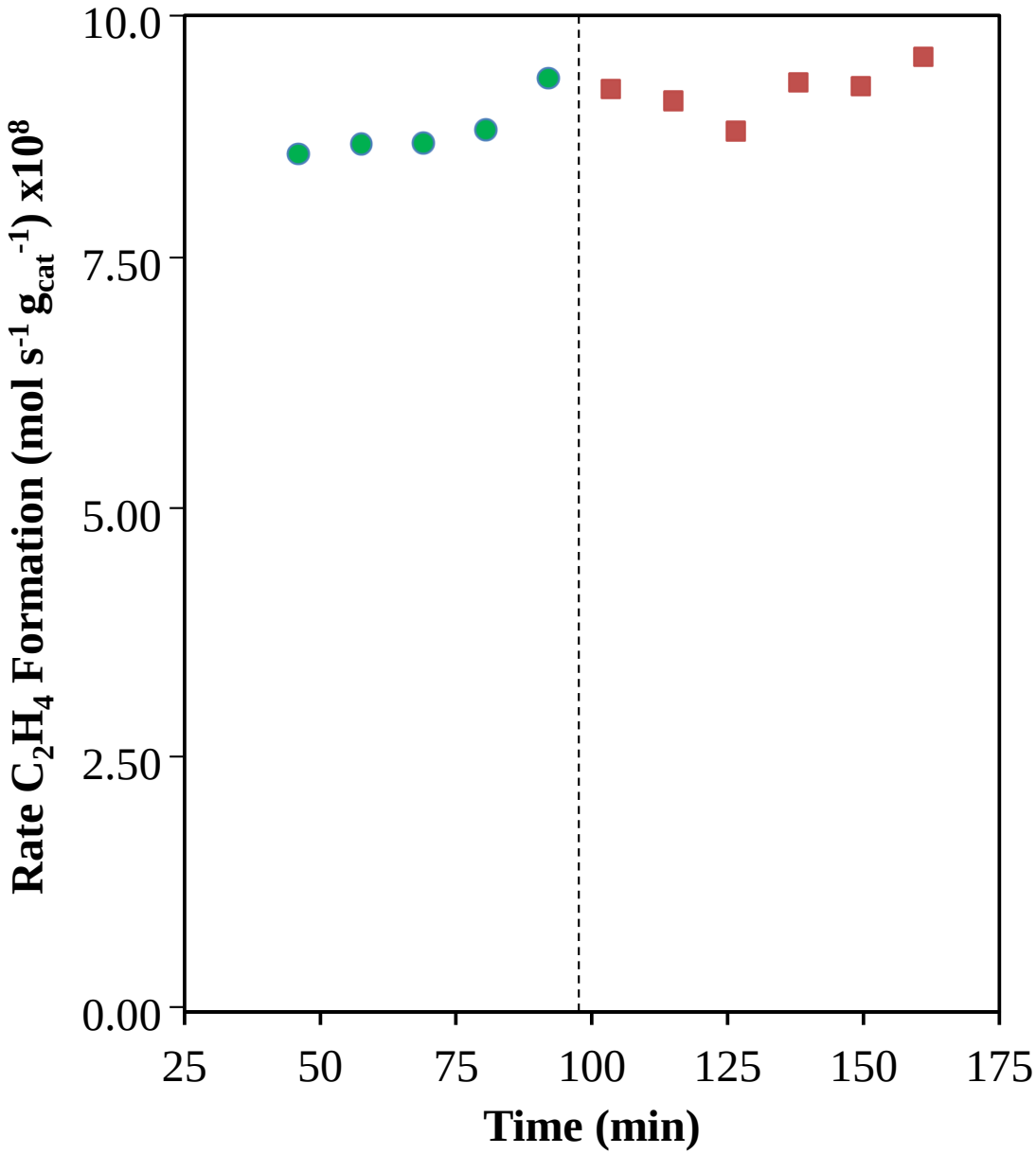

Figure 4.3.11. Measured rate of ethylene formation for ethanol dehydration on γ-Al_2O_3 as a function of time on stream at 488 K and ethanol pressure 1.6 kPa. (●) under DEE pressure 0.2 kPa and (■) under DEE pressure 0.04 kPa.

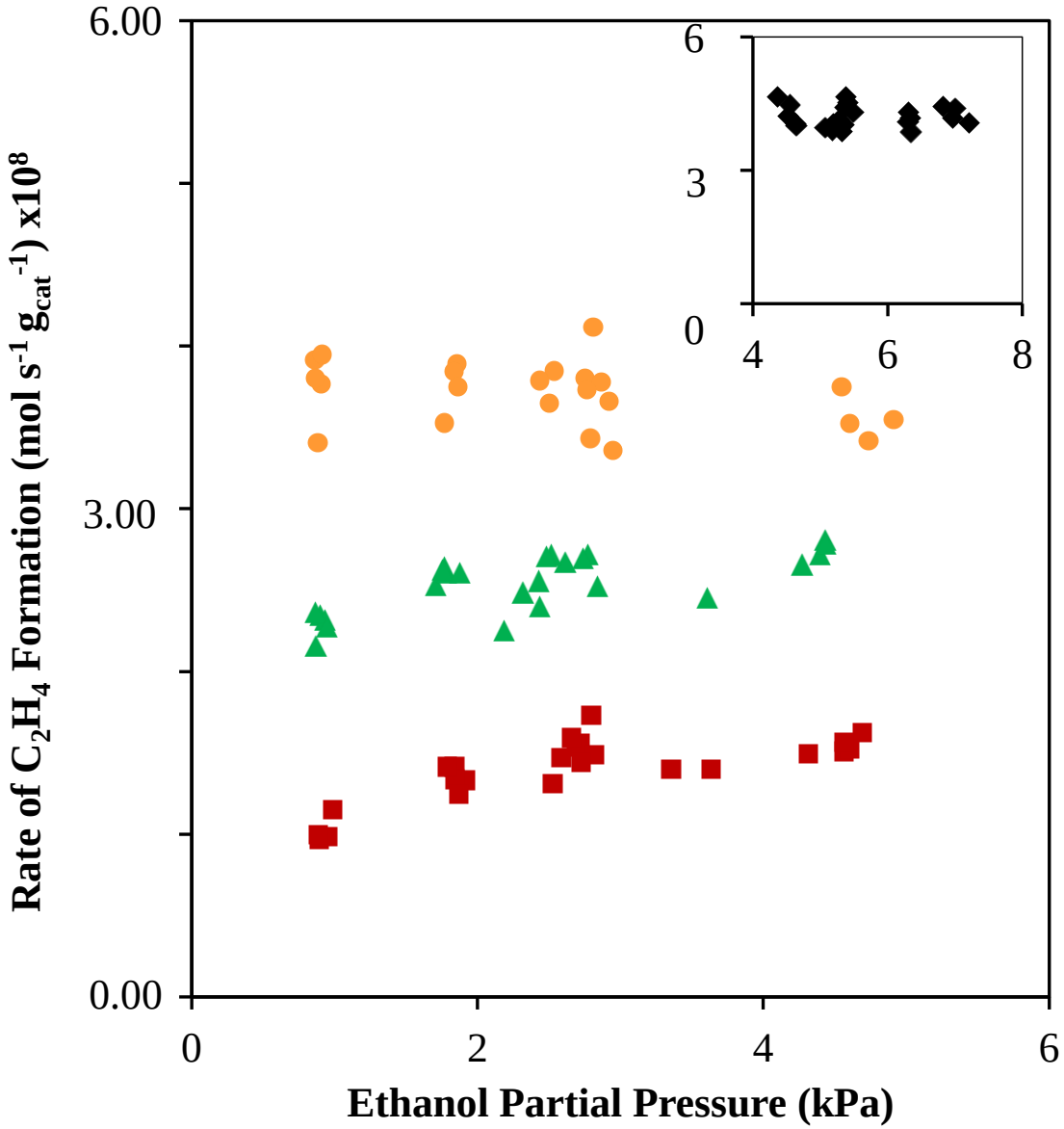

Figure 4.3.12. Measured rate of ethylene formation for ethanol dehydration on γ-Al_2O_3 as a function of ethanol pressure at 488 K under water pressures 0.4 (◆), 0.6 kPa (●), 1.2 kPa (▲), and 2.2 kPa(■).

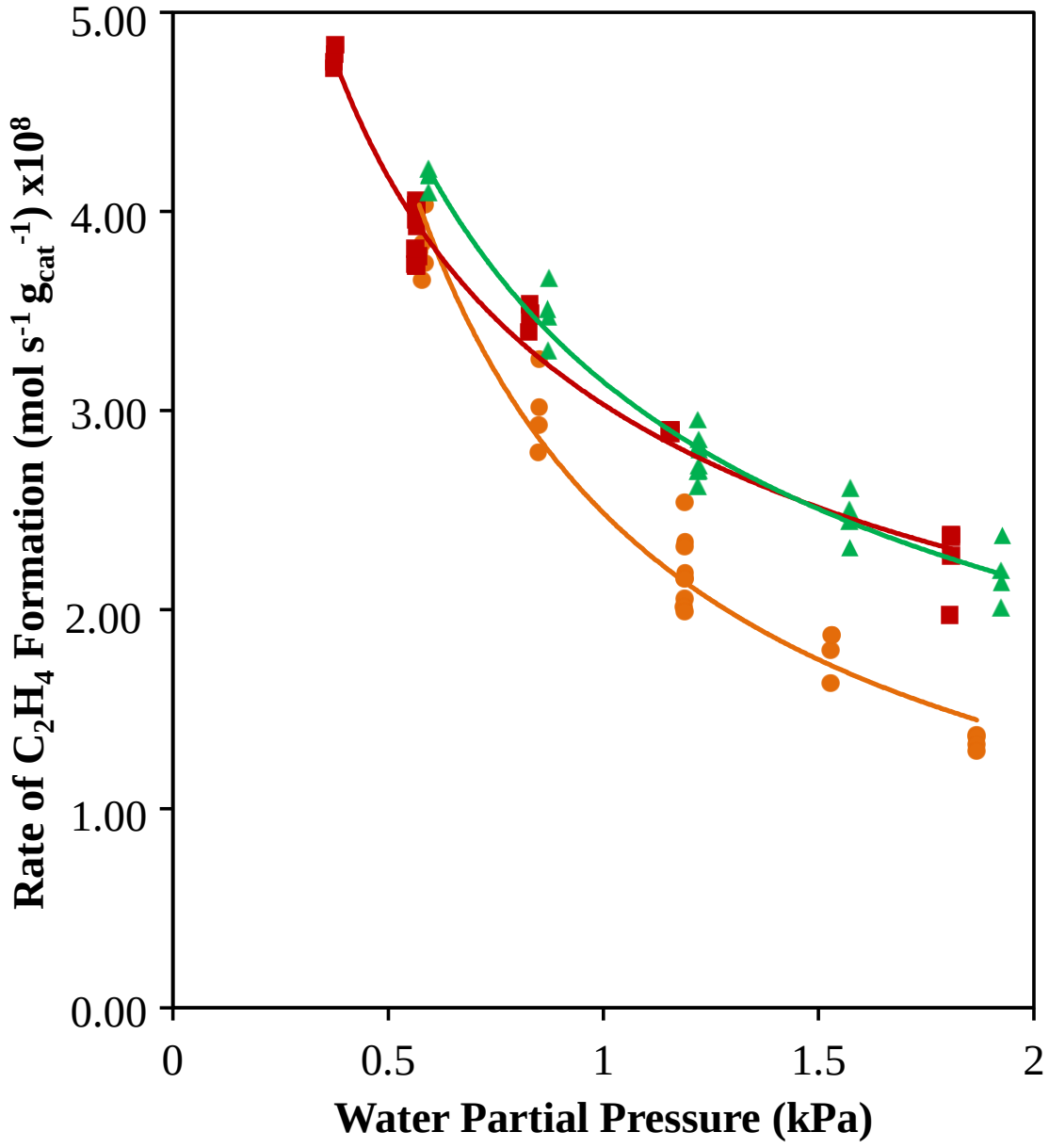

Figure 4.3.13. Measured rate of ethylene formation for ethanol dehydration on γ-Al_2O_3 as a function of water pressure at 488 K under ethanol pressures 0.9 kPa (●), 2.9 kPa (▲) and 4.2 kPa(■).

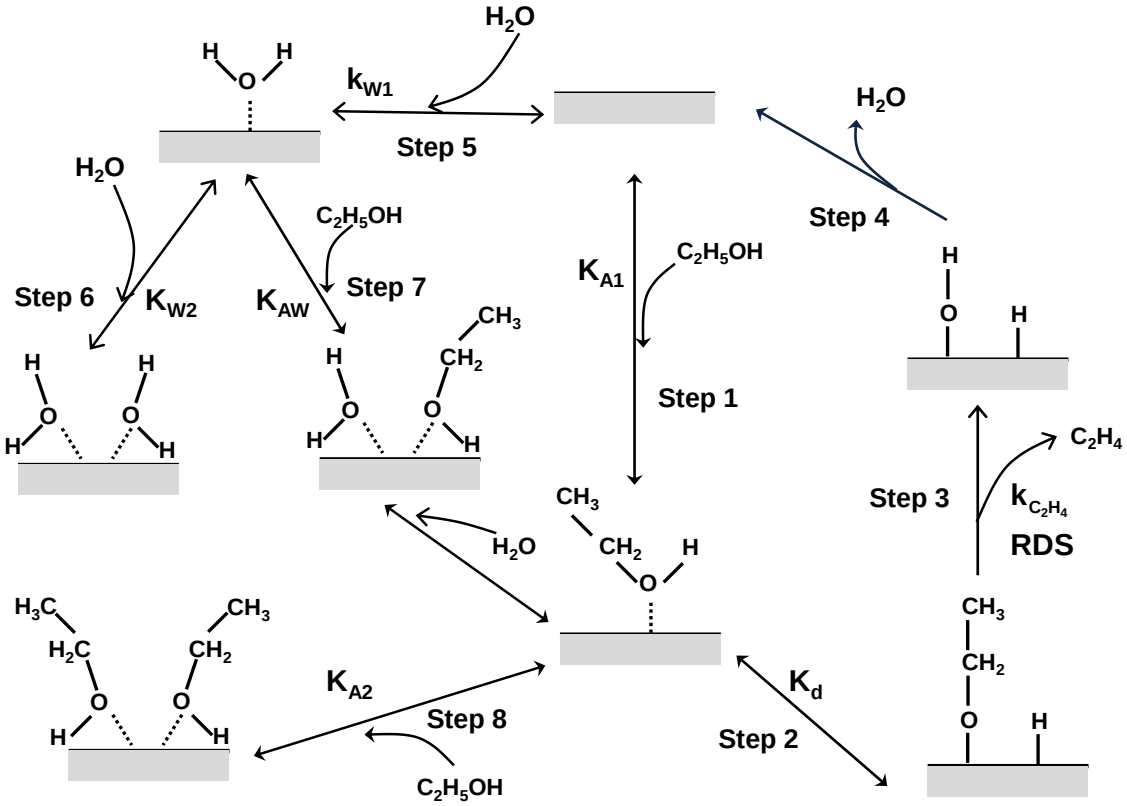

Figure 4.3.14. Proposed elementary steps for ethylene formation for ethanol dehydration via desorption of surface-bound ethoxide species on γ-Al_2O_3.

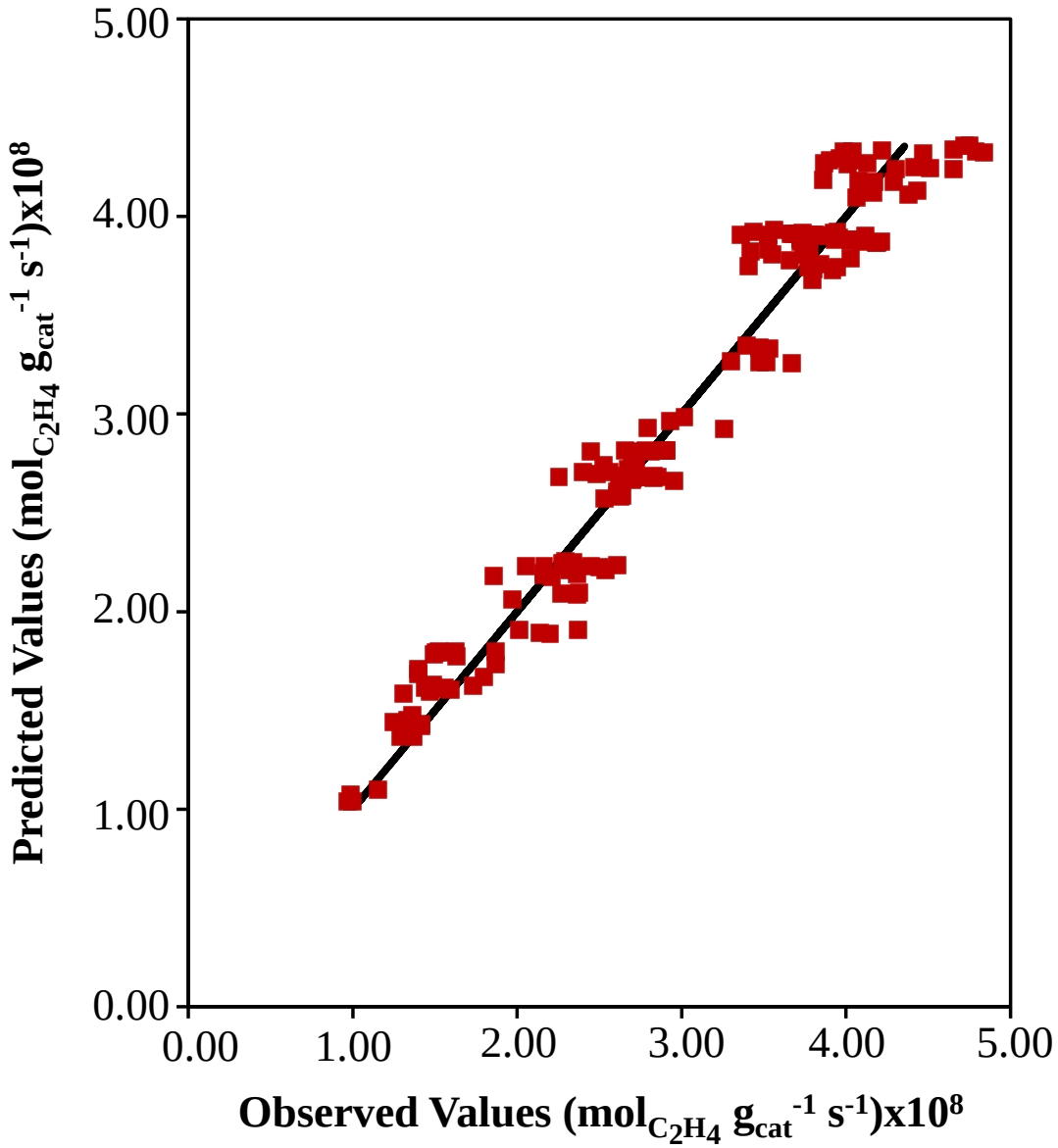

Figure 4.3.15. Predicted rate of ethylene formation using equation 4.3.4 as a function of measured rate at 488 K.

Table 4.1.1. The formation energy (∆E) and activation energy (ΔE^a) for cis-2-butene and trans-2-butene from the desorption of surface-bound 2-buthoxide from [46].

	van der Waals interaction	Product: Cis-2-butene	Product: Trans-2-butene
△E (k J mol-1)	no	42	36
	yes	60	63
$\triangle E^a$ (k J mol-1)	no	79	94
	yes	108	147

Table 4.3.1. The measured rate of DEE and ethylene formation from dehydration of C_2H_5OH and C_2D_5OD at ethanol pressure 1.0 kPa, water pressure 1.2 kPa, and temperature 488 K.

Reactant	C_2H_5OH	C_2D_5OD	DEE r_H/r_D	C_2H_4 r_H/r_D
Rate of DEE ($/10^{-7}$ mol $g^{-1}s^{-1}$)	2.99±0.38	2.97±0.13	1.01 ± 0.14	
Rate of C_2H_4 ($/10^{-8}$ mol $g^{-1}s^{-1}$)	2.44±0.12	1.01±0.06		2.42 ± 0.19

Table 4.3.2. The measured rate of DEE and ethylene formation from ethanol dehydration of C_2H_5OH and C_2D_5OD at ethanol pressure 1.3 kPa and temperature 488 K.

Reactant	C_2H_5OH	C_2H_5OD	DEE r_H/r_D	C_2H_4 r_H/r_D
Rate of DEE ($/10^{-6}$ mol $g^{-1}s^{-1}$)	2.49±0.29	2.56±0.09	0.97 ± 0.12	
Rate of C_2H_4 ($/10^{-8}$ mol $g^{-1}s^{-1}$)	1.18±0.18	1.32±0.06		0.89 ± 0.14

Table 4.3.3. Rate constant and ratio of adsorption equilibrium constants for bimolecular ethanol dehydration on γ-Al_2O_3 at 488 K.

Product	k_{DEE} ($/10^{-6}$ mol g^{-1} s^{-1})	$K_{W1}K_{AW}/K_{A1}K_{A2}$
DEE	1.60±0.08	4.28±0.47

Table 4.3.4. Rate constant and ratio of adsorption equilibrium constants for unimolecular ethanol dehydration on γ-Al_2O_3 at 488 K.

Product	$k_{C2H4}K_d$ ($/10^{-8}$ mol g^{-1} s^{-1})	$K_{W1}K_{AW}/K_{A1}$ (1/kPa)	K_{A2} (1/kPa)	$K_{W1}K_{W2}/K_{A1}$ (1/kPa)
Ethylene	6.45±0.5	0.831±0.147	0.036 ± 0.015	0.567± 0.105

Supplementary Information for Chapter 2

S.2.1. Derivation of the Rate Equation for DEE Synthesis via the Dimer-mediated Mechanism

Assuming that the rate-limiting step is the dehydration of an ethanol dimer (Step 3, Figure 2.3.5), the rate equation for dimerization of two co-adsorbed ethanol monomers is expressed as equation S.2.1.1.

$$r_{C_2H_5OC_2H_5} = k_5[\text{dimer}] \qquad \text{(S.2.1.1)}$$

where k_5 is the intrinsic rate constant for the dimerization step and [dimer] is the number of ethanol dimers adsorbed on the zeolite surface.

The quasi-equilibrium assumption is applied for ethanol adsorption (Step 1, Figure 2.3.5) and for ethanol dimer formation (Step 2, Figure 2.3.5) with equilibrium constants K_1 and K_4, respectively. Therefore, the number of ethanol monomers and dimers can be expressed in terms of gas phase ethanol concentration as shown in equations S.2.1.2 and S.2.1.3.

$$[\text{monomer}] = K_1[H^+][C_2H_5OH] \qquad \text{(S.2.1.2)}$$

$$[\text{dimer}] = K_4[\text{monomer}][C_2H_5OH] = K_1K_4[H^+][C_2H_5OH]^2 \qquad \text{(S.2.1.3)}$$

where $[C_2H_5OH]$ is the ethanol pressure in gas phase, $[H^+]$ is the number of accessible Brønsted acid sites, and [monomer] and [dimer] reperesent the number of ethanol monomers and dimers absorbed on the zeolite surface, respectively. Based on the assumption that ethanol monomers and ethanol dimers are the most abundant surface

*Reported from H. Chiang, and A. Bhan, Journal of Catalysis 271 (2010) 251-261 © 2010 Elsevier Inc.

intermediates on the zeolite, the balance of surface species can be expressed as equation S.2.1.4.

$$[H^+]_0 = K_1[H^+][C_2H_5OH] + K_1K_4[H^+][C_2H_5OH]^2 \quad \text{(S.2.1.4)}$$

where $[H^+]_0$ is the number of initially accessible Brønsted acid sites.

The combination of equations S.2.1.1-2.1.4 results in the rate expression for diethyl ether formation shown in equation S.2.1.5.

$$\frac{r_{C_2H_5OC_2H_5}}{[H^+]_0} = \frac{k_5K_4[C_2H_5OH]}{1+K_4[C_2H_5OH]} \quad \text{(S.2.1.5)}$$

The rearrangement of equation S.2.1.5 leads to equation S.2.1.6.

$$\frac{[C_2H_5OH][H^+]_0}{r_{C_2H_5OC_2H_5}} = \frac{1}{k_5K_4} + \frac{[C_2H_5OH]}{k_5} \quad \text{(S.2.1.6)}$$

S.2.2. Derivation of the Rate Equation for DEE Synthesis via the Ethoxide-mediated Mechanism

The rate law for the ethoxide-mediated mechanism shown in Figure 2.3.6 can be expressed as equation S.2.2.1 because the rate-limiting step is the reaction of surface-bound ethoxide species with ethanol (Step 3, Figure 2.3.6).

$$r_{C_2H_5OC_2H_5} = k_3[C_2H_5OH][\text{ethoxide}] \quad \text{(S.2.2.1)}$$

where k_3 is the intrinsic rate constant for the reaction of surface-bound ethoxide species with ethanol, and [ethoxide] represents the number of surface-bound ethoxide species on the zeolite surface.

Based on the assumption that the zeolite surface is mainly occupied by ethanol monomers and ethanol dimers, the rate expression can be expressed as equation S.2.2.2.

$$\frac{r_{C_2H_5OC_2H_5}}{[H^+]_0} = \frac{k_3K_1K_2\dfrac{[C_2H_5OH]^2}{[H_2O]}}{K_1[C_2H_5OH]+K_1K_4[C_2H_5OH]^2} = \frac{k_3K_2[C_2H_5OH]}{[H_2O]+K_4[H_2O][C_2H_5OH]} \quad (S.2.2.2)$$

where K_2 is the equilibrium constant for the decomposition of ethanol into water and surface-bound ethoxide species, and $[H_2O]$ is the partial pressure of water in gas phase.

S.3. Derivation of the Rate Equation for DEE Synthesis from the Reactions of Ethanol and Ethylene

There are two plausible catalytic cycles for DEE formation from the reaction of co-adsorbed ethanol and ethylene. One is the ethoxide-mediated mechanism, and the other is from the dehydration of ethanol dimers and from co-absorbed ethanol and ethylene complexes.

If diethyl ether (DEE) formation is through the ethoxide-mediated mechanism (Figure 2.3.6), the assumption that ethylene adsorption to form ethoxide species is in quasi-equilibrium implies equation S.2.2.1 can be written as shown in equation S.2.3.1, when the reactants are ethanol and ethylene.

$$r_{C_2H_5OC_2H_5} = k_3K_e[C_2H_5OH][C_2H_4][H^+] \quad (S.2.3.1)$$

where $[C_2H_4]$ is the partial pressure of ethylene in gas phase.

The assumption that the zeolite surface is mainly occupied by ethanol monomeric species and ethanol dimeric species leads to equation S.2.3.2.

$$\frac{r_{C_2H_5OC_2H_5}}{[H^+]_0} = \frac{k_3K_e[C_2H_5OH][C_2H_4]}{K_1[C_2H_5OH]+K_1K_4[C_2H_5OH]^2} = \frac{k_3K_e[C_2H_4]}{K_1+K_1K_4[C_2H_5OH]} \quad (S.2.3.2)$$

If DEE formation is from the dehydration of ethanol dimeric species and from the activation of co-absorbed ethanol and ethylene complexes, the rate expression is comprised of two terms. The first term represents the contribution from the dimer-

mediated mechanism (Figure 2.3.5). Therefore, the first term in equation S.2.3.6 is the same as equation S.2.1.5. The second term represents the contribution from the activation of the co-adsorbed ethylene and ethanol complexes to produce DEE.

The second term is expressed as equation S.2.3.3 based on the assumption that the rate-limiting step is the activation of co-adsorbed ethylene and ethanol to produce DEE.

$$\text{Second term} = k_{ee}[C_2H_4 * C_2H_5OH] \qquad \text{(S.2.3.3)}$$

where k_{ee} is the intrinsic rate constant for activation of co-adsorbed ethanol and ethylene complexes and $[C_2H_4*C_2H_5OH\ ]$ is the number of co-adsorbed ethanol and ethylene complexes.

By applying the quasi-equilibrium assumption to the formation of co-adsorbed ethanol and ethylene complexes, $[C_2H_4*C_2H_5OH]$ can be expressed in terms of the pressure of ethanol and ethylene in gas phase as shown in equation S.2.3.4.

$$[C_2H_4 * C_2H_5OH] = K_{co}[\text{monomer}][C_2H_4] = K_{co}K_1[C_2H_5OH][C_2H_4][H^+] \qquad \text{(S.2.3.4)}$$

where K_{co} is the equilibrium constant for an ethanol monomer interacting with ethylene to form a co-absorbed ethanol and ethylene complex.

Based on the assumption that the zeolite surface is mainly occupied by ethanol monomeric and dimeric species, the rate law for DEE synthesis via activation of the co-absorbed ethanol and ethylene complexes is expressed as equation S.2.3.5.

$$\text{Second term} = \frac{k_{ee}K_{co}K_1[C_2H_5OH][C_2H_4][H^+]_0}{K_1[C_2H_5OH] + K_1K_4[C_2H_5OH]^2} = \frac{k_{ee}K_{co}[C_2H_4][H^+]_0}{1 + K_4[C_2H_5OH]} \qquad \text{(S.2.3.5)}$$

Therefore, combining equations S.2.1.5 and S.2.3.5, equation S.2.3.6 represents the rate law for DEE synthesis via the dehydration of ethanol dimeric species and concurrently via the activation of co-absorbed ethanol and ethylene complexes.

$$\frac{r_{C_2H_5OC_2H_5}}{[H^+]_0} = \frac{k_5 K_4 [C_2H_5OH]}{1 + K_4 [C_2H_5OH]} + \frac{k_{ee} K_{co} [C_2H_4]}{1 + K_4 [C_2H_5OH]} \quad \text{(S.2.3.6)}$$

S.2.4. Derivation for the Rate Equations of Ethylene Synthesis over H-MOR

According to Figure 2.3.13, the rate equation for ethylene synthesis within 8-MR channels in H-MOR is expressed as shown in equation S.2.4.1.

$$r_{C_2H_4} = k_{2,8MR} [\text{monomer}]_{8MR} \quad \text{(S.2.4.1)}$$

where $k_{2,8MR}$ is the intrinsic rate constant of water elimination to form surface-bound ethoxide species (step2 in Figure 2.3.13) and $[\text{monomer}]_{8MR}$ is number of ethanol monomers adsorbed within the 8-MR side pockets in the MOR-type zeolite. Assuming that ethanol monomer formation achieves quasi-equilibrium with an equilibrium constant $K_{1,8MR}$, we can relate the number of adsorbed ethanol monomers to the gas phase pressure of ethanol as shown in equation S.2.4.2.

$$[\text{monomer}]_{8MR} = K_{1,8MR} [H^+]_{8MR} [C_2H_5OH] \quad \text{(S.2.4.2)}$$

where $[H^+]_{8MR}$ is the number of unoccupied Brønsted sites within 8-MR channels.

The assumption that nearly all the Brønsted sites are occupied by ethanol monomers within the 8-MR channels leads to the rate expression shown in equation S.2.4.3.

$$r_{C_2H_4,8MR} = \frac{[H^+]_{0,8MR} k_{2,8MR} K_{1,8MR} [C_2H_5OH]}{K_{1,8MR} [C_2H_5OH]} = k_{2,8MR} [H^+]_{0,8MR} \quad \text{(S.2.4.3)}$$

According to Figure 2.3.14, the rate equation for ethylene synthesis in 12-MR channels of H-MOR is expressed as equation S.2.4.4.

$$r_{C_2H_4,12MR} = k_{2,12MR} [\text{monomer}]_{12MR} \quad \text{(S.2.4.4)}$$

where $k_{2,12MR}$ is the intrinsic rate constant for water elimination to form surface-bound ethoxide species (Step 2, Figure 2.3.14) and $[\text{monomer}]_{12MR}$ is the number of ethanol

monomers within the 12-MR channels in MOR-type zeolites. The assumption that the most abundant surface species are ethanol monomers and ethanol dimers leads to equation S.2.4.5.

$$r_{C_2H_4,12MR} = \frac{k_{2,12MR}[H^+]_{0,12MR}}{1+K_{4,12MR}[C_2H_5OH]} \quad \text{(S.2.4.5)}$$

where $[H^+]_{0,12MR}$ is the total number of initially accessible Brønsted acid sites within 12-MR channels in MOR-type zeolites.

The number of initial Brønsted acid sites in MOR-type zeolites can be expressed as equation S.2.4.6.

$$[H^+]_0 = x_{8MR}[H^+]_0 + x_{12MR}[H^+]_{0,12MR} \quad \text{(S.2.4.6)}$$

where x_{12MR} and x_{8MR} are the fraction of Brønsted acid sites in the 12-MR and the 8-MR channels, respectively; $[H^+]_0$ is the total number of initial Brønsted acid sites in H-MOR.

The rate of ethylene synthesis in H-MOR is equal to the sum of the rate within 8-MR channels and within 12-MR channels. Therefore, the rate of ethylene synthesis in MOR-type materials is expressed as equation S.2.4.7.

$$\frac{r_{C_2H_4}}{[H^+]_0} = \frac{x_{12MR}k_{2,12MR}}{1+K_{4,12MR}[C_2H_5OH]} + x_{8MR}k_{2,8MR} \quad \text{(S.2.4.7)}$$

S.2.5. Estimation of Kinetic Isotopic Effects on Ethanol Dehydration Reactions to Produce Ethylene

The effects of isotopic labeling on reaction rates are termed as kinetic isotope effects (KIE) and the KIE value is defined as following [146].

$$\text{KIE value} = \frac{k_{2,H}}{k_{2,D}} \quad \text{(S.2.5.1)}$$

where $k_{2,H}$ is the rate constant for the reaction with no deuterium atoms in the reactants, and $k_{2,D}$ is the rate constant for reaction with deuterium atoms in the reactants. Based on Lowry and Richardson [146], for a rate-limiting step involving the cleavage of C-H or O-H bonds, the KIE value can be estimated by the following equation

$$\text{KIE value} = \frac{k_{2,H}}{k_{2,D}} = \exp\left(\frac{0.1865}{T}\upsilon_H\right) \qquad \text{(S.2.5.2)}$$

where T is the absolute temperature and υ_H is the vibrational frequency of the C-H or O-H bond (unit: cm^{-1}). The C-H bond stretching frequency is ~2985 cm^{-1} [15] and the vibrational frequency for O-H bond stretching is ~3612 cm^{-1} [15], implying the estimated KIE value involving the cleavage of a C-H bond is 4.2 at 388 K and the KIE value predicted for a rate-limiting step that involves cleavage of an O-H bond is 5.7 at 388 K.
For a rate-limiting step involving the re-hybridization of α carbon from sp^3 to sp^2 hybridization in the transition state, the KIE value can be estimated by the following equation [146].

$$\text{KIE value} = \frac{k_{2,H}}{k_{2,D}} = \exp\left(-\frac{0.1865}{T}(\upsilon^{\#} - \upsilon^{R})\right) \qquad \text{(S.2.5.3)}$$

where $\upsilon^{\#}$ is the vibrational frequncy of an C_α-H bond of the transition state and the υ^R is the vibrational frequncy of the corresponding C_α-H bond of the reactant molecules. For a transition state with sp^3 hybridization on the α carbon and a reactant with sp^2 hybridization on α carbon, the $\upsilon^{\#}$ is ~800cm^{-1} and the υ^R is ~1350 cm^{-1} [146], so the estimated KIE value is 1.3.

Supplementary Information for Chapter 3

S.3.1. Infrared measurements for O-H groups in 8-MR and 12-MR channels

H-MOR (30mg) was compressed as a thin pellet and was held in a quartz cell with NaCl windows. The pellet was treated in He (1.67 cm^3 s^{-1} at NTP condition, Minneapolis oxygen) at 773 K for 2h (0.0167 K s^{-1}), and cooled to ambient temperatures (298-303K) before infrared (IR) measurements. N_2 flow (~1.0 cm^3 s^{-1}, Valley National gases) was maintained overnight in the chamber of the IR spectrometer (Nicolet 6700 FTIR spectrometer, Thermo Scientific, Hg-Cd-Te (MCT) detector) before and also during the IR measurement to remove CO_2. Each IR spectrum was obtained by averaging 32 scans (4 cm^{-1} resolution, 4000-1300 cm^{-1} region) at ambient temperature. The IR bands corresponding to OH groups in H-MOR were deconvoluted and fitted using Gaussian band shapes for each of the bands using Origin 6.0. The IR spectra and the deconvolution of the spectral bands corresponding to OH groups in 8-MR and 12-MR channels are shown in Figure S.3.1.1 and reported in Table S.3.1.1.

S.3.2. Chemical Titration by Dimethyl Ether over Zeolites

Chemical titration using dimethyl ether (DME) over H-FER, H-MOR, and H-BEA materials was performed in a tubular packed-bed quartz reactor (10 mm inner diameter) under atmospheric pressure. A mixture of DME/Ar/He (0.17 cm^3 s^{-1}; 24.9% DME, 25.1% Ar and 50% He; Praxair) was introduced by He (0.67 cm^3 s^{-1}, ultrapure, Minneapolis oxygen) during each pulse with 90 s intervals. The physisorbed DME and water formed were subsequently removed by He (1.67 cm^3 s^{-1}) for 1.5 to 2.5 hours.

The DME uptake ratio per Al site on the three zeolites is tabulated in Table S.3.2.2. Cheung et al. [76] showed that each Brønsted acid site can adsorb 0.5 DME molecules because DME reacts with surface hydroxyl groups to form persistent methyl groups.

Therefore, the concentration of Brønsted acid sites in the three zeolites used in this study is nearly identical to that of concentration of Aluminum in these materials.

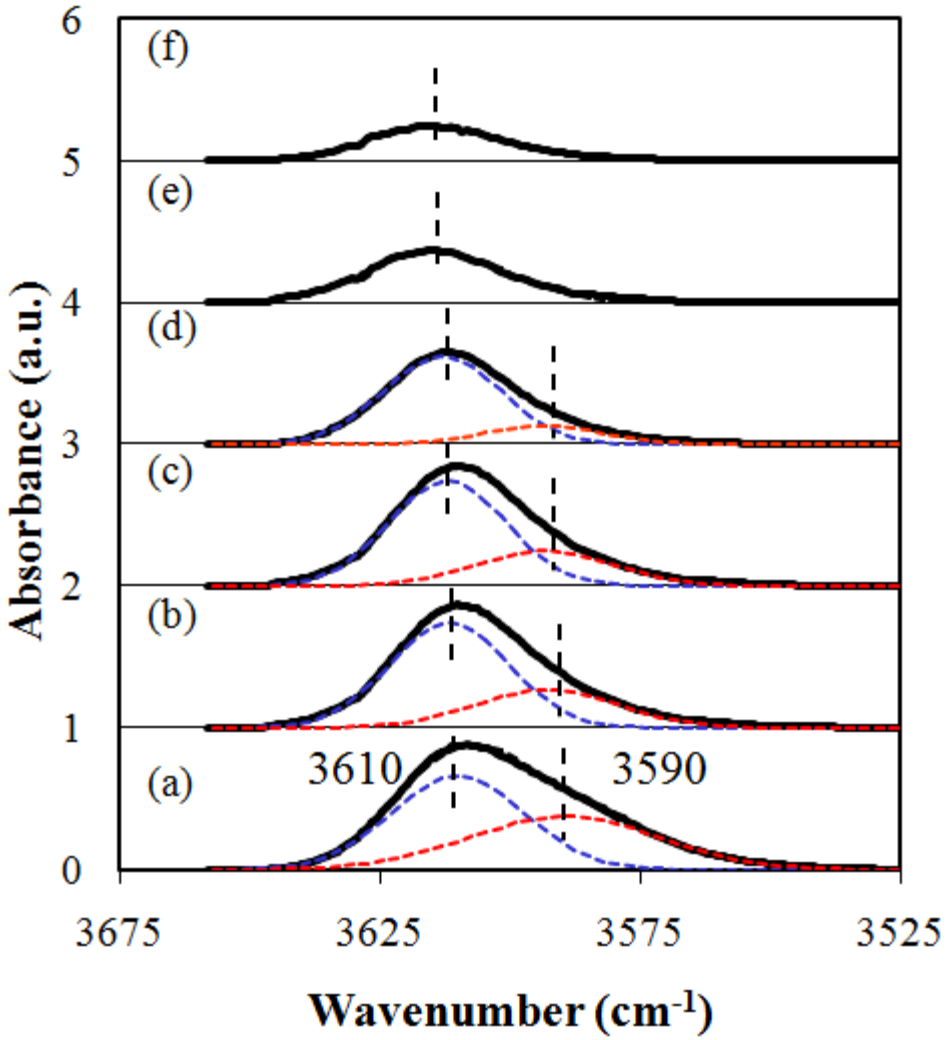

Figure S.3.1.1. Infrared spectra (solid lines) and deconvoluted bands (dashed lines) corresponding to O-H groups in 8-MR and 12-MR channels for (a) $H_{100}Na_0MOR$, (b) $H_{81}Na_{19}MOR$, (c) $H_{77}Na_{23}MOR$, (d) $H_{55}Na_{45}MOR$, (e) $H_{32}Na_{68}MOR$, and (f) $H_{19}Na_{81}$-MOR.

Table S.3.1.1. The percentage of Brønsted acid sites left in 8-MR side pockets and 12-MR channels of sodium exchanged MOR.

Sample	Number of Brønsted acid sites		
	Total	12-MR	8-MR
H-MOR	100	55(100%)	45(100%)
$H_{81}Na_{19}MOR$	81	55(100%)	26(56%)
$H_{55}Na_{45}MOR$	55	46(82%)	9(21%)
$H_{32}Na_{68}MOR$	32	32(57%)	0(0%)
$H_{19}Na_{81}MOR$	19	19(38%)	0(0%)

The number in the parentheses is the percentage of left Brønsted acid sites

Table S.3.2.2. Adsorbed DME per Al atom on zeolites at 438 K

	H-FER (Si/Al= 11.5)	H-MOR (Si/Al= 11.1)	BEA (Si/Al=12)
DME/Al	0.45	0.48	0.42

Bibliography

[1] I. Chorkendorff, and J.W. Niemantsverdriet, Concepts of Modern Catalysis and Kinetics. Wiley-VCH, 2007.

[2] J. Elzea Kogel, N.C. Trivedi, and J.M. Barker, Industrial Minerals & Rocks: Commodities, Markets, and Uses. Society for Mining Metallurgy, 2006.

[3] X. Krokidis, P. Raybaud, A.E. Gobichon, B. Rebours, P. Euzen, and H. Toulhoat, J. Phys. Chem. B 105 (2001) 5121-5130.

[4] M. Trueba, and S.P. Trasatti, Eur. J. Inorg. Chem. (2005) 3393-3403.

[5] A. Bhan, and E. Iglesia, Accounts of Chemical Research 41 (2008) 559-567.

[6] A. Corma, Chemical Reviews 95 (1995) 559-614.

[7] M.E. Davis, Nature 417 (2002) 813-821.

[8] A. Corma, Journal of Catalysis 216 (2003) 298-312.

[9] P.B. Weisz, Pure and Applied Chemistry 52 (1980) 2091-2103.

[10] S.M. Csicsery, Zeolites 4 (1984) 202-213.

[11] T.F. Degnan, Journal of Catalysis 216 (2003) 32-46.

[12] L.A. Clark, M. Sierka, and J. Sauer, Journal of the American Chemical Society 126 (2004) 936-947.

[13] W.O. Haag, R.M. Lago, and P.B. Weisz, Faraday Discussions 72 (1981) 317-330.

[14] W. Wang, J. Jiao, Y.J. Jiang, S.S. Ray, and M. Hunger, Chemphyschem 6 (2005) 1467-1469.

[15] J.N. Kondo, K. Ito, E. Yoda, F. Wakabayashi, and K. Domen, Journal of Physical Chemistry B 109 (2005) 10969-10972.

[16] A. Zecchina, S. Bordiga, G. Spoto, D. Scarano, G. Spano, and F. Geobaldo, Journal of the Chemical Society-Faraday Transactions 92 (1996) 4863-4875.

[17] C.C. Lee, R.J. Gorte, and W.E. Farneth, Journal of Physical Chemistry B 101 (1997) 3811-3817.

[18] J. Macht, R.T. Carr, and E. Iglesia, Journal of the American Chemical Society 131 (2009) 6554-6565.

[19] A. van de Runstraat, J.A. Kamp, P.J. Stobbelaar, J. van Grondelle, S. Krijnen, and R.A. van Santen, Journal of Catalysis 171 (1997) 77-84.

[20] F. de Gauw, J. van Grondelle, and R.A. van Santen, Journal of Catalysis 206 (2002) 295-304.

[21] P.B. weisz, and E.W. Swegler, Science 126 (1957).

[22] H.Y. Chu, R.P. Rosynek, and J.H. Lunsford, Journal of Catalysis 178 (1998) 352-362.

[23] R. Gounder, and E. Iglesia, Journal of the American Chemical Society 131 (2009) 1958-1971.

[24] B. Xu, C. Sievers, S.B. Hong, R. Prins, and J.A. van Bokhoven, Journal of Catalysis 244 (2006) 163-168.

[25] J.N. Kondo, S.W. Yang, Q.J. Zhu, S. Inagaki, and K. Domen, Journal of Catalysis 248 (2007) 53-59.

[26] V. Nieminen, M. Sierka, D.Y. Murzin, and J. Sauer, Journal of Catalysis 231 (2005) 393-404.

[27] B.A. De Moor, M.F. Reyniers, and G.B. Marin, Physical Chemistry Chemical Physics 11 (2009) 2939-2958.

[28] T. Blasco, Chemical Society Reviews 39 (2010) 4685-4702.

[29] Y.J. Jiang, M. Hunger, and W. Wang, Journal of the American Chemical Society 128 (2006) 11679-11692.

[30] T. Demuth, X. Rozanska, L. Benco, J. Hafner, R.A. van Santen, and H. Toulhoat, Journal of Catalysis 214 (2003) 68-77.

[31] M. Boronat, P. Viruela, and A. Corma, Journal of Physical Chemistry 100 (1996) 16514-16521.

[32] J.A. Wang, X. Bokhimi, A. Morales, O. Novaro, T. Lopez, and R. Gomez, J. Phys. Chem. B 103 (1999) 299-303.

[33] Y. Cesteros, P. Salagre, F. Medina, and J.E. Sueiras, Chem. Mat. 11 (1999) 123-129.

[34] Y.X. Pan, C.J. Liu, and Q.F. Ge, Langmuir 24 (2008) 12410-12419.

[35] M. Digne, P. Sautet, P. Raybaud, P. Euzen, and H. Toulhoat, J. Catal. 226 (2004) 54-68.

[36] R.A. Zotov, V.V. Molchanov, A.M. Volodin, and A.F. Bedilo, J. Catal. 278 (2011) 71-77.

[37] M.C. Manchado, J.M. Guil, A.P. Masia, A.R. Paniego, and J.M.T. Menayo, Langmuir 10 (1994) 685-691.

[38] M.P. Rosynek, J. Phys. Chem. 79 (1975) 1280-1284.

[39] X.S. Liu, and R.E. Truitt, J. Am. Chem. Soc. 119 (1997) 9856-9860.

[40] E.P. Parry, J. Catal. 2 (1963) 371-379.

[41] A. Zecchina, E.E. Platero, and C.O. Area´n, J. Catal. 107 (1987) 244-247.

[42] B.C. Shi, and B.H. Davis, J. Catal. 157 (1995) 359-367.

[43] H. Knözinger, Angew. Chem. internat. Edit 7 (1968) 791-805.

[44] H. Knözinger, and A. Scheglila, J. Catal. 17 (1970) 252-263.

[45] E.C. Decanio, V.P. Nero, and J.W. Bruno, J. Catal. 135 (1992) 444-457.

[46] J.H. Kwak, R. Rousseau, D.H. Mei, C.H.F. Peden, and J. Szanyi, ChemCatChem 3 (2011) 1557-1561.

[47] S. Roy, G. Mpourmpakis, D.Y. Hong, D.G. Vlachos, A. Bhan, and R.J. Gorte, accepted by ACS catalysis (2012). DOI: 10.1021/cs300176d.

[48] B.E.S. Workshop. 2007. Basic Research Needs: Catalysis for Energy. U. S. Department of Energy, editor.

[49] B. Arstad, and S. Kolboe, Journal of the American Chemical Society 123 (2001) 8137-8138.

[50] M. Bjorgen, S. Svelle, F. Joensen, J. Nerlov, S. Kolboe, F. Bonino, L. Palumbo, S. Bordiga, and U. Olsbye, Journal of Catalysis 249 (2007) 195-207.

[51] R.M. West, D.J. Braden, and J.A. Dumesic, Journal of Catalysis 262 (2009) 134-143.

[52] G.W. Huber, and A. Corma, Angewandte Chemie-International Edition 46 (2007) 7184-7201.

[53] A. Corma, G.W. Huber, L. Sauvanauda, and P. O'Connor, Journal of Catalysis 257 (2008) 163-171.

[54] F. Eder, M. Stockenhuber, and J.A. Lercher, Journal of Physical Chemistry B 101 (1997) 5414-5419.

[55] M.W. Anderson, and J. Klinowski, Journal of the American Chemical Society 112 (1990) 10-16.

[56] C.B. Phillips, and R. Datta, Industrial & Engineering Chemistry Research 36 (1997) 4466-4475.

[57] C. Delaspozas, R. Lopezcordero, J.A. Gonzalezmorales, N. Travieso, and R. Roquemalherbe, Journal of Molecular Catalysis 83 (1993) 145-156.

[58] J.C. Oudejans, P.F. Vandenoosterkamp, and H. Vanbekkum, Applied Catalysis 3 (1982) 109-115.

[59] R. Levanmao, T.M. Nguyen, and G.P. McLaughlin, Applied Catalysis 48 (1989) 265-277.

[60] S. Bun, S. Nishiyama, S. Tsuruya, and M. Masai, Applied Catalysis 59 (1990) 13-29.

[61] I. Takahara, M. Saito, M. Inaba, and K. Murata, Catalysis Letters 105 (2005) 249-252.

[62] D. Varisli, T. Dogu, and G. Dogu, Chemical Engineering Science 62 (2007) 5349-5352.

[63] Q.J. Zhu, J.N. Kondo, S. Inagaki, and T. Tatsumi, Topics in Catalysis 52 (2009) 1272-1280.

[64] S. Svelle, S. Kolboe, O. Swang, and U. Olsbye, Journal of Physical Chemistry B 109 (2005) 12874-12878.

[65] S. Svelle, C. Tuma, X. Rozanska, T. Kerber, and J. Sauer, Journal of the American Chemical Society 131 (2009) 816-825.

[66] S.R. Blaszkowski, and R.A. vanSanten, Journal of the American Chemical Society 118 (1996) 5152-5153.

[67] IZA Structure and Commission, http://www.iza-structure.org/.

[68] J. Macht, M.J. Janik, M. Neurock, and E. Iglesia, Angewandte Chemie-International Edition 46 (2007) 7864-7868.

[69] J. Macht, M.J. Janik, M. Neurock, and E. Iglesia, Journal of the American Chemical Society 130 (2008) 10369-10379.

[70] M.J. Janik, J. Macht, E. Iglesia, and M. Neurock, Journal of Physical Chemistry C 113 (2009) 1872-1885.

[71] K.Y. Lee, T. Arai, S. Nakata, S. Asaoka, T. Okuhara, and M. Misono, Journal of the American Chemical Society 114 (1992) 2836-2842.

[72] F. Eder, and J.A. Lercher, Journal of Physical Chemistry B 101 (1997) 1273-1278.

[73] J. Huang, Y. Jiang, V.R.R. Marthala, and M. Hunger, Journal of the American Chemical Society 130 (2008) 12642-+.

[74] P. Cheung, A. Bhan, G.J. Sunley, D.J. Law, and E. Iglesia, Journal of Catalysis 245 (2007) 110-123.

[75] A. Bhan, A.D. Allian, G.J. Sunley, D.J. Law, and E. Iglesia, Journal of the American Chemical Society 129 (2007) 4919-4924.

[76] P. Cheung, A. Bhan, G.J. Sunley, and E. Iglesia, Angewandte Chemie-International Edition 45 (2006) 1617-1620.

[77] M. Brandle, and J. Sauer, Journal of the American Chemical Society 120 (1998) 1556-1570.

[78] C. Lo, and B.L. Trout, Journal of Catalysis 227 (2004) 77-89.

[79] R. Gounder, and E. Iglesia, Angewandte Chemie-International Edition 49 (2010) 808-811.

[80] H. Chiang, and A. Bhan, Journal of Catalysis 271 (2010) 251-261.

[81] A.L.L. East, T. Bucko, and J. Hafner, Journal of Physical Chemistry A 111 (2007) 5945-5947.

[82] H.J. Fang, A.M. Zheng, S.H. Li, J. Xu, L. Chen, and F. Deng, Journal of Physical Chemistry C 114 (2010) 1054-10264.

[83] S. Namuangruk, D. Tantanak, and J. Limtrakul, Journal of Molecular Catalysis A: Chemical 256 (2006) 113-121.

[84] M.T. Aronson, R.J. Gorte, W.E. Farneth, and D. White, Journal of the American Chemical Society 111 (1989) 840-846.

[85] M.T. Aronson, R.J. Gorte, and W.E. Farneth, Journal of Catalysis 105 (1987) 455-468.

[86] D. Schuring, A.P.J. Jansen, and R.A. van Santen, Journal of Physical Chemistry B 104 (2000) 941-948.

[87] L.A. Clark, A. Gupta, and R.Q. Snurr, Journal of Physical Chemistry B 102 (1998) 6720-6731.

[88] M.A. Makarova, A.E. Wilson, B.J. van Liemt, C. Mesters, A.W. de Winter, and C. Williams, Journal of Catalysis 172 (1997) 170-177.

[89] V.A. Veefkind, M.L. Smidt, and J.A. Lercher, Applied Catalysis A: General 194 (2000) 319-332.

[90] M. Maache, A. Janin, J.C. Lavalley, and E. Benazzi, Zeolites 15 (1995) 507-516.

[91] J.R. Carpenter, S. Yeh, S.I. Zones, and M.E. Davis, Journal of Catalysis 269 (2010) 64-70.

[92] T. Yashima, Z.B. Wang, A. Kamo, T. Yoneda, and T. Komatsu, Catalysis Today 29 (1996) 279-283.

[93] J.F. Denayer, G.V. Baron, J.A. Martens, and P.A. Jacobs, Journal of Physical Chemistry B 102 (1998) 3077-3081.

[94] C.E. Ramachandran, B.A. Williams, J.A. van Bokhoven, and J.T. Miller, Journal of Catalysis 233 (2005) 100-108.

[95] J.F. Denayer, W. Souverijns, P.A. Jacobs, J.A. Martens, and G.V. Baron, Journal of Physical Chemistry B 102 (1998) 4588-4597.

[96] B.A. De Moor, M.F. Reyniers, O.C. Gobin, J.A. Lercher, and G.B. Marin, Journal of Physical Chemistry C 115 (2011) 1204-1219.

[97] X. Rozanska, L. Barbosa, and R.A. van Santen, Journal of Physical Chemistry B 109 (2005) 2203-2211.

[98] X. Rozanska, R.A. van Santen, F. Hutschka, and J. Hafner, Journal of Catalysis 215 (2003) 20-29.

[99] X. Rozanska, R.A. van Santen, F. Hutschka, and J. Hafner, Journal of the American Chemical Society 123 (2001) 7655-7667.

[100] M. Boronat, C.M. Zicovich-Wilson, P. Viruela, and A. Corma, Journal of Physical Chemistry B 105 (2001) 11169-11177.

[101] X. Rozanska, T. Demuth, F. Hutschka, J. Hafner, and R.A. van Santen, Journal of Physical Chemistry B 106 (2002) 3248-3254.

[102] C.L. Cavalcante, and D.M. Ruthven, Industrial & Engineering Chemistry Research 34 (1995) 177-184.

[103] F. Jimenez-Cruz, and G.C. Laredo, Fuel 83 (2004) 2183-2188.

[104] C.E. Webster, R.S. Drago, and M.C. Zerner, Journal of the American Chemical Society 120 (1998) 5509-5516.

[105] I. Daems, R. Singh, G. Baron, and J. Denayer, Chemical Communications (2007) 1316-1318.

[106] S.I. Zones, and T.V. Harris, Microporous and Mesoporous Materials 35-6 (2000) 31-46.

[107] J.A. Martens, R. Parton, L. Uytterhoeven, P.A. Jacobs, and G.F. Froment, Applied Catalysis 76 (1991) 95-116.

[108] S. Savitz, F. Siperstein, R.J. Gorte, and A.L. Myers, Journal of Physical Chemistry B 102 (1998) 6865-6872.

[109] G. Gutierrez, A. Taga, and B. Johansson, Phys. Rev. B 65 (2002) 4.

[110] W.Y. Ching, L.Z. Ouyang, P. Rulis, and H.Z. Yao, Phys. Rev. B 78 (2008).

[111] M.H. Lee, C.F. Cheng, V. Heine, and J. Klinowski, Chemical Physics Letters 265 (1997) 673-676.

[112] C.S. John, N.C.M. Alma, and G.R. Hays, Applied Catalysis 6 (1983) 341-346.

[113] G. Paglia, A.L. Rohl, C.E. Buckley, and J.D. Gale, Phys. Rev. B 71 (2005) 16.

[114] A.R. Ferreira, E. Kucukbenli, A.A. Leitao, and S. de Gironcoli, Phys. Rev. B 84 (2011) 9.

[115] L.A. O'Dell, S.L.P. Savin, A.V. Chadwick, and M.E. Smith, Solid State Nucl. Magn. Reson. 31 (2007) 169-173.

[116] M.R. Hill, T.J. Bastow, S. Celotto, and A.J. Hill, Chem. Mat. 19 (2007) 2877-2883.

[117] E. Brunner, Catal. Today 38 (1997) 361-376.

[118] A.L. Blumenfeld, and J.J. Fripiat, Top. Catal. 4 (1997) 119-129.

[119] D. Coster, A.L. Blumenfeld, and J.J. Fripiat, J. Phys. Chem. 98 (1994) 6201-6211.

[120] X.S. Liu, J. Phys. Chem. C 112 (2008) 5066-5073.

[121] J.A. Ripmeester, J. Am. Chem. Soc. 105 (1983) 2925-2927.

[122] C. Morterra, and G. Magnacca, Catal. Today 27 (1996) 497-532.

[123] M.R. Basila, and T.R. Kantner, J. Phys. Chem. 70 (1966) 1681.

[124] M.R. Basifo, T.R. Kantner, and I.H. Rhee, J. , J. Phys. Chem. 68 (1964).

[125] S.L. Soled, G.B. McVicker, L.L. Murrell, L.G. Sherman, N.C. Dispenziere, S.L. Hsu, and D. Waldman, J. Catal. 111 (1988) 286-295.

[126] H.D. Morris, and P.D. Ellis, J. Am. Chem. Soc. 111 (1989) 6045-6049.

[127] B.A. HENDRIKSEN, D.R. PEARCE, and R. RUDHAM, J. Catal. 24 (1972) 82-87.

[128] R. Wischert, C. Coperet, F. Delbecq, and P. Sautet, Angew. Chem.-Int. Edit. 50 3202-3205.

[129] S.H. Cai, and K. Sohlberg, J. Mol. Catal. A-Chem. 193 (2003) 157-164.

[130] P.A. Clayborne, T.C. Nelson, and T.C. DeVore, Applied Catalysis a-General 257 (2004) 225-233.

[131] H.A. Dabbagh, M. Zamani, and B.H. Davis, J. Mol. Catal. A-Chem. 333 (2010) 54-68.

[132] R.G. GREENLER, THE JOVRNAL OF CHEMICAL PHYSICS 37 (1962) 2094-2100.

[133] H. Jeziorowski, H. Knözinger, W. Meye, and H.D. Müller, 69 (1973) 1744-1758.

[134] H. Knözinger, and B. Stübner, J. Phys. Chem. 82 (1978) 1526-1532.

[135] T.P. Beebe, J.E. Crowell, and J.T. Yates, J. Phys. Chem. 92 (1988) 1296-1301.

[136] H. Pines, and W.O. Haag, J. Am. Chem. Soc. 83 (1961) 2847-2852.

[137] H. Knözinger, H. Buhl, and K. Kochloefl, J. Catal. 24 (1972) 57-68.

[138] J.P. Perdew, K. Burke, and M. Ernzerhof, Physical Review Letters 77 (1996) 3865-3868.

[139] H. Knözinger, and E. Ress, Z. physik. Chem. NF. 54 (1967) 136-149.

[140] M. Delgado, F. Delbecq, C.C. Santini, F. Lefebvre, S. Norsic, P. Putaj, P. Sautet, and J.M. Basset, J. Phys. Chem. C 116 834-843.

[141] H. Knözinger, A. Scheglila, and A.M. Watson, The Journal of Physical Chemistry 72 (1968) 2770-2774.

[142] C.D. Baertsch, K.T. Komala, Y.H. Chua, and E. Iglesia, J. Catal. 205 (2002) 44-57.

[143] J.H. Kwak, J.Z. Hu, D.H. Kim, J. Szanyi, and C.H.F. Peden, J. Catal. 251 (2007) 189-194.

[144] C. Morterra, G. Cerrato, and G. Meligrana, Langmuir 17 (2001) 7053-7060.

[145] S. Golay, R. Doepper, and A. Renken, Applied Catalysis a-General 172 (1998) 97-106.

[146] T.H. Lowry, and K.S. Richardson, Mechanism and Theory in Organic Chemistry, Addison Wesley Longman.